

## Effects of gold nanoparticles dispersed in anodes for dye sensitized solar cells

Master's thesis in Applied Physics

ERIK ANVELL



# Effects of gold nanoparticles dispersed in anodes for dye sensitized solar cells

ERIK ANVELL

Department of Applied Physics  
CHALMERS UNIVERSITY OF TECHNOLOGY  
Gothenburg, Sweden 2015

Effects of gold nanoparticles dispersed in anodes for dye sensitized solar cells

ERIK ANVELL

©Erik Anvell, 2015

Department of Applied Physics  
CHALMERS UNIVERSITY OF TECHNOLOGY  
SE-4120 96 Gothenburg  
Sweden  
Telephone: +46 (0)31-772 00 00

Printed by Chalmers Reproservice  
Gothenburg, Sweden 2015

## Abstract

Future solar cells need to be cheaper, more efficient and produced in an environmental friendly way to be a competitive and sustainable alternative for solar energy conversion. The emerging dye sensitized solar cells (DSSCs) might be able to meet future demands regarding price, structural flexibility and environmental issues, but for the time being, their potential as a competitive and viable alternative is hampered by low energy conversion efficiencies and stability issues. A most central process in the conversion of sunlight energy directly into electric energy, is the photon to charge carrier conversion which takes place in the photoactive part of the solar cell. To achieve a high incident photon to charge carrier efficiency (IPCE), efficient absorption of incoming sunlight over a wide range of wavelengths is needed. The use of plasmonic effects generated by metal nanoparticles (MNP) in combination with a sensitizing dye is an interesting approach to increase the IPCE for DSSCs. In this work, effects on cell energy conversion efficiency of adding gold nanoparticles (GNPs) have been studied. Spherical GNPs of diameter 5, 10 and 40 nm, embedded in the photoactive layers have been studied in combination with three different sensitizing dyes; Ruthenizer 455-PF6, Ruthenizer 620-1H3BTA and Sensidizer SQ2. Cells without dye were also included in the study. TiO<sub>2</sub> was used as semiconductor material in thin (< 1 μm) photoactive layers. Complete DSSCs containing gel electrolyte have been built and characterized with I-V graphs using different light intensities of 0.11, 0.55, 0.79 and 1.0 sun.

The results clearly show that the cell efficiency can be improved by using GNPs this way, it was also shown that certain combinations of dye and GNP sizes affected cell efficiency more positive than others while addition of GNPs to cells without dye sensitizer affected the efficiency negatively. Most positive results were achieved using the organic dye Ruthenizer 455-PF6 in combination with 40 nm GNPs, showing relative efficiency increase well above 25 %.

### Key words:

dye sensitized solar cells, gold nanoparticles, sensitizing dyes, local surface plasmon resonance



## Acknowledgements

First of all I want to thank my examiner of this work, Professor Bengt-Erik Mellander and my supervisor, Maurizio Furlani, for planning and providing the proper conditions for a work like this, and also for giving me the needed support and guidance to carry it out. Ingvar Albinsson, Johanna Stiernstedt, Fredrik Larsson, Antti Rytinki, Daniele Franchi and Anja Herrmann, thank you all for the supportive and friendly atmosphere in our Electrophysics group. A special thank you to Anja, who often helped me out with both hardware and software problems in the lab, always with a friendly smile and witty comments.

During this work, I also had the privilege to meet two guest scientist from Sri Lanka, Dr Wijendra Bandara and Sampath Fernando. Dr Bandara, who has a profound understanding for DSSCs as well as long experience of building them for testing and evaluation, was always willing to share his knowledge with me. Sampath who was always helpful around the lab equipment thought me some useful tricks and techniques. Thank you both for all your help, interesting discussions and pleasant company.

Part of the experimental work has been conducted outside the Electrophysics division and I want to express my gratitude to Professor Aleksandar Matic and Ezio Zanghellini at the Condensed Matter Physics division, for letting me use their equipment for spin coating electrodes. All our absorption measurements were carried out at the Polymer Technology division and I want to thank Assistant Professor Ergang Wang and Dr. Desta Antenehe Gedefaw who invited us to carry out our measurements in their laboratory. Special thanks are addressed to Desta, always willing to help out whenever it was needed. Desta assisted me in the lab, showing how to use the equipment and also assisted me in some of the measurements.

I want to thank Valeria Saavedra at the Division of Physical Chemistry for interesting and instructive discussions during our cooperation on gel electrolytes. Valeria also arranged for an interesting field trip to The Ångström laboratories at Uppsala University where she showed their solar cell laboratories and also helped me with some thickness measurements of  $\text{TiO}_2$  layers. I also want to thank Professor Dinko Chakarov for his professional opinion and for providing inspiration. Assistant Professor Åsa Haglund, always a source of inspiration, provided some important and useful facts about light intensity measurements, thank you for that. And last but not least I also want thank Eddy Haglund, Jan-Åke Wiman, Lars Hellberg, Hans Odelius and Mats Rostedt for helping out in different situations, somehow connected to this work.

Erik Anvell, Gothenburg 05/10/15



# Contents

<b>I</b>	<b>INTRODUCTION</b>	<b>1</b>
<b>1</b>	<b>Energy supply</b>	<b>1</b>
1.1	Motivation . . . . .	1
1.2	The potential of solar energy . . . . .	3
1.3	History of solar cells . . . . .	5
1.4	Different types of solar cells . . . . .	6
1.5	The aim of this work . . . . .	8
<b>2</b>	<b>Choice of materials</b>	<b>9</b>
2.1	Gold nanoparticles . . . . .	9
2.2	Choice of GNPs for this work . . . . .	11
2.3	Photosensitizing dyes . . . . .	12
2.4	Electrolytes . . . . .	13
2.5	TiO <sub>2</sub> slurry . . . . .	13
<b>II</b>	<b>THEORY</b>	<b>15</b>
<b>3</b>	<b>Physics of solar cells</b>	<b>17</b>
3.1	Sunlight . . . . .	17
3.2	The AM sunlight standard . . . . .	18
3.3	Working principles of solar cells . . . . .	21
3.3.1	General function of a solar cell . . . . .	21
3.3.2	Dye sensitized photoelectrochemical cells . . . . .	24
3.4	Limitations of performance . . . . .	29
<b>4</b>	<b>Characterizing properties of solar cells</b>	<b>33</b>
4.1	Measuring and testing conditions . . . . .	33
4.2	I-V characteristics of a solar cell . . . . .	33
4.3	Efficiency . . . . .	34
4.4	Fillfactor . . . . .	35
<b>5</b>	<b>Modelling of solar cells</b>	<b>37</b>
5.1	The ideal solar cell model . . . . .	37
5.2	Simple realistic solar cell model . . . . .	38
5.3	Dye sensitized solar cell model . . . . .	40
<b>6</b>	<b>Localized surface plasmon resonance</b>	<b>41</b>
<b>7</b>	<b>Enhancing the performance of a DSSC</b>	<b>47</b>

<b>III</b>	<b>EXPERIMENTAL</b>	<b>49</b>
<b>8</b>	<b>Experimental</b>	<b>51</b>
8.1	Chemicals . . . . .	52
8.2	Experimental equipment . . . . .	53
8.3	Preparation of materials . . . . .	59
8.3.1	Gold nanoparticles . . . . .	59
8.3.2	Dyes . . . . .	60
8.3.3	Electrolytes . . . . .	64
8.3.4	TiO <sub>2</sub> substrates . . . . .	65
8.3.5	Electrodes . . . . .	65
8.3.6	Assembling of the cell . . . . .	68
8.4	Characterization of the cells . . . . .	71
8.5	Gold nanoparticle experiments . . . . .	72
8.5.1	Series 1 experiments . . . . .	75
8.5.2	Series 2 experiments . . . . .	76
<b>IV</b>	<b>RESULTS</b>	<b>77</b>
<b>9</b>	<b>Results and discussion</b>	<b>79</b>
9.1	Absorption measurements . . . . .	79
9.1.1	Absorption spectra of dyes . . . . .	80
9.1.2	Absorption spectra of gold colloids . . . . .	81
9.2	TiO <sub>2</sub> slurry composition . . . . .	82
9.3	Impedance measurements of the electrolyte . . . . .	85
9.4	Characterization of the cells . . . . .	87
9.4.1	I-V graphs for cells in series 1 . . . . .	88
9.4.2	Efficiency of cells in series 1 . . . . .	90
9.4.3	Current at maximum power of cells in series 1 . . . . .	92
9.4.4	I-V graphs for cells in series 2 . . . . .	93
9.4.5	Efficiency of cells in series 2 . . . . .	95
9.4.6	Fill factor of cells in series 2 . . . . .	98
9.4.7	Short circuit current of cells in series 2 . . . . .	100
9.4.8	Open circuit voltage of cells in series 2 . . . . .	104
9.4.9	Current at maximum power of cells in series 2 . . . . .	106
9.4.10	Voltage at maximum power of cells in series 2 . . . . .	108
<b>10</b>	<b>Conclusions and outlook</b>	<b>111</b>
<b>A</b>	<b>Furnace test</b>	<b>113</b>
<b>B</b>	<b>Solar simulator test</b>	<b>115</b>

<b>C</b>	<b>Capacitive properties of DSSC</b>	<b>119</b>
<b>D</b>	<b>Nitric acid effects on GNPs</b>	<b>125</b>
D.1	Absorption measurements . . . . .	126
D.2	Comparing cell performance . . . . .	133

## Acronyms

AM	Air Mass
AU	Astronomical Unit
BTU	British Thermal Unit
CB	Conduction Band
CIGS	Copper Indium Gallium Selenide
DSSC	Dye Sensitized Solar Cell
EIA	U.S Energy Information Agency
FF	Fill Factor
FTO	Fluorine Tin Oxide
GNP	Gold Nano Particle
HOMO	Highest Occupied Molecular Orbit
IPCC	International Panel on Climate Change
IR	Infra Red
I-V	Current voltage
LSPR	Local Surface Plasmon Resonance
LUMO	Lowest Unoccupied Molecular Orbit
MJSC	Multi Junction Solar Cell
MNP	Metal Nano Particle
NIR	Near Infra Red
NP	Nano Particle
NREL	National Renewable Energy Laboratory
PAN	PolyAcryloNitrile
PC	PolyCarbonate
PEC	Photo Electrochemical Cell
PV	Photo Voltaic
QBTU	Quadrillion British Thermal Unit
RPM	Revolutions Per Minute
SC	Solar Cell
SQ	Schockley Queisser
SRC	Standard Reporting Conditions
STC	Standard Testing Conditions
TCO	Transparent Conducting Oxide
UV	Ultra Violet
VB	Valence Band

## Symbols used in the text, figures and tables

$\alpha$	polarizability
$\varepsilon$	dielectric constant
$\eta$	efficiency
$\phi$	electric potential
$\lambda$	wavelength
$\nu$	frequency of light
$\theta$	angle
$\omega$	angular frequency of light
$\sigma$	conductivity
$\theta_{ZS}$	solar zenith angle
$a$	particle radius
$C$	capacitance
$\Delta E_{\text{sensitizer}}$	energy diff. between HOMO and LUMO levels
$e^-$	electron
$h^+$	hole
$I$	current
$I_{ph}$	photocurrent
$\vec{K}$	wavevector
$k$	magnitude of wavevector
$\vec{n}$	unit vector
$P$	power
$\vec{p}$	dipole moment
$r$	distance
$R_s$	series resistance
$R_{sh}$	shunt resistance
$S$	groundstate
$S^*$	excited state
$T$	filter transmittance, temperature
$V$	voltage

## Fundamental constants

$B_0$	solar constant
$c$	speed of light in vacuum
$\epsilon_0$	permittivity of free space
$h$	Planck's constant
$k_B$	Boltzmann's constant
$q$	elementary charge



**Part I**

# **INTRODUCTION**



# 1 Energy supply

## 1.1 Motivation

The total population of the earth is growing and the estimate for 2015 is 7.2 billion people living on earth. By the year of 2024 the population is estimated to 8 billion [1], and many of the fast growing populations are in the undeveloped regions of the world [2]. As these regions develop, the world is facing fast growing populations which are also developing into a more energy consuming lifestyle, resulting in a huge increase in total needed energy production. The energy consumption is estimated to increase by 56 % over the next three decades. Figure 1 shows some historic and projected data of the total world energy consumption from 1990 to 2040 [3], the energy unit in the figure is quadrillion British thermal units<sup>1</sup> (QBTU).

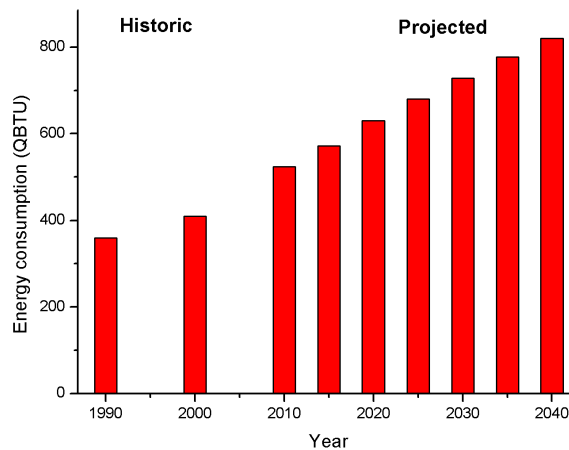


**Figure 1:** Diagram showing historical and projected total annual energy consumption of the world for the time period 1990 - 2040.

This makes humanity facing a significant increase in global demand for energy. Finding energy sources and building infrastructure to meet this demand, even in remote places, is quite a challenging task. These facts in combination with severe environmental problems connected to energy production from fossil fuels makes it an urgent and very challenging problem to solve. To meet all requirements, this end up with the task of producing more energy in a sustainable way, at a cost competitive to the existing systems. In addition to low cost, a huge advantage for the fossil fuels is their flexibility, these fuels can be used in both small and large scale systems and work well for stationary as well as mobile applications. Fossil fuels also have high energy density and can

---

<sup>1</sup> 1 QBTU =  $10^{15}$  BTU, 1 BTU = 1055.1 J.

easily be transported and stored without considerable loss. At the end users, they can be used in different ways, covering applications from high technological combustion engines to just burning them for heat production.

To succeed in competition with existing systems, the most probable approach will be looking for solutions in many different fields and combine different technologies to achieve efficient and reliable production systems. The efforts that are put in to find smart energy saving solutions are not enough to solve the problem. The main issue here is to find new, clever and sustainable solutions, and to improve some existing ones, to produce the needed energy.

If the International Panel on Climate Change (IPCC) goal of at most 2 degrees increase of the global average temperature is to be achieved, the energy supplied from fossil fuels, or the environmental effects from it must be reduced. In Sweden, the goals for renewable energy is that by 2020, at least 50 % of the produced energy should be renewable energy [4]. Solar energy is one of the alternatives that is considered having a large potential to replace energy produced from fossil fuels [5]. One of the most attractive alternatives to address these problems is probably using some concept of solar energy utilizing solar cells as direct energy converters.

Looking in a time perspective, short in comparison to geological eras, almost all energy sources except nuclear and fossil can be regarded as solar energy. The energy from the sun drives: the vaporization from the oceans which in the end gives us hydropower from the rivers, the photo synthesis processes that will store up energy in biomass and the winds around the world are driven by heat gradients caused by different amount of power irradiated from the sun at different places. However, in this report, solar energy is defined as energy converted directly from the sunlight. Within this definition there are still different ways of energy conversion, one is to use the sunlight as a heat source, heating some material and then either use the heat directly or, use some intermediate conversion to mechanical or electrical energy. Another way is to convert the energy in the sunlight directly into electrical energy. In this report, it is the direct conversion of optical energy in the sunlight into electrical energy that is considered.

It is not just the environmental arguments that suggests the use of solar energy in general and photovoltaic (PV) devices in specific. Using solar cells as energy converters has many advantages but there are also some disadvantages [6], these are listed in Table 1 on the next page.

**Table 1:** Advantages and disadvantages of using PV systems for energy supply

Advantages	Disadvantages
The fuel source, the sun, is enormous, basically infinite in human lifetime	Energy density of sunlight is relatively low Fluctuating light intensity at the surface of earth
Possibilities to match daily output and need High public acceptance High safety	Better energy storages needed
Low operation costs, no fuel needed Operation temperature = ambient temperature No moving parts in the devices No emissions, does not contribute to pollution High reliability Silent devices, no disturbing noise	High cost of installation
Can be installed near end users, even in remote places Relatively quick and simple installation Modular installation, large or small scale possible Possible to integrate in existing structures	System integration and installation not available widespread

## 1.2 The potential of solar energy

The amount of sunlight energy that is irradiating the earth is enormous. A calculation that also takes the albedo of the earth into account, shows that the solar radiation powers the earth with some 120 PW ( $120 \cdot 10^{15} \text{W}$ ) [7]. Using this as an average power, the total annual energy reaching the surface of earth will add up to  $3.78 \cdot 10^{24} \text{ J} = 3.59 \cdot 10^6 \text{ QBTU}$ . Comparing this to the estimated annual consumption for 2020 of 620 QBTU, it is obvious that with adequate converters, the sunlight can provide the modern world with all the needed energy.

The solar cell as an energy converter is well suited for both large and small systems, this makes an energy supplying system based on these devices quite flexible. Solar cells can operate in large or small scale, independently or integrated in systems. The use of solar cells for energy conversion makes it possible to produce energy near end users, even in remote places where grid infrastructure is missing. In modern systems where electrical energy is already accessible via the grid, smaller systems of solar cells can be used to cover local need and possible surplus can be added to the grid. Solar and wind power systems are sensitive to weather conditions and the cyclic variations of light. However, if a combination of different renewable systems and energy storages is used, the system as a whole will be less sensitive to these variations.

In a future vision, solar cells might be part of a concept called the hydrogen economy, this is thought to work as a global energy supplying system where energy would be stored and transported as chemical energy, using hydrogen as the main energy carrier. In this system hydrogen, is primarily produced from electrolysis of water, using electricity only from renewable sources. At the end users, the energy can be converted into electric energy using fuel cells which produce water during this process. Solar cells would be one of several sustainable choices of energy converters that could fit well into this system, provided they can be manufactured in a sustainable way and produce electricity at a competitive cost. A cycle of a simplified model for a hydrogen economy concept is depicted in Figure 2.

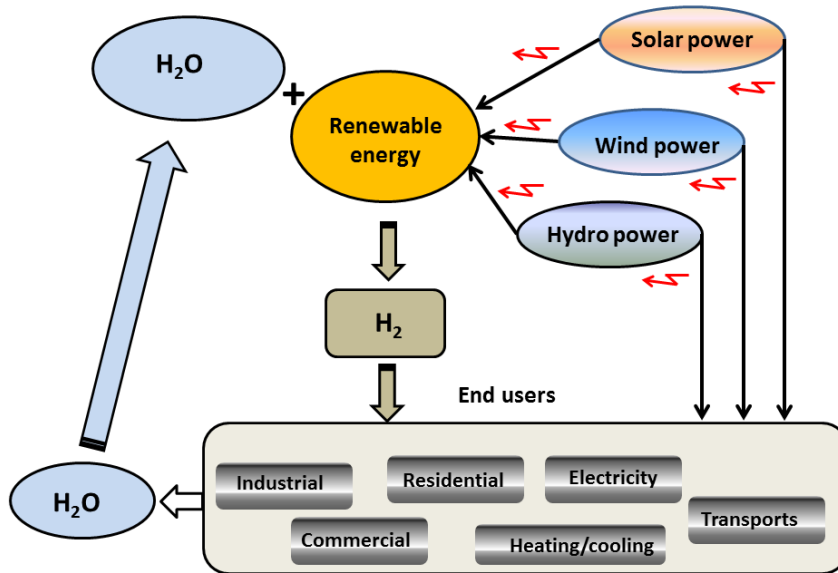


**Figure 2:** Schematic picture of the fundamental components in a hydrogen economy model powered only by renewable energy.

To be able to realize these ideas and utilize the enormous amount of energy provided by the sun, some issues have to be addressed. Basically all the steps in an energy supplying system like the hydrogen economy need to be improved in some way. At the first stage, where the sustainable energy should be produced and put into the system, the cost is one of the most central issues. The fossil and nuclear alternatives are still very cheap in comparison, so if energy from solar cells should be able to compete, the cost must be reduced significantly from present levels. If the alternatives among the different types of solar cells is compared, the dye sensitized solar cells(DSSCs) might be the strongest candidate for really cheap and rational large scale production. However,

this type of cells are not yet a fully competitive alternative, mostly due to their poor efficiency and unstable performance over time.

### 1.3 History of solar cells

A solar cell is a PV device that works on the principle of the PV effect, this effect was first discovered by the french scientist Alexandre Edmund Bequerel in 1839. Almost 50 years later, in 1883 the first functional, intentionally PV device was made by the American inventor Charles Fritts. In his notes it can be read "the current, if not wanted immediately, can be either stored where produced, in storage batteries, or transmitted a distance and there used". By writing this, Fritts predicted already some 130 years ago, the present use of the PV devices called solar cells for energy production [6].

In 1954, researchers at Bell Labs in the USA, accidentally discovered that voltage could be generated when room light was irradiating pn-junction diodes, this discovery basically marks the start of the modern era of PVs. In the following years, PV devices were developed in different ways using new approaches and improved results were reported frequently. 1973 was an important year in the history of solar cells, both in technical and non technical terms. This year the relative efficiency for the state of the art Si solar cells were improved by 30 %. As a result of the Cherry Hill Conference that year, the US Energy Research and Development Agency was formed, this was the world's first governmental group that should work with research on renewable energy. In addition, 1973 was the year of the first world oil embargo and this came to be the start signal for many governments to implement programs for development of renewable energy in which solar energy came to play a central role [6].

In 1999 the total installed PV reached 1000 MW and in 2002 it reached 2000 MW, so it took about 25 years to install the first 1000 MW, and then this figure was doubled in just three years. The years following 2002, the annual and cumulative installation of PV increased significantly. This development is depicted in Figure 3a and 3b on the next page with graphs based on data from U.S. Energy Information Administration (EIA). Until 2012 the largest annual increase in installation has been in Europe, but in 2013 the leading role was taken by China [3]. If numbers for annual consumption and total installed PV are compared for 2010, it shows that the installed PV is only about 0.2 % of the annual consumption that year.

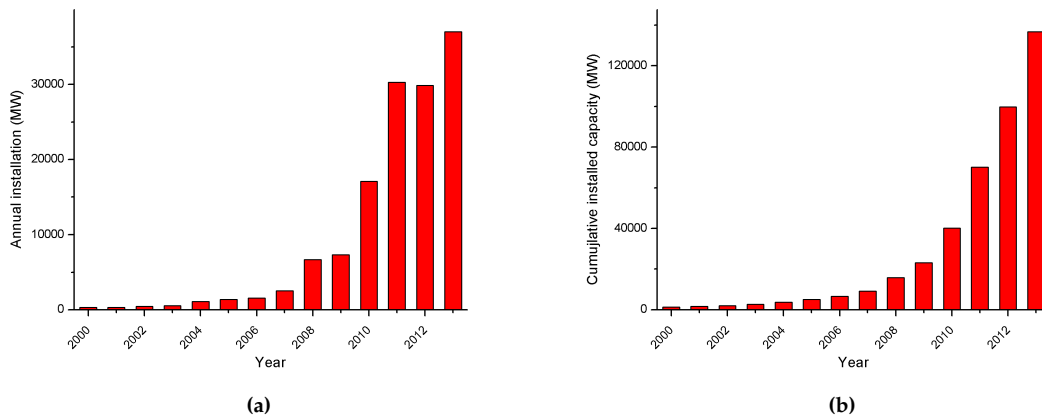


**Figure 3:** a, Annual installed PV power in the period 2000 - 2013. b, Cumulative installed PV power in the period 2000 - 2013

## 1.4 Different types of solar cells

Many different techniques and materials can be used to construct a solar cell and up to today, a great variety of different types have been developed. A presentation covering all types would be too extensive for this report, therefore in the following, just a few basic types will be presented briefly. In literature it is common to divide the different types of solar cells into generations. This division into different generations can differ a bit from one text to another, but nevertheless, it places the different approaches and types of devices in some chronological order. A summary showing different cell types and their efficiency development over the years in the period of 1975 to 2015, is presented by National Renewable Energy Laboratories(NREL)[8] and a more specific presentation of efficiencies, is presented by M. Green et. al. [9].

### First generation technologies

The most common solar cell of today is the crystalline silicon type, representing the first generation technologies, this means cells made from large grain multicrystalline or singlecrystalline materials. These cells are single junction cells which means that they are efficiency limited by the Shockley Queisser limit (SQ limit), see Section 3.4. Theoretically this limits the ideal single junctions cell efficiency to  $\sim 30\%$  under AM 1.5 direct sunlight conditions and ideal Si cells to  $\sim 29\%$ . In real cells there are always parasitic losses which make these efficiencies very hard to achieve in practice. Drawbacks for these cells are high costs due to complicated production methods and high material consumption due to the fact that Si is an indirect bandgap semiconductor. Indirect band gap causes lower absorption and therefore thicker absorbers are needed to achieve sufficient absorption, this is described in Section 3.3.1. Without light concentrators, the best cell efficiencies of  $25\%$  are reported for crystalline Si cells [9].

## Second generation technologies

Much effort has been focused on finding new materials and technologies for the next generation of solar cells which includes the thin film solar cells. The aim was to find solutions that do not require use of crystalline Si or Si-wafer substrates, this would allow for both simpler production methods and less material consumption. Progress has been made here, and some examples with promising development are devices based on thin layers of CdTe, Cadmium Indium Gallium Selenide (CIGS) and amorphous Si. These devices can be produced using large area techniques which is promising considering cheap and rational production. However, some of the materials used here are not environmental friendly and in most cases, the devices produce far below their potential maximum efficiency. The promising high efficiency research results have proven quite hard to realize in practice. Manufacturing costs and device efficiencies have to be improved if these devices are going to be competitive on the market.

## Third generation technologies

Dye sensitized solar cells (DSC, DSSC) or Grätzel cells, are a kind of hybrid cell employing both semiconductor materials and some photosensitizing dye to improve the absorption of photons. In these devices, a junction is formed between the semiconductor and the dye, and the excitation of electrons and regeneration of the dye is going on in a three dimensional structure of semiconductor, dye and electrolyte. As semiconductor,  $\text{TiO}_2$  is the most common choice because it is a cheap, non toxic and stable material. The dye is needed to ensure an acceptable absorption of photons. The  $\text{TiO}_2$  itself can absorb photons but due to its wide band gap of  $\approx 4$  electron volt(eV), most of the photons in the sun spectra will just pass through if it is used without some sensitizing dye.

The properties of the dye in a DSSC is crucial for the function of the cell. Some requirements for a good dye are: it should be a good absorber of photons in the interval of the sunlight spectrum, the lowest unoccupied molecular orbit (LUMO) level should be higher but comparable to the conduction band (CB) level of the  $\text{TiO}_2$ , it should be able to stay in service for a period of 20 years without considerable loss of efficiency, be chemically stable under light irradiation and be stable to desorption from the semiconductor material [10]. The DSSC has a great advantage in that the charge separation takes place at the interface between the dye and the semiconductor, and the charge transportation takes place in the semiconductor and the electrolyte separately. This separation makes it possible to optimize the spectral properties of the dye alone, while the charge carrier transport properties can be improved by changing the composition of the electrolyte and the semiconductor separately [11].

## 1.5 The aim of this work

The aim of this work was to address the poor efficiency of DSSCs by utilizing nanoplasmonic effects from metal nanoparticles. The chosen approach here was to study effects on cell efficiency of gold nano particles (GNPs) dispersed in the photoactive part of a DSSC. The effects were explored by building and characterizing dye sensitized solar cells with gold nano particles of different amount and size dispersed in the TiO<sub>2</sub> layer on the anode. The characterizing measurements were carried out under different intensity of light irradiation.

The study included both cells with sensitizing dye and cells containing no dye. For the sensitized cells the metal organic dyes: Ruthenizer 455-PF6, Ruthenizer 620-1H3TBA and the organic Sensidizer SQ2 were used.

The focus has mainly been on the effect on the over all cell efficiency but other properties connected to cell performance, such as fill factor, open circuit voltage and short circuit current have also been studied.

To set a framework for this work, both methods and materials had to be considered. To choose materials for the cells to investigate, some literature studies was carried out to take advantage of earlier results in this field. A discussion and a declaration of the decisions based on that study, is presented in Section 2.

## 2 Choice of materials

With the aim to study effects of gold nanoparticles (GNPs) dispersed into the photoactive part of DSSCs i.e. into the anode, the focus was mainly on the GNPs and their interaction with the photosensitizing dye and the semiconductor. This included considerations of what size and amount of the GNPs to be used as well as choice of electrolyte, dyes, composition of  $\text{TiO}_2$  slurry and thickness of photoactive layers. In the following, some effects concerning the use of GNPs and the choice of materials for this work are discussed.

### 2.1 Gold nanoparticles

The use of plasmonics for solar cell improvements is a very active and wide area of research with the aim set for direct manipulation of light in wavelengths within the visible interval [12].

Theoretically, positive effects on DSSC efficiency of adding GNPs was expected due to enhanced photon absorption, caused by the plasmonic effect from the GNPs under light irradiation. There are many reported results, showing that metal nanoparticles (GNPs) added in the anode material actually have potential to increase the energy conversion efficiency of the cells [13, 14, 15].

Two approaches within the field of using plasmonic effects in solar cells that have got much attention are: enhanced probability of photon absorption by scattering of the incident light and using near field effects to excite electrons in the photosensitizing dye or in the semiconductor material. Both of these effects can be achieved by adding GNPs into the photoactive structure of the solar cell. The photo active part of a DSSC consists of a semiconducting material in combination with a sensitizing dye, both contacting the electrolyte and the electronic conductive substrate. Adding GNPs into this concept means that there will be GNPs, semiconductor, dye and electrolyte, all together in a three dimensional structure resulting in simultaneously ongoing complicated processes. These processes which are also affecting each other, are not yet completely understood. Examples of these processes are; exciting electrons from highest occupied molecular orbital (HOMO) levels to LUMO levels in the dye, injecting electrons from the dye into the conducting band of the semiconductor, reduction of the oxidized dye molecules and quite many recombination processes of the excited electrons. [16].

A great advantage of a concept utilizing plasmonic effects, is the possibility of more efficient absorption of the irradiating light in thinner layers of photoactive materials. This might make production of more efficient solar cells using less material possible, which in turn will make them a cheaper and more competitive alternative.

In addition to placement of GNPs inside the absorber material for increased absorption and scattering, GNPs can also be placed at the semiconductor surface and even at some small distance above the surface to increase the in-coupling of light. Increased in-coupling, will increase the photon flux inside the absorber which in turn increases the probability for absorption. In-coupling of light, refers to the process of light passing through the cell surface, reaching the interior of the cell. Both size and shape as well as the relative position of the GNPs are reported to be key factors for the efficiency of light in-coupling. [17, 18]. In this work, the incoupling effects by GNPs at the surface or outside the absorber were not studied, instead the focus was only on effects of GNPs placed inside the absorbing material.

There are many approaches under investigation to study and understand the scattering of the light and the enhanced near field effects caused by plasmonics. Examples of these approaches are;

- Using GNPs with a  $\text{SiO}_2$  shell which would isolate the GNPs from both  $\text{TiO}_2$  particles and dye molecules. A positive effect from this is less recombination between GNPs,  $\text{TiO}_2$  and electrolyte [19]. The GNPs would also have a protection against corrosion due to contact with the electrolyte chemicals.
- Arrangement of nanoparticles in structures has been tried: it has been proven in experiments that light scattering from nanoparticle arrays can increase the photocurrent in thin film solar cells [20].
- Using effects of plasmon coupling between GNPs can increase the photon absorption, it is reported that 100 nm GNPs would be the optimum size for coupled particles while 40 nm would be optimal for isolated ones, the reported experimental results are also confirmed by theoretical calculations [13].

Enhancement of photocurrent is reported for both separate, isolated GNPs, as well as coupled ones. Here, coupled particles refers to particles close enough to produce plasmonic effects between them that are stronger than it would be for separate particles. The effects are size dependent and the optimum size for separate particles is 40 nm and 100 nm for coupled ones. Also, when the distance between particles is less than the particle diameter, the localized field between them is much stronger than the one from a single GNP. The coupling effect has been reported to produce enhanced performance in the long wavelength range [13].

It is also found in literature that particles of size 5-20 nm which have low albedo, would be useful for utilizing the strong enhancement of the local field that exists near the NP. The strong near-field will increase the absorption in the surrounding semiconductor and dye, in this case the nano particles would act as effective antennas for

incident light. [20]. There are indications that particles of size 5 nm or less will not participate in scattering of the light [21], therefore this size would be a good choice to separately study the effects of GNPs on the enhanced near field.

Possibilities to modify the quasi-Fermi levels at the Au-TiO<sub>2</sub> anode, and thereby increase the photovoltage by tuning the ratio of TiO<sub>2</sub> and 2 nm GNPs is also reported. In addition, the nanostructure of the TiO<sub>2</sub> layer with inlaid 2 nm GNPs can also effectively reduce the recombination rate due to its mosaic structure, this also leads to enhanced photovoltage [14].

## 2.2 Choice of GNPs for this work

In this work, the GNPs are randomly inlaid into the bulk of the TiO<sub>2</sub> layer at the anode. One advantage of random positioning is that the GNPs might have larger contacting surface for both dye and TiO<sub>2</sub> than if they were placed at the top or bottom of the layer. When the interaction of the GNPs and the dye/semiconductor is considered, the larger contacting surface is especially important because the effects of the enhanced near field of the GNPs is decaying fast with distance to the GNP surface, see equation (25), Section 6.

For the TiO<sub>2</sub> slurries prepared in this work, the GNPs were added into the TiO<sub>2</sub> slurry during the mixing phase, therefore, due to random positioning, effects of enhanced near field from GNPs considered as separate particles as well as effects of plasmon coupling due to GNPs close to each other would be expected. The resulting effect would then be a sum of separate and coupled plasmons.

In this work, GNPs of size; 2, 5, 10 and 40 nm were initially chosen to be used in different amounts and combinations with different dyes to study the effects of GNPs dispersed in the anode of DSSCs. This choice of GNP sizes was based on the reported results described above [13, 14, 15, 17, 18, 20, 13, 14].

The amount of GNPs used in the solar cells in this work is referred to as Au relative surface area. The meaning of this is the ratio of gold and TiO<sub>2</sub> used in the preparation of the TiO<sub>2</sub> slurry that is used to produce TiO<sub>2</sub> films. The ratio is defined as:

$$\frac{\text{total gold nanoparticle surface area } [cm^2]}{\text{mass of TiO}_2 [g]} \quad (1)$$

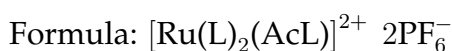
Other references as mass of gold or number of particles per mass of TiO<sub>2</sub> could have been used but the relative surface area reference was chosen because the plasmonic effect that was to be studied, is a surface related effect. The plasmonic effects are size and shape dependent also, and this is referenced by the different particle sizes used in the experiments.

### 2.3 Photosensitizing dyes

Ruthenium complexes have shown the best PV properties among the metal complexes, they have a good electrochemical stability, they absorb over a broad spectrum, their excited states are relatively long lived and their excited and ground state energy levels are suitable for use in combination with  $\text{TiO}_2$  as semiconductor [22].

For the photosensitization of the cells, three different dyes from Solaronix were chosen:

- **Ruthenizer 455-PF6**, a cationic, orange coloured ruthenium based metal containing organic dye with absorption peak at 455 nm.



Where:

AcL = dicarboxybipyridine

L = bipyridine

- **Ruthenizer 620-1H3TBA**, an anionic, dark green coloured ruthenium based metal containing organic dye with absorption peaks at 620, 536, 411 and 328 nm.



Where:

L' = tricarboxytripyrindine

- **Sensitizer SQ2**, a zwitterionic, blue coloured dye based on the squaraine unit. This dye has one sharp and high absorption peak at 655 nm. This dye belongs to the class  $D\pi A$ .

Where:

D = donor group, A = acceptor group and  $\pi$  = photoreceptor group.

D is negatively charged and has a donor property and A is positively charged and has an acceptor property.

The chosen GNPs have their absorption peaks around 520 nm, so these dyes provide the experiments with a good spread in absorption spectra, especially the 620-1H3TBA which absorbs over the broad interval of 328 to 620 nm. Measured absorption spectra of these dyes are presented in Section 9.1. There might be differences in interaction between GNPs and different dyes due to their different ionicity, GNPs are reported to react stronger with cationic dyes than with anionic ones [23]. In addition, the chemical properties of the dyes are very different and this might influence the reactivity of the GNPs to the dyes differently.

In the first part of this work, experiments were carried out with the aim to see which of these dyes that could produce cells that are the most positively sensitive to addition of GNPs in the anode.

## 2.4 Electrolytes

Issues with short life time and decreased efficiency over time for DSSCs employing liquid electrolytes are well known. Long term stability is a key point for commercialization of solar cells, therefore these issues need to be addressed. These problems are often related to electrolyte leakage and photochemical degradation of dyes, solvents and sealants. The issue with leaking electrolyte can be addressed by using a gel electrolytes with a high content of propylene carbonate (PC) instead. Positive results from experiments using this approach are reported for example in, Biancordo et. al. [24, 25]

In this work a polyacrylonitrile (PAN) based gel electrolyte using tetrahexylammonium iodide ( $\text{Hex}_4\text{N}^+\text{I}^-$ ) as salt was chosen. This is a well tested electrolyte and it is known to produce high open circuit voltage in combination with  $\text{TiO}_2$  as semiconductor [26] and has several other advantages due to the stability of the gel. The choice of the hexylic alkyl chains instead of the propylic which have higher conductivity, is due to the need of reaching the highest  $V_{OC}$ . The proportion of the salt  $\text{Hex}_4\text{NI}$  to PAN was chosen as 120 to 100 as this gave the highest conductivity compared to other proportions [26, 27].

## 2.5 $\text{TiO}_2$ slurry

For the preparation of the  $\text{TiO}_2$  semiconductor, a well tested slurry was chosen. This slurry has been used in different works, both with the doctor blade method and the spin coating method. The slurry is composed of  $\text{TiO}_2$  nanoparticles, carbowax, nitric acid and triton X-100. Preparation methods was followed as described by Bandara et. al. [27, 28, 29]. Different compositions of this slurry were tried and these are declared in Section 8.3.4. For deposition of the  $\text{TiO}_2$  slurry to the transparent conducting oxide (TCO) glass substrates the spin coating method was chosen, and the annealing of the layers were carried out at 450 °C for 30 minutes.



**Part II**  
**THEORY**



## 3 Physics of solar cells

### 3.1 Sunlight

The fuel for all PV devices is electromagnetic radiation and sunlight is a part of the total electromagnetic spectra. Sunlight, like all electromagnetic radiation is composed of photons, which can be regarded as massless particles that can carry energy but not momentum. Photons also exhibits properties of a wavelike character with wavelength  $\lambda$  and frequency  $\nu$ . Sunlight is composed of photons with different wavelengths covering an interval of approximately 250 to 2500 nm, expressed as energy, this equals 4.9 to 0.5 eV. The specific spectrum of the sunlight is affected and changed when it passes through the atmosphere of the earth, see Figure 4 on the following page. The energy carried by a photon,  $E_{ph}$  is related to the wavelength  $\lambda$  and the frequency  $\nu$  as:

$$E_{ph} = h \cdot \nu = \frac{h \cdot c}{\lambda} \quad (2)$$

where  $h$  is Planck's constant and  $c$  is the speed of light.

In the interval of sunlight, the units nm for wavelength and eV for energy are commonly used, a convenient relation between these units is:

$$E_{ph}(eV) \approx \frac{1240}{\lambda(nm)} \quad (3)$$

PV devices of which the solar cell is one type, convert optical energy carried by photons to electrical energy carried by electrons. In the case of solar cells it is the light from the sun that is used as energy source, but basically any electromagnetic radiation will do as carrier and supplier of energy to PV devices. The electromagnetic radiation that is defined as visible light, is in the wavelength interval of approximately 400 to 800 nm, which means 3.1 to 1.55 eV expressed as energy.

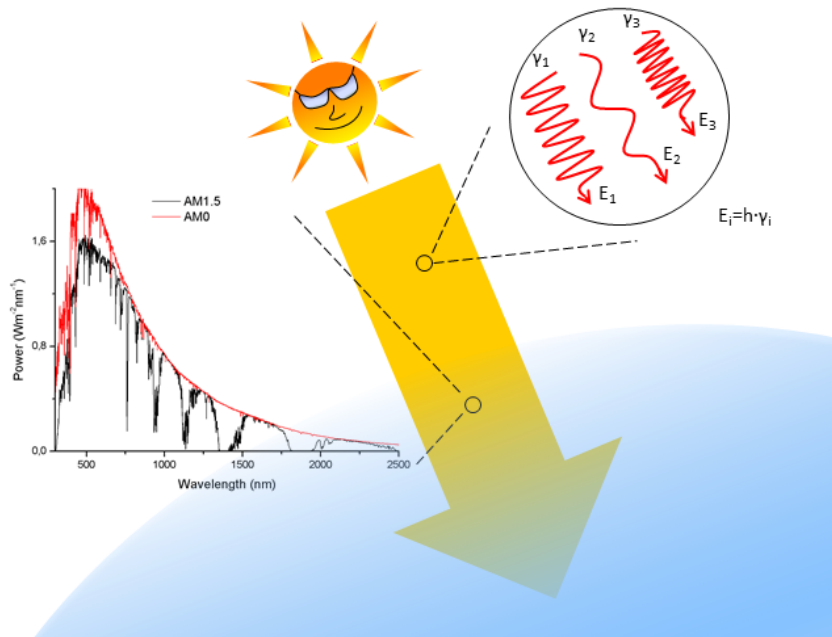


**Figure 4:** The radiation from the sun is composed of photons carrying different amounts of energy. When the light passes through the atmosphere of the earth it is scattered and absorbed by different substances in the atmosphere. The optical properties of the atmosphere changes the specific spectra of the sunlight.

### 3.2 The AM sunlight standard

In the field of solar cells, a notation including air mass (AM) followed by a number is often used for reference when the irradiation used in experiments should be specified. This AM light standard is a reference system for standardization of sunlight irradiation for both terrestrial and extraterrestrial radiation.

The intensity and spectral content of the sunlight are affected when it passes through the atmosphere which is composed of different substances. How the sunlight will be affected by passing the atmosphere is dependent on the composition of the atmosphere, the optical properties of the different substances and the actual path length.

One way to describe the atmospheric light path is the use of the relative optical path length, this is however a generalization because it assumes homogeneous and isotropic composition of the atmosphere. This relative measure is referred to with the notation AM $x$ , where  $x$  is the ratio of the actual path length to the path length with the sun directly overhead (angle of incidence =  $0^\circ$ ). In Figure 5 on the next page, a two dimensional schematic shows how angles, path lengths and AM numbering are defined.

With this system AM1.0 is the irradiance at sea level at  $0^\circ$  angle of incidence and AM1.5 is for the incidence angle of  $\approx 48.2^\circ$ . The radiation just outside the atmosphere is denoted AM0.

Different wavelengths in the sunlight will be affected differently and this makes it difficult to identify an exact definition of the irradiated light at a specific location. It would be necessary to measure the intensity and the spectral content in every measurement to have exact references. The most common method in experiments with solar cells is to use some solar simulator of known optical power and spectral distribution with reference to the AM reference system.

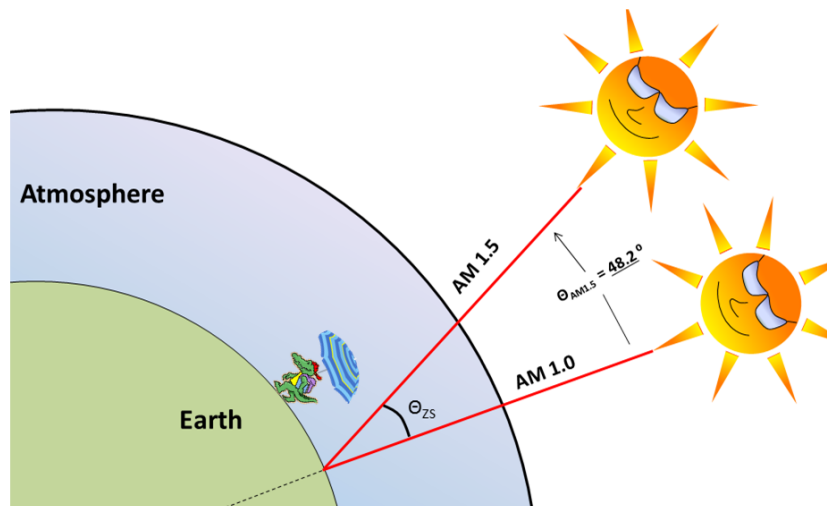


**Figure 5:** Schematic figure of sunlight reaching a position on earth at different incident angles. In the figure the AM1.0 and AM1.5 are shown, the incident angle for the AM1.5 is  $48.2^\circ$ .

Even if an ideal homogeneous atmosphere is assumed, the calculation of the air mass is complicated. One approximation that is sufficient for most engineering applications is achieved by using some simple geometric considerations. In this case the air mass is calculated as:

$$AM = \frac{1}{\cos \theta_{ZS}} \quad (4)$$

where  $\theta_{ZS}$  is the solar zenith angle which is the angle between the vertical (angle of incidence =  $0^\circ$ ) and the incident light beam [6].

The radiation from the sun can to a good approximation be regarded as radiation from a black body at temperature of 5770 K. The power from this radiation incident on a unit area just outside the atmosphere, at a distance of 1 astronomical unit (AU)<sup>1</sup> from the sun, is denoted as the solar constant  $B_0$ :

$$B_0 = 1367 \text{ (W/m}^2\text{)} \quad (5)$$

In Figure 6 the solar spectra is shown for AM0 sunlight (red) and AM1.5 sunlight (black), the graphs are based on data from the National Renewable Energy Laboratory [30]. The figure clearly shows that the spectrum is significantly changed after passing through the atmosphere. Each wavelength is affected differently, this depends on the wavelength dependence of the extinction coefficients of the substances in the atmosphere, leading to different absorbance at different wavelengths of the light.[6, 31, 30] At higher values of AMx , the absorption due to atmospheric gases will make the gaps in the extraterrestrial radiation deeper.

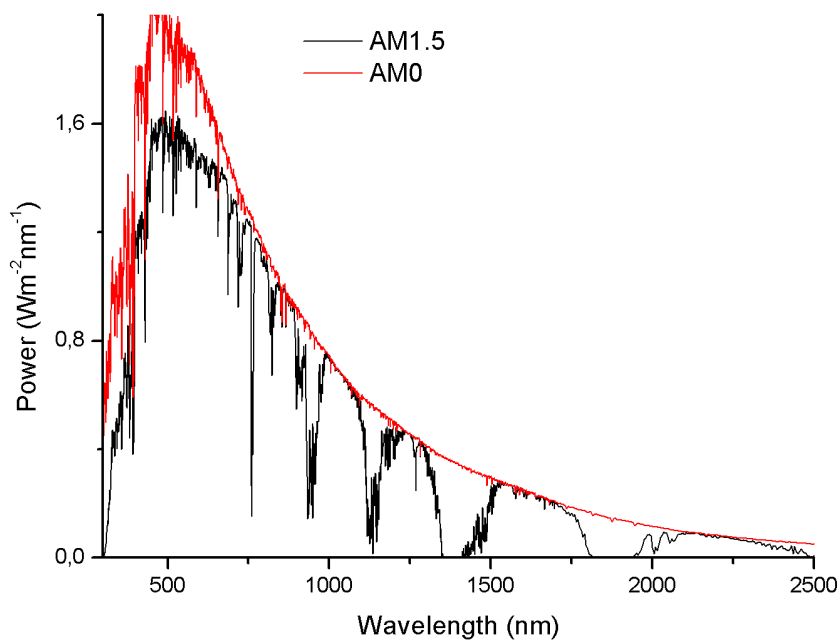


**Figure 6:** Graphs showing reference spectral irradiances for AM0 (ASTM E 490) and AM1.5 (ASTM G 159), spectral data from NREL.

<sup>1</sup> 1 AU=149 597 871 kilometers which equals the distance between the sun and the earth

### 3.3 Working principles of solar cells

#### 3.3.1 General function of a solar cell

Looking from the outside, the function of different types of solar cells are, even though different in efficiency, the same, they convert optical energy into electrical energy. However, a look on the inside reveals that they can be quite different to each other, both in structure and material composition.

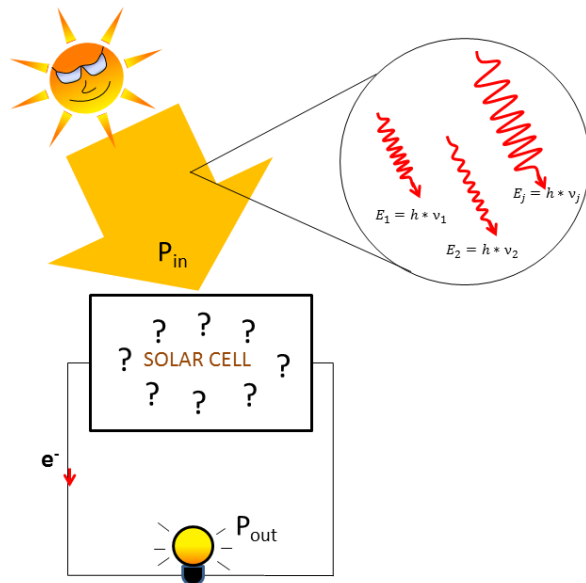
In this text, the general operation of a conventional semiconductor solar cell is presented first and following that, the operation of a dye sensitized solar cell. The aim here is to give an overview of these concepts, a more complete description and understanding would require a quite extensive text.

The most simple type of a solar cell can basically be described as a semiconductor diode that has been designed to absorb light and convert the energy of the photons into electrical energy. A semiconductor has the capacity to absorb light and use a part of the energy carried by the photons to excite electrons in the semiconductor material. When an electron is excited, an electron hole-pair is created and these "particles" will now be the carriers of the energy instead of the photons which do not exist after the absorption-excitation process. Figure 7d on page 23 shows a schematic structure of a simple conventional solar cell. In this figure the top surface is the front of the cell where the irradiating light enters, this surface is often prepared with some anti-reflective coating to get as much light as possible into the device. All light that is reflected at this surface is to be regarded as loss from the irradiated energy.

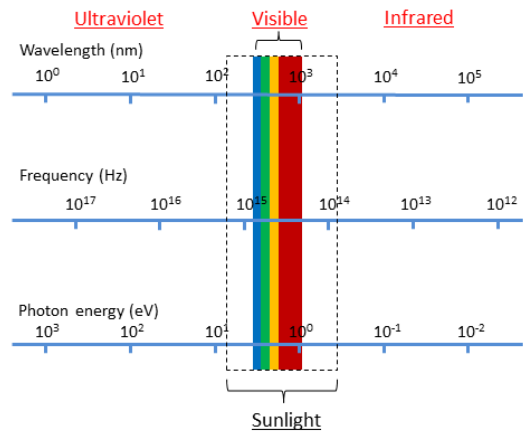
In a semiconducting material, electrons and holes move within separated energy levels. The energies between these limiting levels form so called energybands. The energies between different energy bands form the bandgaps. There are valence bands (VB), where the electrons are bound to the nucleus and conduction bands (CB), where the electrons are more free to move between different nucleus. The amount of energy separating the VB maximum and the CB minimum, called the band gap energy, is denoted  $E_g$  and defines the minimum energy that has to be supplied for an intra-band excitation of an electron. The band gap, which is temperature dependent, can be either indirect where VB maximum and CB minimum are separate in both energy and momentum, or direct, where the VB maximum and CB minimum have the same momentum but are separated in energy, see Figure 7c on page 23. In general, the size of the band gap is different for different materials. For a direct band gap material such as GaAs ( $E_g = 1.43$  eV at 300 K), it is sufficient just to add energy equal to the band gap,  $E_g$  for the creation of an electron - hole pair. For an indirect band gap material such as Si ( $E_g = 1.11$  eV at 300 K), both energy and momentum must be added for an excitation to take place. Photons which just carry energy, can not excite the electrons themselves in an indirect band gap semiconductor, momentum also have to be added and this is

supplied via phonons. The fact that both a photon of sufficient energy and a phonon of sufficient momentum have to be involved, in general makes the probability for an electron excitation lower for the indirect than for the direct band gap material. This is one reason why relatively thick absorbers are needed to achieve sufficient light absorption in solar cells built with indirect band gap materials like Si.

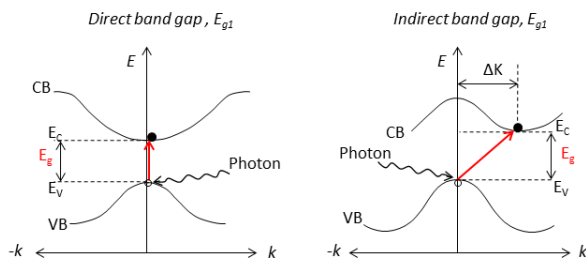
Energy from different photons do not add up spontaneously to required energy for electron excitation. All electrons with less energy than the band gap will just pass through, and the energy carried by them will be lost. When photons of higher energy than the band gap is absorbed, electrons will be excited to energy levels above the CB edge. The electron will then lower its energy within the CB until it reaches the CB edge, the amount of energy between the higher level and the CB edge will in this case be converted to heat and lost. When an electron excitation takes place the photon is annihilated at the same time. The process works in the opposite direction also, if an electron lowers its energy by moving from the CB edge to the VB edge, it will emit a photon with energy equal to the energy of the band gap.



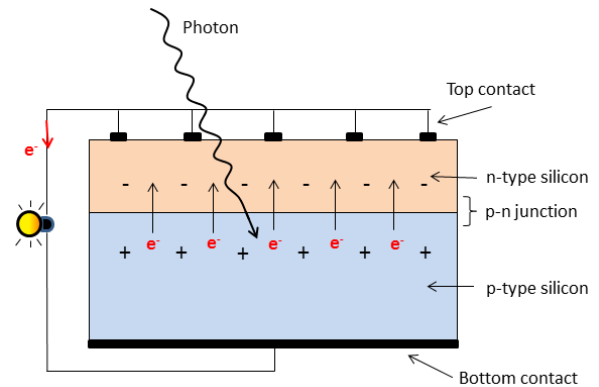
(a) Schematic figure of direct solar energy conversion using a solar cell. The energy carried by the photons in the sunlight is converted to electrical energy carried by the electrons in the circuit without using intermediate steps involving other forms of energy.



(b) The position of visible light and solar spectrum marked in the electromagnetic spectrum. The spectra is shown as function of wavelength, frequency and energy. The relation between the three quantities is  $E = h \cdot \nu = h \cdot c / \lambda$ .



(c) Different types of band gap in a semiconductor. a, Direct band gap, CB minimum and VB maximum occurs at the same momentum. b, Indirect band gap, CB minimum and VB maximum occurs at different momentum



(d) Schematic figure showing one of most simple type of a conventional single junction solar cell. The basic parts along with the central process of hole pair creation are depicted.

**Figure 7:** (a) Direct energy conversion, sunlight energy to electrical energy. (b) Sunlight and visible light spectra positioned in the spectra of electromagnetic radiation. (c) Direct and indirect band gaps. (d) Schematic of simple conventional solar cell.

### 3.3.2 Dye sensitized photoelectrochemical cells

#### The DSSC structure

A dye sensitized solar cell is a photoelectrochemical solar cell (PSC) consisting of; a photoelectrode (anode), a counter electrode (cathode) and an electrolyte containing a redox couple. The semiconductor material in the PSC is attached as a thin layer to the anode. Oxide semiconductor materials such as  $\text{TiO}_2$ ,  $\text{ZnO}$ , and  $\text{SnO}_2$  are often used here because of their good stability under irradiation, the most common among these is  $\text{TiO}_2$ . This semiconductor has a relatively large band gap ( $\sim 3.2$  eV) which hinders effective absorption of visible light [6]. To enhance the absorption of light irradiated into the cell, a photosensitizing dye can be added to the semiconductor in a PSC. The chosen photosensitizer absorbs photons of lower energy than the band gap of the semiconductor and the excited electrons in the photosensitizer are subsequently injected into the CB of the semiconductor. This concept is the archetype of a DSSC. These solar cells are often called Grätzel cells, named after one of the inventors and major expert in this field, Michael Grätzel. In a DSSC the basic processes: excitation of dye, injection of electrons into the semiconductor and regeneration of the dye occurs in a three dimensional structure of semiconductor, photosensitizer and electrolyte. The DSSC counterpart of the band gap in a semiconductor is the difference between the LUMO level and the HOMO level in the photosensitizer molecule. A schematic interior structure of a DSSC completed with relative electron energy levels in different parts of the cell, is depicted in Figure 8.

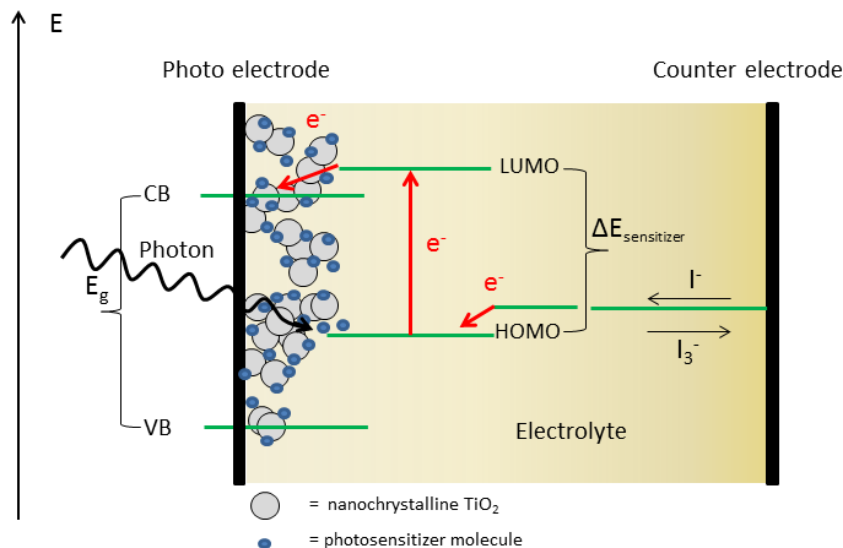


**Figure 8:** Schematic structure of a DSSC showing electron energy levels of the basic processes.  $\Delta E_{\text{sensitizer}}$  and  $E_g$  are the excitation energies of the dye and the semiconductor respectively.

A schematic structure of a DSSC with enlarged parts of the interior showing the relative positions for the different materials is shown in Figure 9

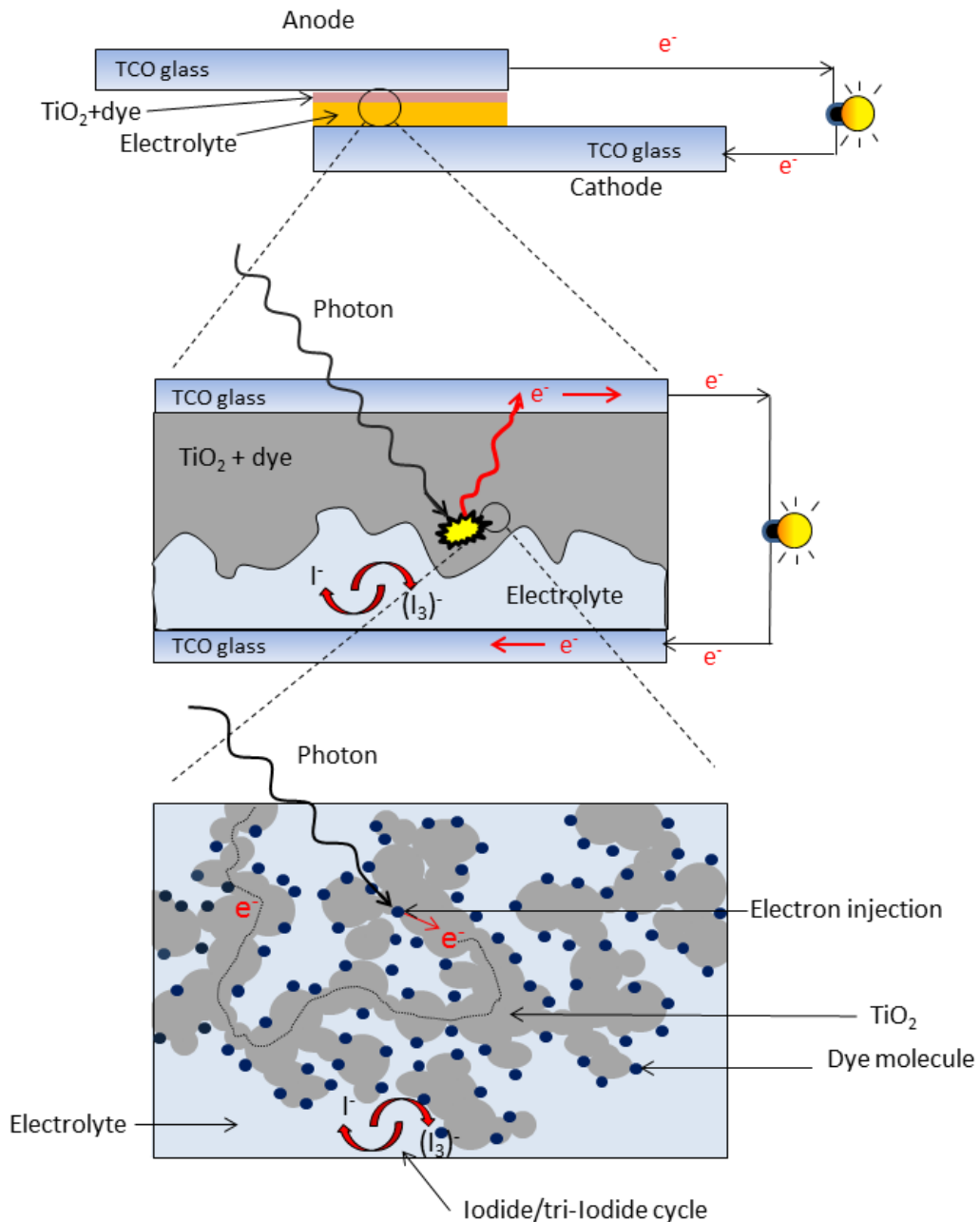


**Figure 9:** Two dimensional schematic structure of a cross section of a DSSC using nanocrystalline  $\text{TiO}_2$  as semiconductor at the anode and an iodide/tri-iodide electrolyte as mediator between the electrodes.

### Primary processes

From the event that a photon is absorbed and an electron is excited from the HOMO level to a LUMO level in the dye, to the event that the dye is regenerated again, there are a series of basic processes that occur in the DSSC and its connected circuit. These processes are marked and numbered in the order they occur in Figure 10, here the DSSC is regarded as an ideal cell without recombinations of charge carriers.

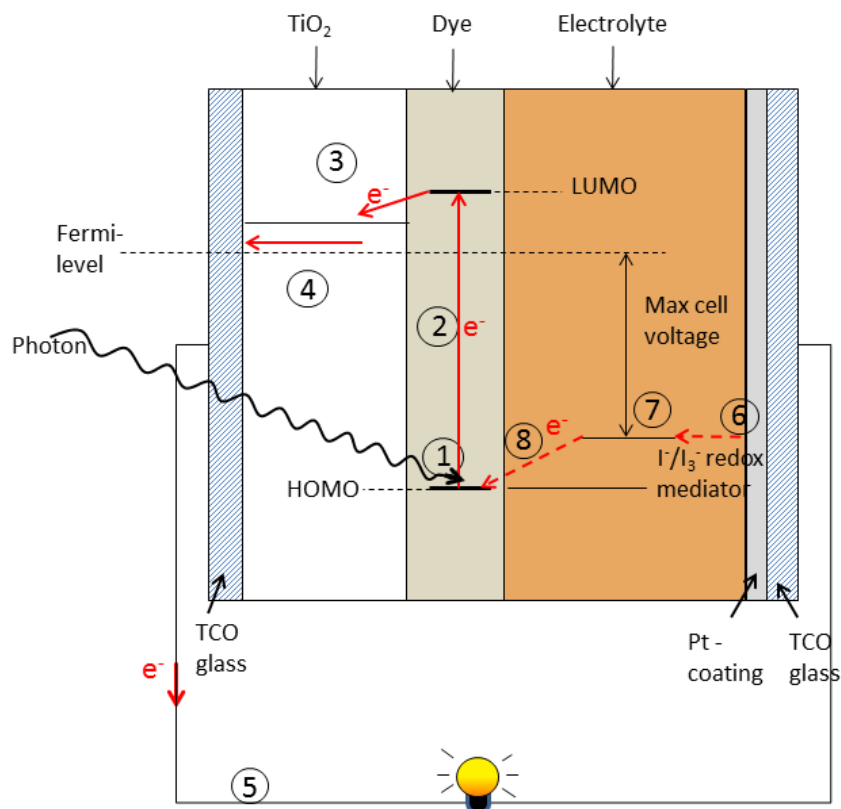


**Figure 10:** Schematic structure of the DSSC using TiO<sub>2</sub> as semiconductor and an electrolyte with I<sup>-</sup>/I<sub>3</sub><sup>-</sup> as redox mediator. The primary processes within the cell are marked and numbered in the order they occur during operation.

The ideal DSSC processes shown in Figure 10 are [32, 6]:

1. The photosensitizing dye absorbed in the TiO<sub>2</sub> layer at the anode absorbs photons with energy equal to or higher than the energy difference between the ground state, S (HOMO level) and the excited state, S\* (LUMO level) in the photosensitizer.

2. Energy from the photon is used to excite the electron to the LUMO level or higher in the photosensitizer.



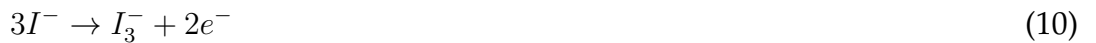
3. The excited electrons are injected into the CB of the  $\text{TiO}_2$ , the dye molecule is oxidized at the same time.



4. The injected electrons in the CB moves between the  $\text{TiO}_2$  nanoparticles by diffusion until they reach the TCO glass at the anode.
5. Electrons are moving from the anode to the cathode passing via the connected load where they perform work and lose energy.
6. At the interface between the platinum treated TCO glass and the electrolyte, the oxidized mediator  $\text{I}_3^-$  is reduced to  $\text{I}^-$  ions.



7.  $\text{I}^-$  ions diffuses through the electrolyte towards the oxidized photosensitizers in the  $\text{TiO}_2$  layer.
8. Oxidized photosensitizers are reduced with electrons from the  $\text{I}^-$  ions which at the same time is oxidized to  $\text{I}_3^-$ .



There are four energy levels in the DSSC that significantly affects the performance of the DSSC; the ground state (HOMO level) and the excited state (LUMO level) of the photosensitizer; the Fermi level of  $\text{TiO}_2$  electrode, located close to the CB edge, and the mediator ( $\text{I}^-/\text{I}_3^-$ ) redox potential in the electrolyte. The HOMO-LUMO energy gap, analogous to the band gap for inorganic semiconductors determines the photocurrent in the DSSC. The smaller this energy gap the more of the long wavelengths of the light can be utilized and therefore more current can be produced. The energy of the LUMO level must be negative enough compared to the  $\text{TiO}_2$  CB level for the injection of electrons to work efficiently. The HOMO level must be positive enough compared to the redox potential of the ( $\text{I}^-/\text{I}_3^-$ ) mediator for the oxidized dye to effectively receive electrons. The cell voltage of the DSSC is developed by the energy gap between the Fermi level in the  $\text{TiO}_2$  and the redox potential in the electrolyte [6, 33].

### Recombination of charge carriers

The processes described in the paragraph above did not include any recombinations of charge carriers, however, in real cells, recombinations are always present to some degree. In a recombination process, excited charge carriers are transported back to ground states without performing any work in the connected circuit, therefore recombinations are always to be considered as losses, lowering the performance of the cell. For a DSSC there are direct recombinations within the photosensitizer, but also recombinations of injected electrons from the  $\text{TiO}_2$  CB to oxidized photosensitizers and to acceptors in the electrolyte and also from the TCO glass to the electrolyte. In Figure 11, the direct recombinations within the dye and recombinations from The  $\text{TiO}_2$  are depicted, the typical time constants for the excitation and recombination processes are also given.

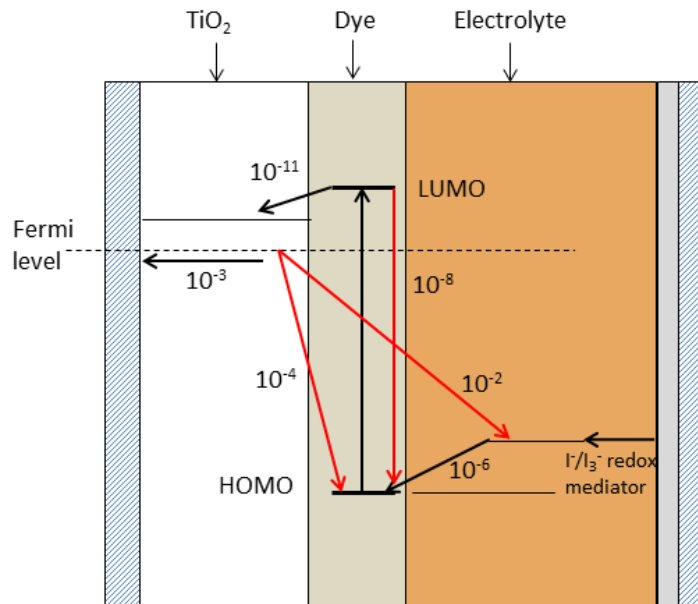


**Figure 11:** The kinetic data, given in seconds, for the desired electron transfer processes (black) and the recombination processes (red) in the DSSC.

### 3.4 Limitations of performance

The performance of solar cells are limited by different factors comprising both practical issues like material quality as well as physical phenomena. During the energy conversion there are many processes going on simultaneously in a solar cell, the efficiency of which, varies from one process to another and they all need to be optimized to achieve the best overall cell efficiency. Figure 12 shows in a rough outline how incoming energy is distributed between theoretical maximum harvested energy and different losses for a single junction silicon solar cell [34].

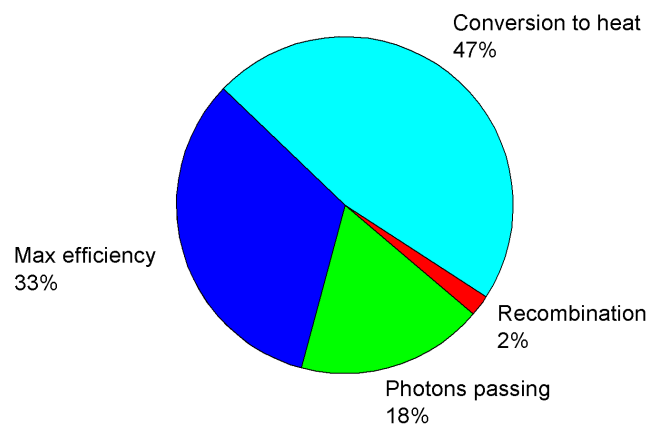


**Figure 12:** Pie chart showing the distribution of the incoming energy between theoretical maximum photon to electron conversion ( $\sim 33\%$ ) and different losses.

The figure shows that, with direct conversion of sunlight energy into electrical energy using a single junction solar cell, at most  $33\%$  of the incoming energy can be converted into usable electrical energy

#### The Shockley Queisser limit

The most central of the limiting physical phenomena originates from the nature of the sunlight in combination with the energy band structure in semiconductors. In 1961 the two scientists William Shockley and Hans Queisser first described the theoretical maximum efficiency of single junction PV devices powered by sunlight.

To realize that there is such a limit the following can be considered;

1. A semiconductor can only absorb photons with energy equal to or larger than the band gap energy,  $E_g$ .
2. The sunlight which mainly covers wavelengths between 250 and 2500 nm is composed of photons carrying different energies. For each wavelength, the photons have a specific energy and flux.

When a semiconductor with band gap energy  $E_g$  is irradiated with sunlight, all photons with energy equal to  $E_g$  is absorbed and will excite electrons to the CB minimum which can be delivered directly to the outer circuit, i.e. for these photons there could be 100 % efficiency.

All photons with energy lower than  $E_g$  will not be absorbed at all, i.e. 0 % efficiency for these photons. All photons with energy larger than  $E_g$  will be absorbed and excite electrons to energy states above the CB min. in the semiconductor, from these higher states the electrons will lower their energy until they reach the CB minimum and then be delivered to the outer circuit, in this case the excess energy will be lost mainly to heat. For these photons the efficiency will be dependent on the energy they carry.

To increase the efficiency, a semiconductor with smaller  $E_g$  can be used to absorb more of the low energy photons, but the energy lost to heat in the semiconductor will increase simultaneously. If a semiconductor with larger band gap is used less energy is lost to heat but more of the lower energy photons will just pass through and their energy will be lost. So there is a trade-off between energy lost to heat and energy totally lost due to photons passing through without being absorbed at all, the balance between these two losses are dependent of the size of the semiconductor band gap.

It was showed by Shockley and Queisser that there is a theoretical efficiency limit for photon to electron conversion for a single junction PV device and this limit is specific for each wavelength. The highest theoretical value for a single junction PV device used under AM1.5 light condition is  $\sim 33\%$  and this value is reached at  $\sim 1100$  nm (1.11 eV). [34, 35]

To achieve efficiencies higher than the SQ limit, there are some alternatives to explore:

- Multi-junction solar cells (MJSCs); junctions of different materials and different band gap are arranged in series inside the PV device, allowing the light to react separately in the different layers. Due to their different band gaps, more of the photons can be absorbed with less energy loss. MJSCs are often used in combination with light concentrators. For this method a best efficiency of 46 % was reported from the Fraunhofer institute in 2014 [36].

- The irradiating light can be split into different wavelength intervals and PV devices with suitable band gap can be used for each interval.
- Different techniques to sensitize the photoactive material that absorbs the light, this technique basically implements more than one junction into the same device.
- Combine PV semiconductors with heat technology to harvest the heat produced by electrons excited to levels above the band gap minimum.

### Some other limitations

As mentioned before, solar cells exist in many different concepts and each type has its specific limitations. However, there are limitations that can be regarded as quite general also. In the following summary, both general and specific criticalities and suggested methods how to address them are presented.

- **Low photon flux into the photoactive material**, (general).  
Antireflective coating, structured surfaces, metal nanoparticles at surfaces for increased in-coupling of light, light concentrators [37, 38, 39].
- **Poor absorption of light in the photoactive materials**, (general)  
Sensitizing dyes, MNPs, quantum dots, nano structured surface at the back electrode [17].
- **Direct recombination within the photosensitizer**, (DSSC).  
Finding the right combination of photosensitizer and semiconductor materials to ensure fast injection of electrons into the semiconductor.
- **Recombinations of charge carriers from the TCO glass to the photosensitizer and electrolyte**, (PSC, DSSC)  
Using blocking layers of compact semiconductor material or oxide to prevent contact between the electrolyte/dye and the TCO glass [40].
- **Recombinations at semiconductor surfaces**, (general)  
Passivation of surfaces [41].
- **Low mobility of the charge carriers**, (DSSC, general)  
High conductivity electrolyte, low resistance at interfaces and contacts [39].
- **Leakage of electrolyte**, (PSC, DSSC)  
Better sealing methods, using gel electrolytes instead of liquid ones [27].

This work was focused on the effects of adding GNPs into the photoactive material in the anode. The aim with this approach was to improve the absorption of photons and the photon to electron conversion.



## 4 Characterizing properties of solar cells

To characterize a solar cell by its properties, some measurements have to be done. The most common measurement for this is the I-V measurement, this provides data to calculate; efficiency, open circuit voltage, short circuit current and fill factor. Depending on the used measurement methods, other parameters like capacitance can also be calculated. The efficiency can be further specified as an overall efficiency and two types of quantum efficiencies; internal and external. All the different properties above provide important information about the ongoing processes in the solar cell. To be able to compare between different measurements, the different properties mentioned above as well as the conditions for the experiments needs to be defined unambiguously.

### 4.1 Measuring and testing conditions

When the performance of a solar cell is to be measured and referred to it is most often the efficiency of the device that is measured. To be able to measure efficiency of a solar cell, the optical power irradiating the cell must be known. To achieve comparable results that can be reported and referred to, it is of greatest importance to use standardized methods and conditions that can be unambiguously referred to. The need for such a referring system led to the concept of the Standard Reporting Conditions (SRC), sometimes also referred to as the Standard Test Conditions (STC). The SRC concept consists of the total irradiance, the spectral irradiance under which the performance is measured and the temperature of the photovoltaic device [42]. In table 2 the standard reporting conditions for terrestrial and space applications is shown.

Table 2: Standard Reporting Conditions

Application	Reference spectral irradiance	Total irradiance [W/m <sup>2</sup> ]	AM notation	Temp. [°C]
Low earth orbit	ASTM E 490	1366.1	AM0	28
Terrestrial global	ASTM G 159	1000	AM1	25

The "low earth orbit" in Table 2 is referred to as the conditions just outside the atmosphere and the "terrestrial global" as the conditions at sea level with the sun directly overhead, zenith angle = 0°.

When performance of solar cells are reported the irradiation conditions are often referred to using the AM classification which was described in section 3.2.

### 4.2 I-V characteristics of a solar cell

A common method to perform the characterizing I-V measurements is to apply a voltage to the electrodes of a solar cell under illumination while the current is measured. By

sweeping the voltage from open circuit voltage,  $V_{OC}$  to 0, the current will vary between 0 and short circuit current,  $I_{SC}$ . Another way is to connect the solar cell under illumination to different load resistances between 0 and infinite resistance, while measuring both voltage and current. Both these methods will produce the so called I-V characteristics for the cell and from this data a lot of important information about the performance of the cell can be evaluated. In Figure 13, an I-V graph is plotted with some of the important properties marked.

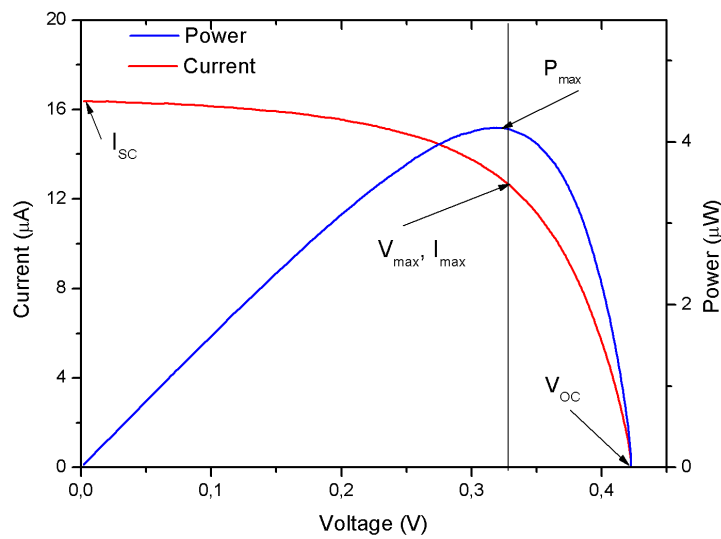


**Figure 13:** The characteristic I-V graph for a solar cell with the calculated power included. In the figure the open circuit voltage  $V_{OC}$ , short circuit current  $I_{SC}$ , max power  $P_{max}$ , voltage at max power,  $V_{max}$  and current at max power  $I_{max}$  are marked.

### 4.3 Efficiency

When a solar cell is characterized, it is the performing properties that is considered, i.e. properties connected to how efficient the energy conversion from optical energy to electrical energy is performed. Solar cells and their functionality are quite complicated and there are a few properties involved that one way or the other will affect the efficiency. From an end user perspective it is basically just one property of interest and that is the power efficiency,  $\eta$ , defined as:

$$\eta = \frac{\text{maximum output electrical power (W)}}{\text{input optical power (W)}} \quad (11)$$

To calculate the power efficiency, the only things needed are the measurements of the incident optical power and output electrical power. The optical power can be measured using calibrated optical sensors with known responsivity for each wavelength and a monochromator. This way the power can be measured at each wavelength and the sum of all contributions will give the total power incident on the solar cell. The output electrical power is determined by measuring current and voltage at the output terminals of the solar cell and calculate maximum power as the maximum value of the product ( $V \cdot I$ ).

The light source used for the experiments was a solar simulator from LOT-Oriel. The power of the light from the simulator was  $1000 \text{ W/m}^2$ , this was measured using a calibrated light detector, see Appendix B. The efficiency of the solar cells can be summarized in the following equation:

$$\eta = \frac{P_{max}}{P_{in}} = \frac{(I \cdot V)_{max}}{P_{in}} \quad (12)$$

Where:

$P_{max}$  is the maximum output power of the cell.

$P_{in}$  is the input optical power of the light.

$(I \cdot V)_{max}$  is the product of I and V at the point of maximum power.

#### 4.4 Fillfactor

One figure of merit that is often used is the fill factor (FF), it informs how close to the theoretical maximum value the cell performs. The highest theoretical value of power for a solar cell is the product of the  $V_{oc}$  and the  $I_{sc}$ , in practice this value is never achieved. To get a measure of how close the performance is to the ideal value, the ratio of actual power and max theoretical power is used, this ratio is defined as the fill factor:

$$FF = \frac{P_{max}}{I_{sc} \cdot V_{oc}} = \frac{(I \cdot V)_{max}}{I_{sc} \cdot V_{oc}} \quad (13)$$

The values for  $V_{oc}$ ,  $I_{sc}$ ,  $V_{max}$  and  $I_{max}$  are obtained from the I-V measurements, see fig 13.



## 5 Modelling of solar cells

A solar cell is a photovoltaic device that converts optical energy in light directly into electrical energy using no intermediate steps. The basic operation of the solar cell is to absorb incoming photons, use the energy of the photons to raise the energy of electrons inside the photoactive material in the cell, and finally, letting the electrons do electrical work in a closed outer circuit. This energy conversion is in many ways very complicated, involving several different physical processes, each one with specific properties and issues.

To better understand and describe the complex processes and how measurable quantities relate to each other, the solar cells are often modelled with equivalent electrical circuits which are easier to analyse and understand. These models, constructed with electrical components of known properties also makes it possible to theoretically estimate and predict results. This way, effects of new ideas might be evaluated without actually building complete solar cells for test and evaluation. The general concept of solar cells, comprises a variety of different types as it was shown in Section 1.4 and to cover all situations, each type would need a specific model. Here, two basic, general models and one specific model for dye sensitized solar cells are presented.

### 5.1 The ideal solar cell model

An ideal solar cell can be modelled as a current source in parallel with a diode as it is shown in Figure 16a on page 39. The current source represents the current produced in the cell which is proportional to the light intensity. In the ideal model, parasitic losses are not existing and the I-V characteristic is described by the Shockley equation for a diode and a current source [31]:

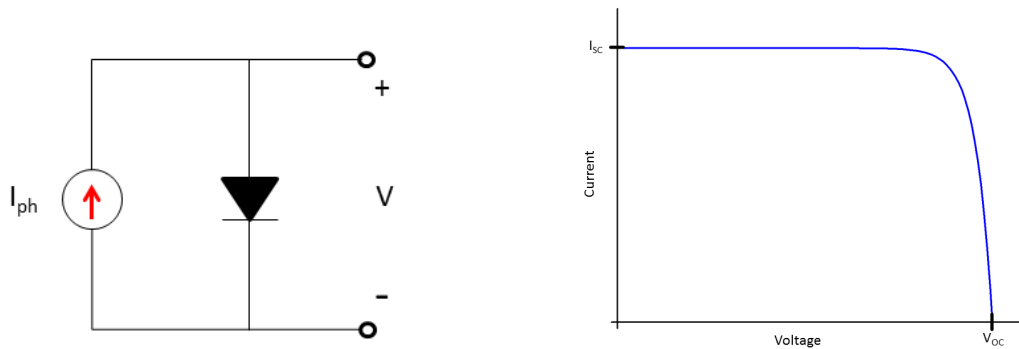
$$I = I_{ph} - I_0 \left( e^{\frac{qV}{k_B T}} - 1 \right) \quad (14)$$

where,  $k_B$  is Boltzmann's constant,  $q$  is the charge of the electron,  $T$  is the absolute temperature,  $V$  is the voltage across the cell terminals,  $I_{ph}$  is the generated photocurrent and  $I_0$  is the diode saturation current. The I-V characteristic of this model circuit is shown in Figure 16b on page 39.

Equation 14 is valid for an ideal diode behaviour, in practise the dependence on  $V$  is modified by an ideality factor  $n$  which describes how close to ideal diode behaviour a cell works. Typical values of  $n$  is, above 2 for DSSCs and between 1 and 2 for Si solar cells. Using the ideality factor to compensate for non-ideal behaviour of the diode, the equation for the model becomes:

$$I = I_{ph} - I_0 \left( e^{\frac{qV}{nk_B T}} - 1 \right) \quad (15)$$

In the remainder of this text, ideal diode behaviour is assumed and  $n$  is set to 1.



(a) The equivalent electric circuit for the ideal cell consists of a current source and an ideal diode, the current source represents the produced photocurrent  $I_{ph}$  within the cell.

(b) The I-V graph described by the Shockley equation, equation 14 on the previous page.

**Figure 14:** a, Equivalent circuit of an ideal solar cell. b, I-V graph for the ideal solar cell model.

## 5.2 Simple realistic solar cell model

When a solar cell is operating under realistic conditions, the performance will be affected by internal resistances, also called parasitic resistances. The efficiency will be decreased due to power dissipation in these internal resistances and the I-V graphs from the non ideal solar cells will look a bit different compared to the ideal one shown in Figure 16b on the facing page.

To model the non-ideal behaviour, more components are usually added into the circuit model for the ideal case. In Figure 15 on the next page, a simple model of a cell including internal parasitic resistances is depicted. In this model, a series resistance ( $R_s$ ) and a shunt resistance ( $R_{sh}$ ) are added. The series resistance corresponds to contact resistances at interfaces, sheet resistance of the TCO glass and charge carrier mobility limitations in the materials. The shunt resistance corresponds mainly to charge recombinations in the cell. For an ideal cell  $R_s$  would be zero and  $R_{sh}$  would be infinite [43, 37].

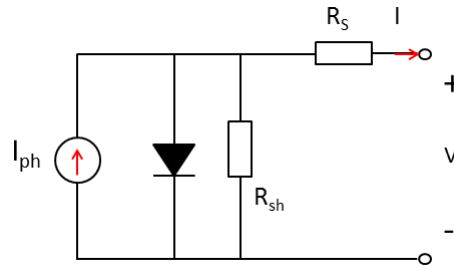


**Figure 15:** The equivalent circuit model for a photovoltaic cell with the components  $R_s$  and  $R_{sh}$  included to represent the parasitic resistances within the cell.

For the model with added non ideal components, the equation for the I-V characteristic is expanded with one term and is now written as [19, 31, 37]:

$$I = I_{ph} - I_0 \left( e^{\frac{q(V + IR_s)}{k_b T}} - 1 \right) - \frac{V + IR_s}{R_{sh}} \quad (16)$$

As mentioned above, the efficiency of the solar cells will be affected by the non ideal properties and the shape of the I-V graph will be changed. The two parasitic resistances will affect the shape of the I-V graphs in different ways, this is illustrated in Figure 16, however, in both cases the fill factor is reduced. The graphs show that there are correlations between the resistances and the derivatives  $(\partial V / \partial I)_{I=I_{SC}}$  and  $(\partial V / \partial I)_{V=V_{OC}}$ . The tangential values of the I-V graph at the current and voltage axes are called dynamic shunt ( $R_{sh0}$ ) and series resistances ( $R_{s0}$ ) respectively.

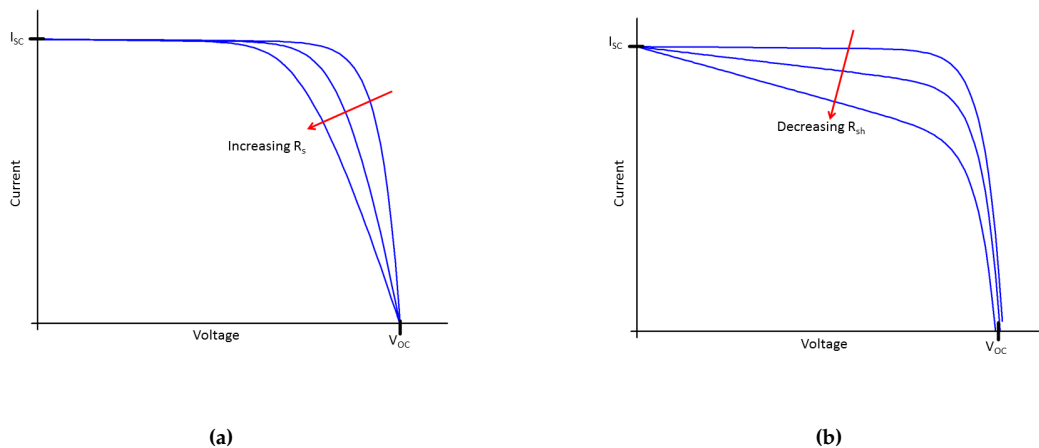


**Figure 16:** a, Effects of parasitic series resistance and b, effects of parasitic shunt resistance in the cell. In both cases the fill factor of the cell will be reduced by these parasitic resistances.

### 5.3 Dye sensitized solar cell model

The dynamic resistances  $R_{sh0}$  and  $R_{s0}$ , has been successfully used to calculate solar cell parameters [44]. The non-ideal resistances directly affects the efficiency and fill factor, therefore this information is valuable when results are evaluated and discussed. This is a useful tool because the dynamic resistances can be calculated directly from measured data. For comparative studies where the absolute values are not essential, it can be sufficient to use only the dynamic shunt and series resistances.

For dye sensitized solar cells which are quite complicated devices, the modelling and construction of equivalent electrical circuits becomes more complex. Using analysis of equivalent circuits is an important tool for high performance DSSC design and several equivalent models for DSSCs can be found in literature [45, 46, 47]. One model for evaluation and calculation of solar cell properties of DSSCs are presented by Guliani et. al. [45]. This model which also contains additional RC circuits to model non-idealities is shown in Figure 17. In this model resistance  $R_1$  is related to diffusion of ions within the electrolyte and it is proportional to the distance between the TCO and the Pt counter electrode. Resistance  $R_2$  is related to charge transfer processes at the Pt counter electrode. The capacitances  $C_1$  and  $C_2$  are related to Helmholtz double layers at the electrodes.  $R_{sh}$  is related to electron back transfer from  $TiO_2$  to electrolyte at the  $TiO_2$ /dye/electrolyte interface.  $R_s$  is related to sheet resistance at the TCO glass substrate.

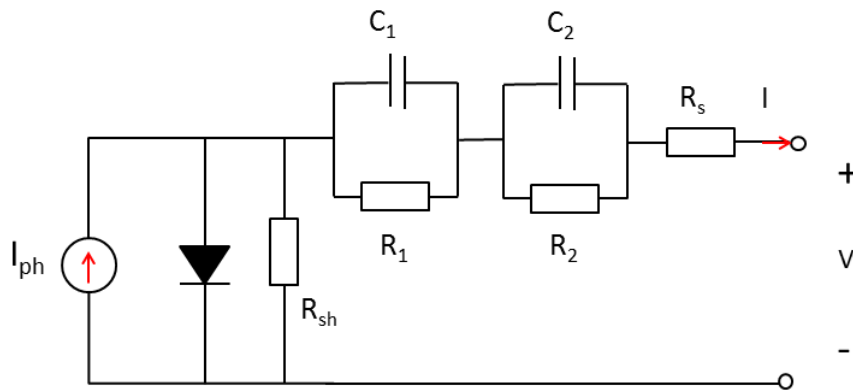


**Figure 17:** The equivalent circuit model for a dye sensitized solar cell with additional circuitry to compensate for non-idealities.

The work by Guliani et. al. shows that calculations based on this model are in good accordance with their experimental results.

## 6 Localized surface plasmon resonance

The central part of this work is about using GNPs to improve performance of dye sensitized solar cells, this brings the topic into the field of localized surface plasmon resonance (LSPR) which is the result of bringing metal nanoparticles<sup>1</sup> into an electromagnetic radiation. In this case the radiation is the light that irradiates the solar cells.

Colloids of noble metal nanoparticles are characterized by intense colors, which are caused by scattering and absorption of visible light. The scattering and absorption properties which vary from one noble metal to another, are also dependent of size and shape of the particles. Early examples of applications using these phenomena can be found in old church windows, where gold and silver nanoparticles were mixed into the glass to give them beautiful colors. These effects are caused by the LSPRs which is one of the most important types of interaction between metal particles and electromagnetic radiation.[48]

Characteristic for metals is that they have free electrons in the conduction bands, able to move almost freely and independent of the ionic background which can be considered only as scattering centres. If a metal particle is placed in an electric field, the electrons surrounding the nucleus will be subjected to a force directed against the field. For an oscillating field, this force will also be oscillating. This will make the electrons move from one side to the other in a movement that is perpendicular to the propagation of the field, this is illustrated schematically in Figure 18 on the following page. As the electrons are displaced in this oscillating way, there will also be an oscillating displacement of charge at the surface of the particles. This oscillating surface charge will cause an enhancement of the electric field in the vicinity the particle. For particles with irregular shape there will be especially strong enhancement of electric field near tips and corners.

When metal nanoparticle structures of size 10 - 100 nm are subjected to light, they will interact with the light through collective excitation of electrons caused by inter-band electron transitions. Resonances can occur when the frequencies of the incident light and the resonance frequencies of the electronic oscillations match each other. The result is a collective and coherent oscillation of the electronic cloud surrounding the metal particle called a plasmon. During this interaction between radiation and the nanoparticle, energy can be stored in the oscillation and this might cause absorption and/or scattering of the incident light.

---

<sup>1</sup> nano particles = particles of size 1 - 100 nm

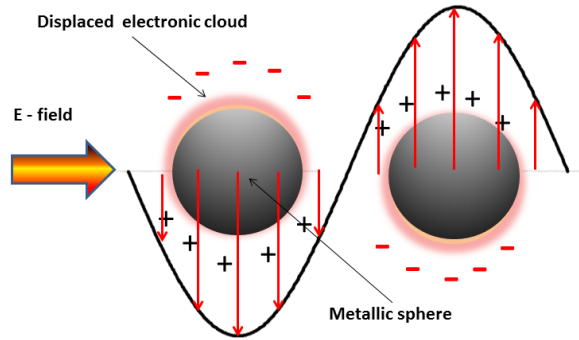


**Figure 18:** Illustration of momentary displacement of the electrons due to the surrounding oscillating electric field.

Plasmonics is part of the field of nanophotonics<sup>1</sup>. The basis for plasmonics is the interaction between electromagnetic radiation and the conduction electrons at metallic interfaces [49]. This section presents some of the fundamental results of LSPRs involving a spheric metal NP in an electromagnetic field. The presentation is a summary of some known results from theoretical work in this field and more detailed descriptions are found in the given references. It should also be noted that these results are valid under the simplified conditions mentioned in the text (spherical particles, wavevector,  $\vec{K}=0$  and wavelength  $\gg$  particle size), however, these conditions serve well for gaining an insight of what is going on when light interacts with small metallic particles.

First some definitions, when a small particle is interposed into a beam of parallel light, several distinct effects can be observed [50].

- Some of the energy contained in the beam can be converted into other forms of energy, this phenomena is known as absorption.
- Part of the incident energy can be extracted and then scattered in all directions at the same frequency as the incident light, this is called elastic scattering.
- When absorption and scattering takes place, the energy of the incident light is reduced by an amount equal to the sum of the absorbed and scattered energy, this reduction is called extinction.

One central relation in the discussion of interactions between electromagnetic radiation and its surroundings is the dielectric function  $\varepsilon(\vec{K}, \omega)$  which describes the relation between the relative permittivity  $\varepsilon$  and the conductivity,  $\sigma$ .

$$\varepsilon(\vec{K}, \omega) = 1 + \frac{i\sigma(\vec{K}, \omega)}{\varepsilon_0\omega} \quad (17)$$

<sup>1</sup> nanophotonics is the study of interaction between light and objects on the nanometer scale

where  $\vec{K}$  is the wavevector,  $\omega$  is the frequency of the field,  $\epsilon_0$  is the permittivity of vacuum and  $i$  is the imaginary unit <sup>1</sup>. When interaction between light and metals is considered, this expression can be simplified to the limit of spatially local response, this is done by setting  $\vec{K} = 0$

$$\Rightarrow \varepsilon(\vec{K} = 0, \omega) = \varepsilon(\omega) \quad (18)$$

This simplification is valid as long as the wavelengths are much longer than the typical mean free path of the electrons or the size of the unit cell in the metal[49].

In a quasi-static approximation for the case of a spheric nanoparticle it can be assumed that the incoming electric field is constant over the volume of the sphere, this is valid as long as the wavelength is much larger than the diameter of the sphere. This approximation allows to simplify this to a problem of a particle in a static electric field. Taking a simple model as an example, a metallic, homogeneous sphere of radius  $a$  is considered in an electric field. The surrounding is considered as non absorbing with a real dielectric constant  $\epsilon_m$  and the Drude model [51], is used for the electrons. Following calculations by S. Maier [49] and Bohren& Huffman [52], the potential, polarizability, electric field and effective cross section areas can be described by equations (19) to (27) in the following paragraphs.

### Potential and polarizability

In the following expressions the variables  $\theta$ ,  $\vec{r}$  and  $a$  is referred to as in Figure 19.

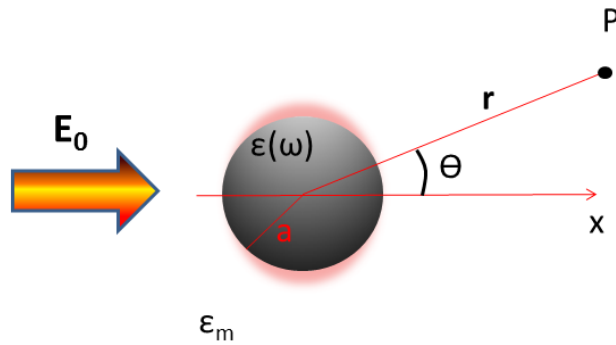


**Figure 19:** Simplified model used for calculations of plasmonic effects from a metal nanoparticle in an electric field. The dielectric function of the sphere and the surrounding is  $\varepsilon(\omega)$  and  $\varepsilon_m$  respectively.

<sup>1</sup> the imaginary unit  $i$  is defined by:  $i^2 = -1$

The electric potential inside and outside of the sphere,  $\phi_{in}$  and  $\phi_{out}$ , and the dipole-moment  $\vec{p}$  are :

$$\phi_{in} = -\frac{3\varepsilon}{\varepsilon(\omega) + 2\varepsilon_m} E_0 r \cos\theta \quad (19)$$

$$\phi_{out} = -E_0 r \cos\theta + \frac{\vec{p} \cdot \vec{r}}{4\pi\varepsilon_0 r^3} \quad (20)$$

$$\vec{p} = 4\pi\varepsilon_0\varepsilon_m a^3 \frac{\varepsilon(\omega) - \varepsilon_m}{\varepsilon(\omega) + 2\varepsilon_0} \vec{E}_0 \quad (21)$$

The dipole moment can also be calculated as:

$$\vec{p} = \varepsilon_0\varepsilon_m \alpha \vec{E}_0, \quad \text{where } \alpha \text{ is the polarizability} \quad (22)$$

Combining equations (21) and (22) the polarizability can be written as:

$$\alpha = 4\pi a^3 \frac{\varepsilon(\omega) - \varepsilon_m}{\varepsilon(\omega) + 2\varepsilon_m} \quad (23)$$

This expression has a resonance when  $\text{Re}(\varepsilon(\omega)) = -2\varepsilon_m$ .

From equation 23 and 22 it is shown that the polarizability is enhanced at a certain frequency of the field, this frequency is dependent on the dielectric properties of the surroundings,  $\varepsilon_m$ .

## Electric field

The electric fields in and outside of the sphere are:

$$\vec{E}_{in} = \frac{3\varepsilon_m}{\varepsilon(\omega) + 2\varepsilon_m} \vec{E}_0 \quad (24)$$

$$\vec{E}_{out} = \vec{E}_0 + \frac{3\vec{n}(\vec{n} \cdot \vec{p}) - \vec{p}}{4\pi\varepsilon_0\varepsilon_m} \frac{1}{r^3} \quad (25)$$

where  $\vec{n}$  is the unit vector in the direction of  $\vec{r}$ . From equation (25) it is shown that the additional part of the electric field from the plasmonic effect decays as  $\frac{1}{r^3}$  outside the sphere.

**Cross section areas**

The effective scattering cross section area for absorption and scattering of the particles can be calculated:

$$A_{abs} = k \operatorname{Im}(\alpha) = 4\pi k a^3 \operatorname{Im} \left( \frac{\varepsilon(\omega) - \varepsilon_m}{\varepsilon + 2\varepsilon_m} \right) \quad (26)$$

$$A_{sc} = \frac{k^4}{6\pi} |\alpha|^2 = \frac{8 - \pi}{3} k^4 a^6 \left| \frac{\varepsilon(\omega) - \varepsilon_m}{\varepsilon(\omega) - 2\varepsilon_m} \right|^2 \quad (27)$$

where  $k$  is the magnitude of the wavevector of the light,  $k = 2\pi/\lambda$ .

From equation 26 and 27; the cross section areas for scattering and absorption of the NPs are increased with increasing particle size and the scattering cross section area has the strongest dependence on particle size.

**Shape dependence**

The results shown above are valid for a spherical metal NP. If there is an elongation of the particle, the optical properties will be affected significantly. The grade of elongation is identified with the aspect ratio  $r$ , which is defined as the ratio of length and width of the particle:

$$r = \frac{\text{length of particle}}{\text{width of particle}} \quad (28)$$

The dependence on the surface plasmon absorption maximum,  $\lambda_{max}$  of the aspect ratio is described by the relation:

$$\lambda_{max} = 420 + 95 \cdot r \text{ [nm]} \quad (29)$$

This shows that  $\lambda_{max}$  occurs at about 515 nm for a spherical particle and that it will be red-shifted when the particle is elongated[48].



## 7 Enhancing the performance of a DSSC

Positive effects of using plasmonics to improve performance of photovoltaic devices have been reported in literature earlier [20, 17, 18]. In this work the focus is on the effects of adding GNPs into the anode material, to study if this might be a promising approach for enhancement of cell performance and to acquire information about the governing mechanisms.

The theoretical calculations in [49], presented in section 6 show that both absorption and scattering cross section areas of the NPs are size dependent, therefore effects on photon absorption might also be dependent on the size of the added NPs. It is therefore of great interest to study correlations between GNP size and cell efficiency. The issue of poor absorption has already been addressed by others with positive results, using specific photosensitizing dyes in the anodes of DSSCs. Now the aim is to see if the so called plasmonic effects from GNPs in combination with sensitizing dyes might enhance the absorption even more, especially of the longer wavelengths in the light spectra.

The plasmonic effect of metal NPs in electromagnetic radiation is explained briefly in section 6. The interaction of different processes involving energy transfer in the photoactive material are very complicated and not yet understood in detail. However, some possible mechanisms of plasmonic enhancement of solar cells, connected to improved absorption in absorbers of less thickness are depicted in Figure 20 on the following page and described as [20]:

- Using metallic nanostructure at the back surface to redirect the light waves into longer pathways in parallel with the surfaces, this will increase the probability for photon absorption [20], Figure 20a.
- Photoemission of charge carriers, an electron - hole pair is created when the plasmon resonance excitation decays within the nanoparticles and the electron is injected to the semiconductor material[53], Figure 20b.
- Near field effects, metal NPs working as antennas to collect more of the the longer wavelengths in the spectra and couple the plasmonic near-field to the semiconductor or the photosensitizing dye, increasing the effective cross section area for absorption[54], Figure 20c.
- Far field effects, metal NPs working as scattering elements to trap the propagating lightwaves and forcing them into longer pathways inside the absorber, increasing the probability for absorption, Figure 20d.

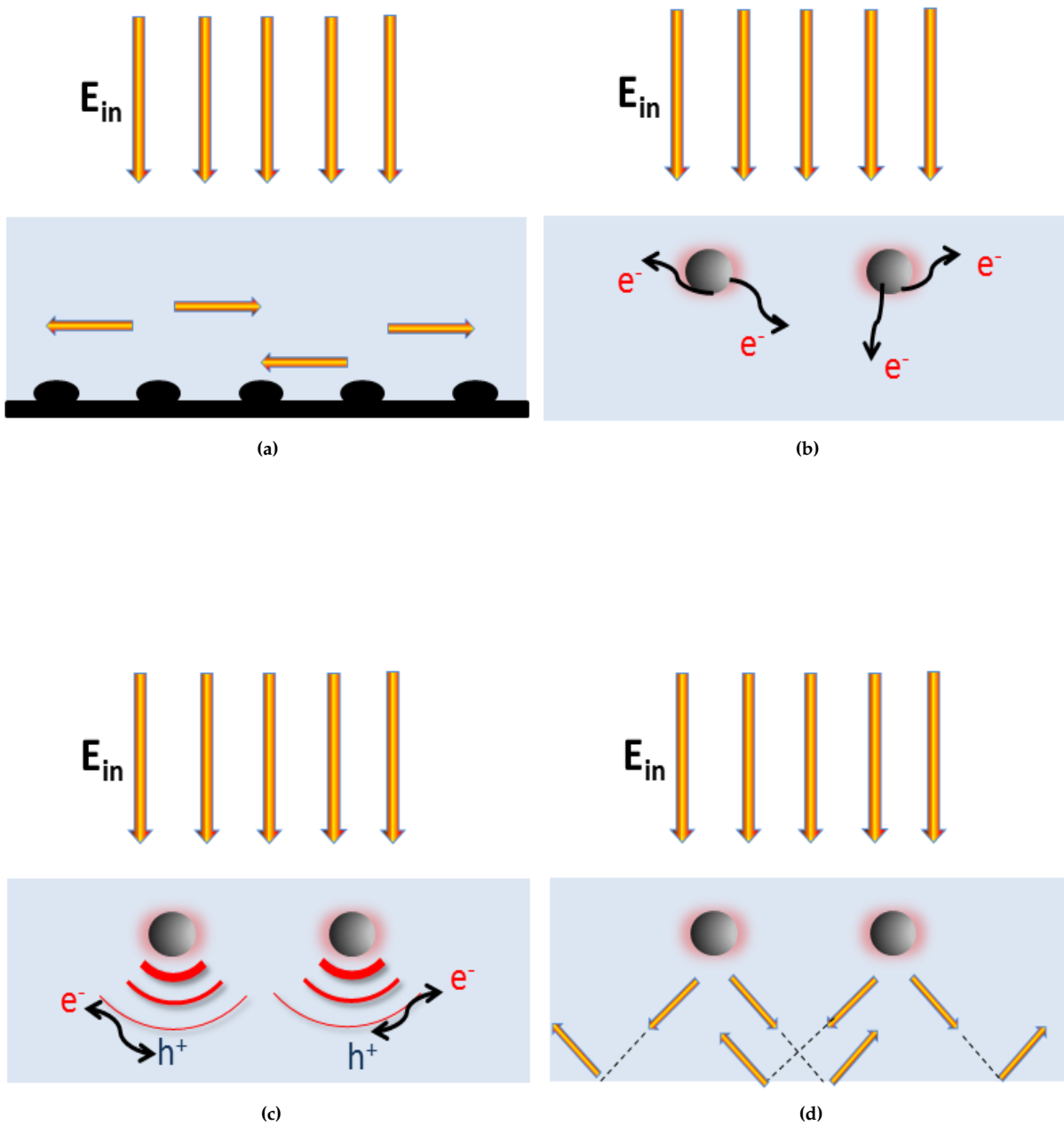


**Figure 20:** Four different ways to use plasmonics for enhancing photon to electron conversion in a solar cell. (a) Metallic nanostructures at the back surface guide the light waves into longer paths, parallel to the surface. (b) Plasmon resonance excitations decay inside the metal NP, causing the creation of electron hole pair. (c) Metal NPs acting like antennas, collecting more of the longer wavelengths and create enhanced nearfields round the NPs. (d) Far field effects increase the scattering cross section area of the nanoparticles.

**Part III**  
**EXPERIMENTAL**



## 8 Experimental

The chemicals used in this work are presented in table 3 on the next page. Methods and equipment used for preparation and characterization of both materials and assembled solar cells are declared and described in detail in Section 8.3.

Additional studies were carried out with the aim to verify and to standardize processes involved in the experiments.

- The dynamic temperature response and the residual temperature error of the annealing furnace was studied for different heating programs. See details in appendix A.
- The solar simulator was tested for light intensity stability in time and homogeneity of intensity within the light beam cross section area, at a recommended working distance, using standard light sensors. See details in appendix B.
- A study of how capacitive properties of DSSCs affects linear voltammetric measurements with the potentiostat equipment was made. See details in appendix C.

## 8.1 Chemicals

The chemicals used in this work are listed in Table 3.

**Table 3:** Chemicals used in this work. The table is divided according to applications and shows short name, chemical/product name and molecular weight. The manufacturing companies are listed in the footnote

Short name	Chemical/Product name	Molecular formula	Molecular weight <sup>1</sup> [g/mol]	Application
EC	Ethylene carbonate <sup>2</sup>	C <sub>3</sub> H <sub>4</sub> O <sub>3</sub>	88.06	Electrolyte
PC	Propylene carbonate <sup>3</sup>	C <sub>4</sub> H <sub>6</sub> O <sub>3</sub>	102.09	
Hex <sub>4</sub> NI	Tetrahexylammonium iodide <sup>7</sup>	C <sub>24</sub> H <sub>52</sub> IN	481.58	
PAN	Polyacrylonitrile <sup>7</sup>	(C <sub>3</sub> H <sub>3</sub> N) <sub>n</sub>	53.06	
I <sub>2</sub>	Iodine <sup>7</sup>	I <sub>2</sub>	253.81	
2 nm GNP	EM.GC2 <sup>4</sup>	Au	1.21 · 10 <sup>-2</sup>	Gold colloid
5 nm GNP	EM.GC5 <sup>4</sup>		6.32 · 10 <sup>-2</sup>	
10 nm GNP	EM.GC10 <sup>4</sup>		5.76 · 10 <sup>-2</sup>	
40 nm GNP	EM.GC40 <sup>4</sup>		5.82 · 10 <sup>-2</sup>	
TiO <sub>2</sub>	Aeroxide TiO <sub>2</sub> P25 <sup>5</sup>	TiO <sub>2</sub>	79.86	TiO <sub>2</sub> layer
Triton	Triton X - 100 <sup>7</sup>	C <sub>14</sub> H <sub>22</sub> O(C <sub>2</sub> H <sub>4</sub> O) <sub>n</sub>	647.00	
Carbowax	MTO - Carbowax 1540 <sup>6</sup>	H <sub>2</sub> O(C <sub>2</sub> H <sub>4</sub> O) <sub>n</sub>	1540	
Nitric acid	Nitric acid <sup>7</sup>	HNO <sub>3</sub>	63.01	
Ethanol	Ethanol <sup>7</sup>	C <sub>2</sub> H <sub>5</sub> OH	46.07	
Isopropanol	2-propanol <sup>7</sup>	C <sub>3</sub> H <sub>7</sub> OH	60.10	
DW	Deionized water <sup>8</sup>	H <sub>2</sub> O	18.02	
455-PF6	Ruthenizer 455-PF6 <sup>9</sup>	C <sub>32</sub> H <sub>24</sub> O <sub>4</sub> N <sub>6</sub> S <sub>2</sub> P <sub>2</sub> F <sub>12</sub> Ru	947.56	Dye
620-1H3TBA	Ruthenizer 620-1H3TBA <sup>9</sup>	C <sub>69</sub> H <sub>117</sub> O <sub>6</sub> N <sub>9</sub> S <sub>3</sub> Ru	1364.70	
SQ2	Sensidizer SQ2 <sup>9</sup>	C <sub>41</sub> H <sub>46</sub> N <sub>2</sub> O <sub>4</sub>	630.81	

<sup>1</sup> For the gold colloids, mass of gold per liter gold colloid [g/L]. <sup>2</sup> Fluka <sup>3</sup> Sigma-Aldrich <sup>4</sup> BBI solutions <sup>5</sup> Degussa <sup>6</sup> Supleco <sup>7</sup> Solveco <sup>8</sup> From lab tap <sup>9</sup> Solaronix

## 8.2 Experimental equipment

In this section the most important parts of the experimental equipment are described. Each presented device is declared with some details of function and performance relevant to this work along with a short description of how it was used.

### Solar simulator

In the characterizing of solar cells, a solar simulator, LS0106 from LOT Oriel was used to irradiate the cells. The light source within this simulator is a 150 W Xenon arc lamp. To better resemble natural sunlight of AM 1.5 standard, the light is passed through a filter with suitable absorption bands, this filter also absorbs some of the peaks in the Xenon arc spectra. Explanation and illustration of the AM 1.5 standard sunlight is given in the theory part, Section 3.2.

The solar simulator is declared to produce a light beam with diameter of 35 mm in a working plane at a distance of 8 - 11 cm from the collimating lens. A schematic figure of the solar simulator and its main components is depicted in Figure 21.

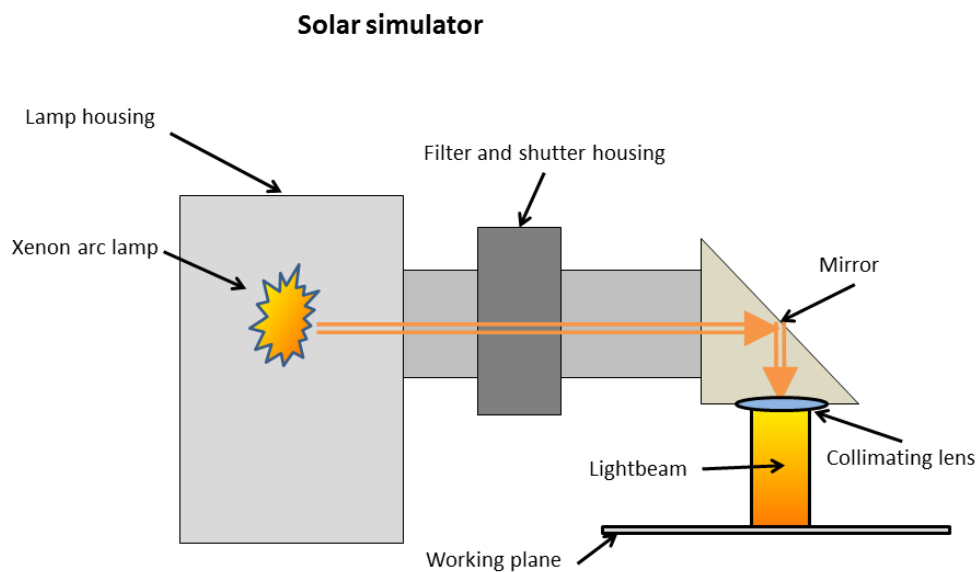


**Figure 21:** Schematic cross section figure of the Lot LS 0106 solar simulator used to irradiate the cells during I-V measurements.

To evaluate the reliability of the results from one measurement to another, the performance of the solar simulator was studied with respect to stability of output optical power and homogeneity of the light beam. Here the homogeneity is considered with respect to measured optical power in the working plane within the light beam cross section area. The study is described and the results are presented in Appendix B. Based on the results from that study it was decided to use the same position for the samples in all measurements and that a warm up period of 30 min should be used prior to measurements. The chosen position was the center of the light beam in the working plane. Practical arrangements for the solar simulator and the sample holder were made to ensure a proper accuracy in the positioning of the samples.

### Potentiostat

For the characterizing measurements of the solar cells, an eDAQ potentiostat, model EA 161 in connection with and an eDAQ e-corder data acquisition unit, model 401 was used. The potentiostat and the e-corder connected to a computer with the eDAQ software: EChem, Chart and Scope, form a complete set-up for potentiostatic measurements where all controlling parameters are set directly from the computer. The equipment can be used in different modes as; potentiostat - applying potential while measuring the current, galvanostat - applying current while measuring the voltage, zero resistance ammeter (ZRA) and high impedance voltmeter (high Z).

Some technical data of this instrument: max data acquisition rate, 200 kHz; max voltage sweep rate, 1000 mV/s; current ranges of 2 nA to 100 mA, resolution of 16 bits (0.0015%) within each range; low pass filters at 10 kHz, 1 kHz, 100 Hz and 10 Hz. In this work 10 Hz filtering was used during all cell characterizing measurements to eliminate mains hum.

The potentiostat equipment with belonging software, offers many features and settings to be chosen by the user. Some examples of these settings are; data acquisition rates, signal filtering and definitions of applied signals. It is also possible to define time delayed measurements which is very useful when time dependent signals are applied to objects with impedance that is not purely ohmic, the use and advantages of time delayed measurements are discussed in Appendix C. The windows in the EChem software used to set parameters for the applied voltage ramp and the delayed current measurement are shown in Figure 22 on the facing page.

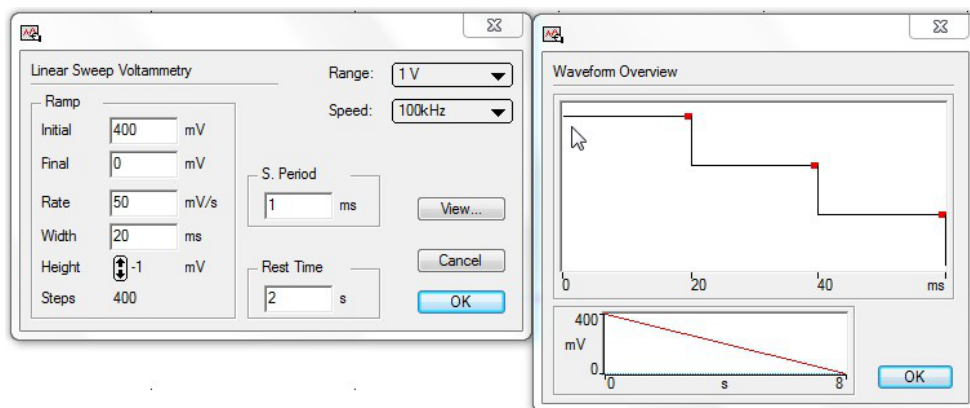


**Figure 22:** EChem windows used for setting the parameters for the applied voltage ramp and the delayed measurement of current. In this case a ramp starting at 400 mV, linearly decreasing to 0 V with a rate of 50 mV/s is set. The actual decrease of the voltage is done in steps defined by the settings. The sampling rate is 100 kHz and the current sampling period is 1 ms. The right window is a graphic representation of the settings and it shows the steps of the voltage ramp and the position of the current measurement in relation to the voltage step.

In this work the equipment was mainly used with the EChem software set in potentiostat mode for measuring I-V characteristics of the cells. Used this way the potentiostat was set to apply a user defined voltage ramp to the electrodes of the cells while measuring the produced current. The high data acquisition rate and the many possibilities to define the measurements, makes this equipment very suitable for dynamic I-V characterizing measurements.

The data from the measurements can be saved in different formats, making evaluation with different software possible. Figure 23 on the next page shows a schematic picture of a solar cell I-V characteristic measurement set-up, using the potentiostat connected to a computer. The set-up shows the instrument connected in the potentiostatic mode.

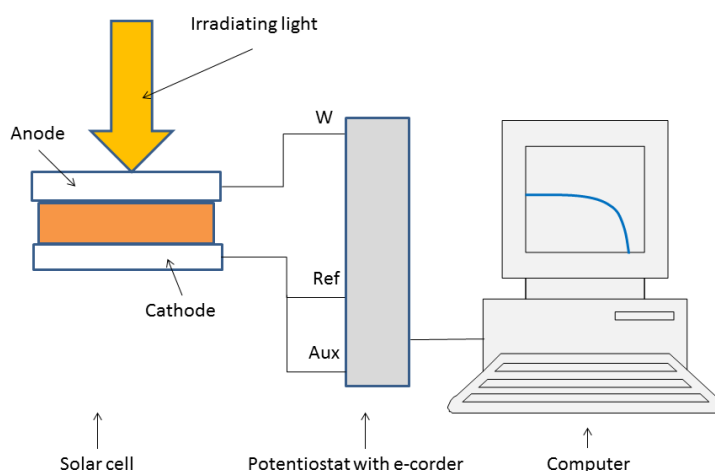


**Figure 23:** Schematic figure showing the set-up and connections of the potentiostat for the characterizing I-V measurements of solar cells. The shown set-up is for measuring in potentiostatic mode.

### Spin coater

The spin coating of the  $\text{TiO}_2$  onto the TCO glass substrates was performed using a Photo Resist Spinner Model 4000 from Electro Micro Systems Ltd. This spin coater equipment consist of a bench top spinner, a remote control unit and a vacuum pump. The control unit and the spinner is connected by flexible cables. With this equipment the spin coating process can be performed in different steps at different speeds. Three independent automatically sequenced spin operations of different duration and speed could be chosen. This spin coater offers speeds between 100 and 6200 rpm and duration between 1 and 650 s at each step. Chosen parameters for a spin process can be stored in a program to facilitate repeatability of sample preparation, maximum 99 programs can be stored in the memory at the same time. The glass substrates which can be up 5 inch in diameter, are fixed in the right position to the chuck by a vacuum. In this work glass substrates of 2 by 4 cm were used in all spin coating processes.

### Spectrometer

The instrument used for spectroscopic measurements was a Perkin Elmer Lambda 900 UV/VIS/NIR Spectrometer<sup>1</sup>. This instrument features a double-beam, double monochromator, ratio recording optical system and covers a wavelength range from 190 to 3300 nm. Two light sources are used to cover the entire working wavelength range, one deu-

<sup>1</sup> UV = ultra violet, VIS = visible and NIR = near infra-red part of the spectrum

terium lamp (UV) and one halogen lamp (VIS/NIR). The instrument is controlled via a computer where different parameters such as: slit size, scan speed, data interval and integration time are set to optimize the measurements. The instrument is equipped with two separate sample holders, one for the sample and the other one for the reference. For liquid samples, cuvettes are used to position the samples correct. The reference sample is needed to compensate for background signal due to the solvents used and the material of the cuvettes and also to compensate for intensity oscillations of the light source. In this work, quartz cuvettes were used, with 10 mm path length for the dyes and 1 mm path length for the gold colloids.

### **Hewlett Packard Impedance Analyser 4192A LF**

To perform impedance measurements on the electrolytes an impedance analyser (IA), Hewlett Packard model 4192A LF was used. The impedance analyser measures impedance by applying a voltage to the sample at different frequencies while measuring the current. By analysing the phase and amplitude difference between the applied voltage and the measured current the impedance can be calculated. The HP 4192A LF has a frequency range of 5 Hz to 13 MHz. Frequency interval and data acquisition rate are set from a computer that controls the instruments.

To perform measurements on a gel electrolyte sample, a special designed sample holder consisting of two polished stainless steel electrodes encapsulated in a plastic tube, see figure 24 on the following page, was used. In this sample holder the electrolyte was pressed between the two electrodes and the plastic tube effectively prevented the electrolyte from leaking out. The diameter of the sample was set by the diameter of the electrodes and the only thing to be noted here was the thickness of the sample which is needed for the calculation of the conductivity. A suitable sample thickness here is between 0.5 and 1 mm. The thickness was measured with a micrometer.

The HP 4192A LF was controlled by a N.I. LabVIEW program which made it possible to automatically scan a frequency range from 5 Hz to 13 MHz at user specified sampling rate during the measurements.

To measure impedance at different temperatures the sample holder was placed in a isolated chamber where the temperature could be controlled. The temperature was measured with a type K (Ni/Cr vs Ni/Al) thermocouple connected to a digital voltmeter.

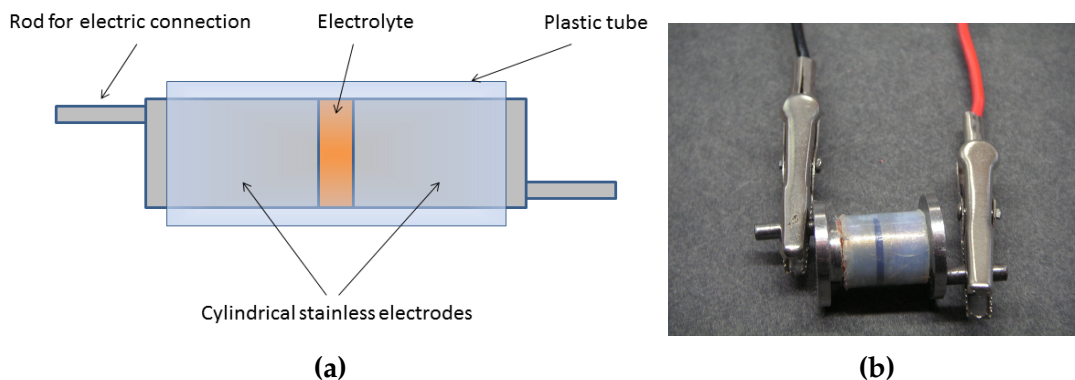


**Figure 24:** Arrangements for conductivity measurements on gel electrolyte. (a) Schematic figure showing the different parts of the sample holder used for impedance measurements of the electrolyte. (b) Photograph of the sample holder used in the measurements.

## Software

Different software has been used for different applications in this work. To control instruments:

- **eDAQ EA161 potentiostat:**  
EChem and Chart.
- **Perkin Elmer lambda 900 spectrometer:**  
UV WinLab.
- **HP 4192A LF impedance analyser and heating chamber:**  
LabVIEW with a program constructed by Ingvar Albinsson.

### 8.3 Preparation of materials

As a preliminary phase in the experimental work, some materials were prepared and characterized in the following way:

- The gold colloids were characterized with absorption spectroscopy and their stability in low pH was studied.
- Dyes were prepared to desired concentrations and characterized with absorption spectroscopy.
- Electrolytes were prepared following strict protocols, and characterized with impedance measurements from which the conductivity was calculated.
- The anode electrodes were prepared by spin coating with TiO<sub>2</sub> based slurry and subsequently, carefully annealed and stained with sensitizing dyes.

#### 8.3.1 Gold nanoparticles

The gold nanoparticles were delivered as suspended in water with a coating of citric acid. This coating which was made by the manufacturer in the synthesis of the Au nanoparticles, confers a net negative charge on the Au nanoparticles which makes them repel each other and stay in solution. Data of the gold colloids is shown in Table 4.

Four different colloidal suspensions containing GNPs of sizes; 2, 5, 10 and 40 nm were first characterized with absorption spectra. These spectra were to be compared with the absorptions spectra of the selected sensitizing dyes. The aim here was to see what dyes and gold colloids could complement each other to get higher optical absorbance of the cells. The absorption measurements were carried out in the wavelength interval 300 - 900 nm. Measurement data and results are presented in the result section. Based on the results from the absorption measurements, where the 2 nm GNPs showed practically no absorbance, it was decided to use only the 5, 10 and 40 nm GNPs in the main experiments of this work.

**Table 4:** Data of gold colloids. The table shows the technical data of the gold colloids as declared by the manufacturer. The volume units used here refers to the volume of the nanoparticle colloid i.e. the total volume of nanoparticles and water. The surface area is the area of one particle and the total particle surface area is the sum of all particle areas per 1 ml of the specific colloid.

Size [nm]	Particles per ml	Mass of 1 particle [g]	Mass of gold/ml [g]	Moles of gold per L	Surface area per particle [cm <sup>2</sup> ]	Tot. Surface area per ml [cm <sup>2</sup> ]
2	$1.50 \cdot 10^{14}$	$8.08 \cdot 10^{-20}$	$1.21 \cdot 10^{-5}$	$6.16 \cdot 10^{-5}$	$1.26 \cdot 10^{-13}$	18.90
5	$5.00 \cdot 10^{13}$	$1.26 \cdot 10^{-18}$	$6.32 \cdot 10^{-5}$	$3.21 \cdot 10^{-4}$	$7.85 \cdot 10^{-13}$	39.30
10	$5.7 \cdot 10^{12}$	$1.01 \cdot 10^{-17}$	$5.76 \cdot 10^{-5}$	$2.92 \cdot 10^{-4}$	$3.14 \cdot 10^{-12}$	17.90
40	$9.00 \cdot 10^{10}$	$6.47 \cdot 10^{-16}$	$5.82 \cdot 10^{-5}$	$2.96 \cdot 10^{-4}$	$5.03 \cdot 10^{-11}$	4.52

### 8.3.2 Dyes

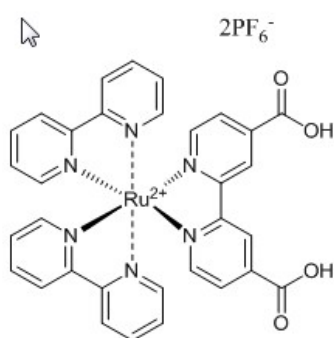
The dyes for used for sensitizing were; Ruthenizer 455-PF6, Ruthenizer 620-1H3TBA and Sensidizer SQ2. The dyes have their peak absorbance at different wavelengths; 455-PF6: at 455 nm, 620-1H3TBA at 620, 415 and 332 nm and SQ2 at about 650 nm. For the staining processes, all dyes were used in concentration 0.3 mM in ethanol. By choosing these dyes the experiments included both metal containing organic and organic dyes of different ionicity.

## Data of the dyes

1. **Ruthenizer 455-PF6**, a Ruthenium based, metal containing organic cationic dye with an absorption peak at 455 nm.

Table 5: Data of the 455-PF6 dye

Dye	Chemical formula	Molecular weight [g/mol]	Absorptionpeak(max) [nm]	Color
Ruthenizer 455-PF6	$C_{32}H_{24}O_4N_6S_2P_2F_{12}Ru$	947.56	455	Orange



(a)

(b)

**Figure 25:** (a) Ruthenizer 455-PF6 molecule. (b) Photograph of Ruthenizer 455-PF6, 0.3 mM in ethanol.

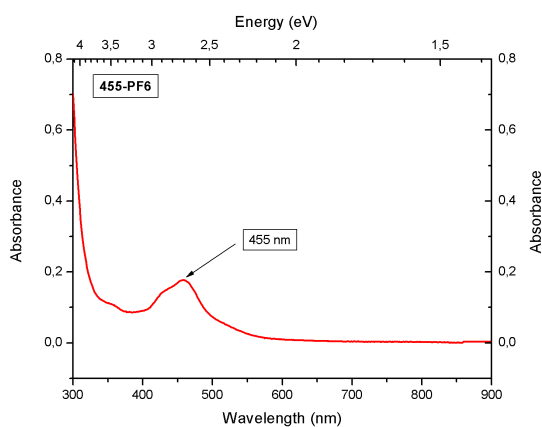


**Figure 26:** Absorptionspectra of Ruthenizer 455-PF6.

2. **Ruthenizer 620-1H3TBA**, a Ruthenium based, metal containing organic, anionic dye with absorption peaks at 328, 411, 536 and 620 nm

**Table 6:** Data of the 620-1H3TBA dye

Dye	Chemical formula	Molecular weight [g/mol]	Absorptionpeak(max) [nm]	Color
Ruthenizer 620-1H3TBA	$C_{69}H_{117}O_6N_9S_3Ru$	1364.7	620	Dark green

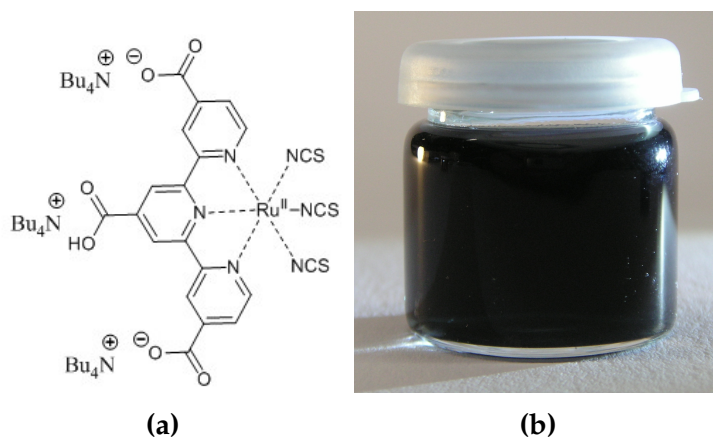


**Figure 27:** (a) Ruthenizer 620-1H3TBA molecule. (b) Photograph of Ruthenizer 620-1H3TBA, 0.3 mM in ethanol.

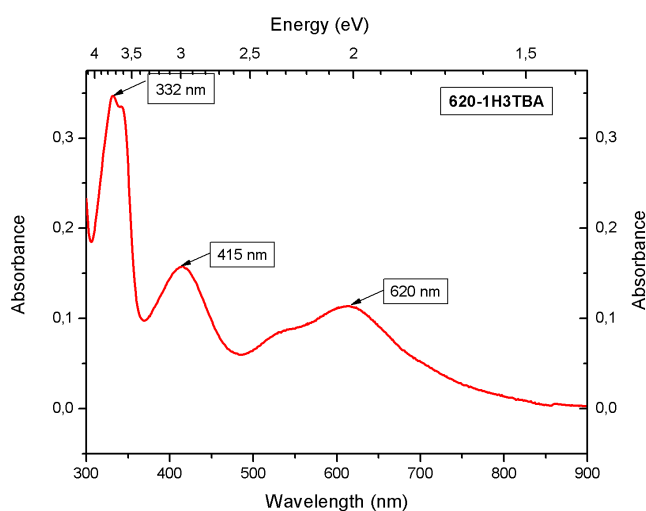
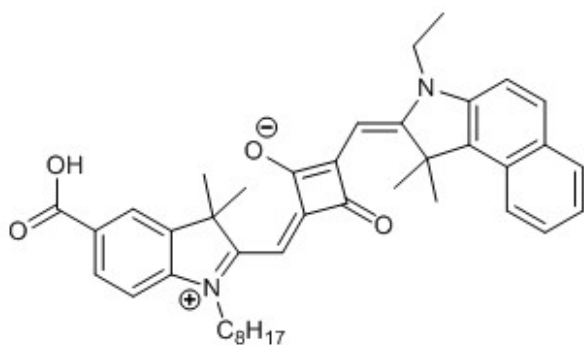


**Figure 28:** Absorptionspectra of Ruthenizer 620-1H3TBA.

3. **Sensitizer SQ2**, an organic, zwitterionic dye containing the squaraine unit, absorption peak at 657 nm.

**Table 7:** Data of the SQ2 dye

Dye	Chemical formula	Molecular weight [g/mol]	Absorptionpeak(max) [nm]	Color
Sensitizer SQ2	C <sub>41</sub> H <sub>46</sub> N <sub>2</sub> O <sub>4</sub>	630.81	620	Blue



(a)



(b)

**Figure 29:** (a) Sensitizer SQ2 molecule. (b) Photograph of Sensitizer SQ2, 0.3 mM in ethanol

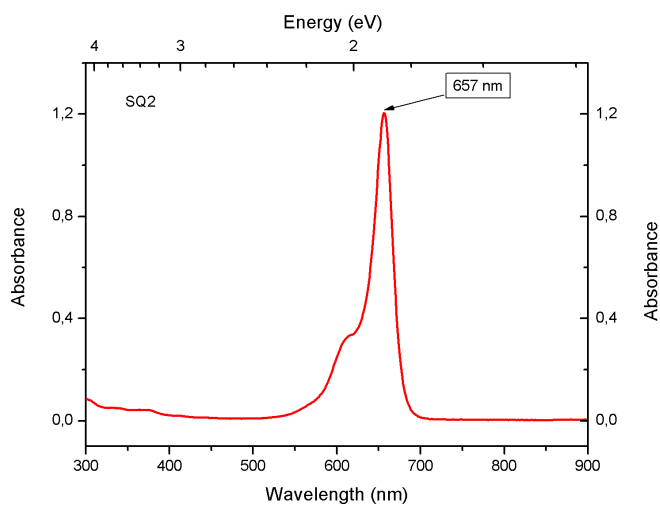


**Figure 30:** Absorptionspectra of Sensitizer SQ2.

The dyes were prepared to a concentration of 0.3 mM in ethanol. Characterization of the dyes were made by measurement of absorption spectra in the wavelength interval 300 - 900 nm (energy interval 4.13 - 1.38 eV) The absorptionspectra for each dye are presented in the result Section 9.1.1.

### 8.3.3 Electrolytes

For this work, a gel electrolyte, Hex120 was used. The composition of this electrolyte is shown in Table 8.

**Table 8:** Composition of the Hex120 electrolyte

Substance	EC	PC	Hex <sub>4</sub> NI	PAN	I <sub>2</sub>
Amount [mg]	400	400	120	100	48

To prepare the electrolyte, EC, PC and Hex<sub>4</sub>NI was mixed in a glass vial and set to stir for 3 h at 50 °C. After that, at a temperature of 40 °, the PAN was added and the mixture was stirred for another 2 h at this temperature. As a last step the iodine was added and the mixture was heated to about 100 °C. After a few minutes at 100 °C, while continuously stirring, the solution became viscous and clear.

After this preparation the electrolyte had gel properties and it was easily shaped by heating to about 50 °C and gently pressing it. Figure 31 shows electrolyte samples before and after heating to gel state

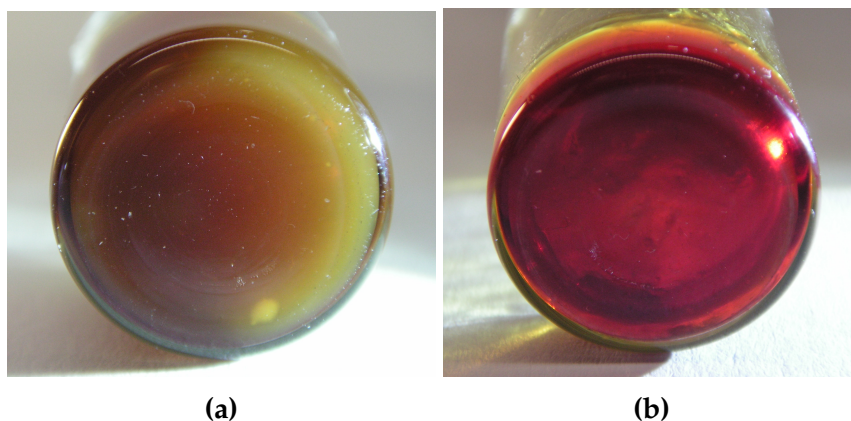


**Figure 31:** Photos of the Hex120 electrolyte. (a) Electrolyte Hex120 before heating to gelation and (b) after heating to gelation

The conductivity of the electrolyte was measured in the temperature range 0 - 60 °C using impedance spectroscopy. The results from impedance measurements and the conductivity calculations are presented in the result section.

### 8.3.4 TiO<sub>2</sub> substrates

The TiO<sub>2</sub> substrate used on the anode side of the cells was produced by spin coating a TiO<sub>2</sub> slurry onto the FTO coated glass. The TiO<sub>2</sub> slurry is composed by: TiO<sub>2</sub> nano particles, nitric acid, Carbowax, Triton, gold colloid and some solvent as for ex. water, ethanol or isopropanol. The semiconductor material is the TiO<sub>2</sub> and it is protonated by the nitric acid, Triton is a surfactant which makes the slurry easier to apply on the substrate glass and Carbowax is used to make the final, calcinated TiO<sub>2</sub> film porous, which facilitates absorption of dye into the TiO<sub>2</sub> film.

The choice of the final composition was based on the properties of the slurry considering the processes of applying and annealing it on the electrode substrate. A series of experiments to try out the best slurry is presented in the next section. The results from that resulted in a final composition of the TiO<sub>2</sub> slurry with gold nanoparticles incorporated. The relative amount of the substances in that final slurry composition is declared in Table 9. The addition of gold colloid limited the possible choices of compositions because the water based colloids were very dilute.

**Table 9:** Final composition of TiO<sub>2</sub> slurry containing gold nanoparticles. In the third column the value of  $x$  can be varied between 0 and 1, for  $x=1$ , the full amount of gold colloid was added and for  $x=0$ , no gold colloid was added. I.e. the total weight of gold colloid and deionized water (DW) was always 1120 mg.

Substance	TiO <sub>2</sub>	HNO <sub>3</sub> 1M	Gold colloid· $x$ + DW ·(1- $x$ )	Triton X-100	Carbowax
Amount (mg)	200	80	1120	20	30

### 8.3.5 Electrodes

The preparation of the anode was carried out in different steps: applying the TiO<sub>2</sub> slurry by spin coating or doctor blading onto the FTO glass (substrate), drying and annealing of the resulting TiO<sub>2</sub> film and finally staining of the TiO<sub>2</sub> films with the chosen dye. In the following these different steps are declared in more detail. In order to plan experiments and achieve reproducible results the entire process for preparing the anode electrodes was carried out following a protocol, specifying the work in both method and time, this protocol is presented in Table 13 on page 68 at the end of this section.

As substrate for the TiO<sub>2</sub> films in the electrodes, Fluorine doped Tin Oxide (FTO) coated glass from Solaronix was used. On the cathode side of the cell, Platinum coated FTO coated glass, TCO 22-7 with final surface resistance  $7 \Omega/\square^1$  was used. On the anode side FTO coated glass, TCO 22-15 with surface resistance  $15 \Omega/\square$  was used to prepare with TiO<sub>2</sub> film to make the electrode. All substrates were thoroughly wiped clean with isopropanol before use. The TCO 22-15 was chosen for the anode because it is more transparent to visible light than the TCO 22-7.

<sup>1</sup> The unit of surface resistance is ohm per square ( $\Omega/\square$ )

### Applying the TiO<sub>2</sub> slurry to the substrate

The three most common methods to apply a TiO<sub>2</sub> slurry to a substrate material are; the doctor blade method, the spin-coating and the screen printing method [42]. In this work the doctor blade method and the spin-coating method were used. The doctor blade method was tried with two different tools for spreading the slurry, a microscope glass (edged tool) and a glass rod (rounded tool) of 6 mm diameter. The spin coating was tried with several different combinations of rpm and spinning time in 1, 2 or 3 steps. As a starting point, a TiO<sub>2</sub> slurry composition, well tested for building DSSCs was used [27]; the composition of this slurry is declared in Table 10.

**Table 10:** Composition of the standard TiO<sub>2</sub> slurry used in [27], all amounts are recalculated to mass in units mg in this table.

Substance	TiO <sub>2</sub> P25	HNO <sub>3</sub> 0.1 M	Ethanol	Triton X-100	Carbowax
Weight (mg)	200	150	1600	20	30

The doctor blade method was first tried to apply the slurry to the substrate; this however produced rather thick and opaque TiO<sub>2</sub> films, not suitable for VIS spectrophotometry.

To get thin and homogeneous films, different compositions of the TiO<sub>2</sub> slurry were tried, this was done in combination with both doctor blade method and spin coating using different programs. Ethanol, Isopropanol and water in varied amounts were used as solvents for these slurries. Table 11 on the next page shows what compositions of slurries and applying methods were used to find a good and reproducible result. In Table 12 on the facing page the different spin coating programs are declared. The best result was achieved for sample 10. This sample is a water based slurry with mass ratio of water and TiO<sub>2</sub> of 1200/200 and it was spin coated with program 95.

**Table 11:** Different combinations of slurry compositions and applying methods used for optimizing the TiO<sub>2</sub> film considering thickness and homogeneity. The doctor blade technique was used with either a microscope slide or a glass rod to apply the slurry.

Slurry/sample	1	2	3	4	5	6	7	8	9	10	11	12
TiO <sub>2</sub> (mg)	200	200	200	200	200	200	200	200	200	200	200	200
HNO <sub>3</sub> 0.1 M (mg)	150	150	150	150	150	150	150	150	150	150	150	150
CH <sub>3</sub> CH <sub>2</sub> OH (mg)	800	1600	800	1200								
CH <sub>3</sub> CH <sub>2</sub> OHCH <sub>3</sub> (mg)					800	1600	3200					
Deionized water (mg)								400	800	1200	1600	3200
Triton X-100(mg)	20	20	60	60	20	20	20	20	20	20	20	20
Carbowax (mg)	30	30	30	30	30	30	30	30	30	30	30	30
Spin coating pgm	99	99	99	99	99	99	98	97	97	96	96	94
	98	98	98	98	98	97	97	96	95	95	95	95
	97		97	97	96	96	96	95				
Doctor blade technique	slide											
slide/rod			rod	rod	rod	rod	rod	rod				

**Table 12:** The different spin coating programs used to optimize the TiO<sub>2</sub> films

Program	99	98	97	96	95	94
Step 1: rpm/(time (s))	1100/5	1100/5	1100/5	875/20	1100/5	2150/5
Step 2: rpm/(time (s))	3930/10	3930/10	2540/10	2540/10	2540/20	3930/10
Step 3: rpm/(time (s))	-	5300/10	5300/10	-	-	-

### Annealing of the TiO<sub>2</sub> films

After spin coating, the TiO<sub>2</sub> films were dried at 125 °C for 30 minutes immediately followed by annealing at 470 °C for 30 min. During the annealing process the organic part of the film is evaporated or calcinated, bringing a porous morphology to the layer. To avoid cracks in the TiO<sub>2</sub> films during the annealing, the heating and cooling processes were carried out slowly. To achieve a slow raising of the temperature the furnace settings were adjusted manually in steps according to a schedule shown in appendix A. After the slow temperature raise the electrodes were kept in 470 °C for 30 min, after that the furnace was turned off and the samples were left in the oven for slowly cooling over night with the furnace door closed. This procedure produced annealed TiO<sub>2</sub> film without visible cracks.

### Staining the TiO<sub>2</sub> films

To stain the TiO<sub>2</sub> films with dye, the electrodes were heated to 70 °C before they were submerged into a dye solution, this was done to dry off possible moisture and to facilitate the absorption of the dye. For the staining process, sealed beakers were used. The electrodes were kept in the dye solution for 20 h at room temperature. After the staining, the electrodes were thoroughly rinsed with ethanol.

**Table 13:** Protocol for preparation of anode electrodes showing the order and the time for each step. The mixing, stirring and staining were carried out at room temperature ( $\sim 20\text{ }^{\circ}\text{C}$ )

	Activity	Time
1	Mix $\text{TiO}_2$ , $\text{HNO}_3$ and DW	
2	Stir	1 h
3	Add Triton and Carbowax	
4	Stir	2 h
5	Add gold colloid	
6	Stir	2 h
7	Grinding with mortar	30 min
9	Sonication	30 min
10	Spin coating	5 min
12	Drying at $125\text{ }^{\circ}\text{C}$	30 min
13	Annealing at $470\text{ }^{\circ}\text{C}$	$1.5\text{ h}^1$
14	Cooling over night - closed oven door	14 h
15	Staining with dye	20 h

### 8.3.6 Assembling of the cell

The assembling of the dye sensitized solar cells used in this work was made by mounting four parts together; the anode electrode with the  $\text{TiO}_2$  film, the electrolyte, the spacers and the cathode electrode; Figure 32 shows schematically how these parts were assembled to build up a dye sensitized solar cell.

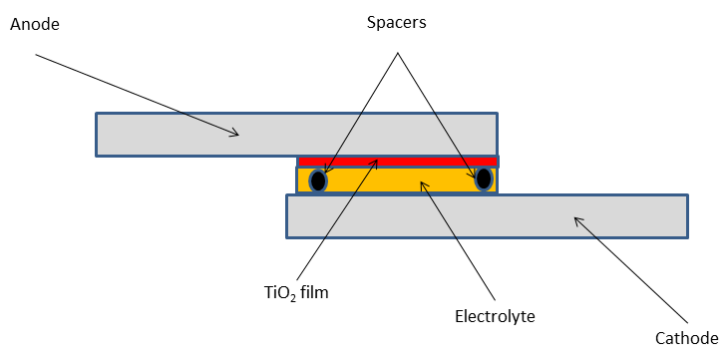


**Figure 32:** Schematic figure of a cross section of an assembled cell: showing the constituent components of a dye sensitized solar cell of the type used in this work.

<sup>1</sup> 1.5 h is the total time for raising the temperature in the furnace and keeping it at  $470\text{ }^{\circ}\text{C}$  for 30 min

The assembling was made on a fixture and the different parts of the cell was held together with two clamps, no sealing was needed for the electrolyte since it was in a gel state. Before mounting the different parts together the electrolyte was formed to a film of about 0.4 mm thickness. The electrolyte films were shaped by placing a bit of gel electrolyte between two glass plates along with two spacers made from nylon line of diameter 0.4 mm. By gently heating the glass plates and at the same time pressing them together, a thin film of electrolyte was formed. A photo of the arrangement for forming the gel film is shown in Figure 33. After cooling, the glass plates were slowly separated and the electrolyte film could be removed, cut into appropriate pieces and used in the cells.

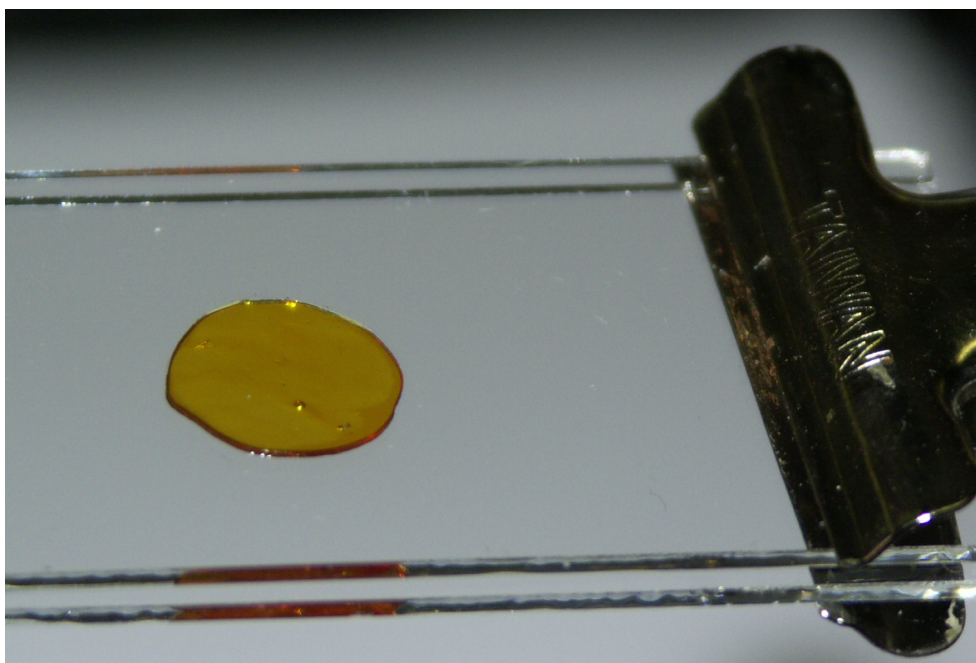
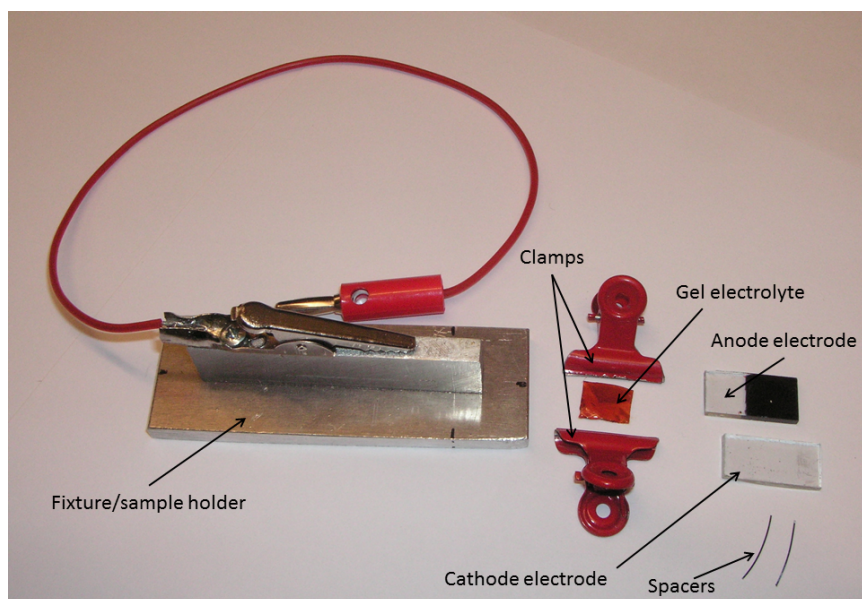


**Figure 33:** Thin electrolyte film of desired thickness was formed by pressing the gel electrolyte gently between two heated glass plates. Spacers were used to ensure the thickness of the film (not shown) and clamps to press the plates together.

A fixture as depicted in Figure 34 on the next page was used both as a tool for easy cell assemblage and as a cell holder in the set-up for irradiating the cell during I-V measurements.



(a)



(b)

**Figure 34:** (a) Photograph of the different cell components: anode, electrolyte, spacers and cathode together with the holding clamps and the fixture. (b) Photograph of an assembled cell, the black part with a hole, on top of the cell is the mask that were used for irradiating the cell with a known beam diameter. The aperture of the mask was circular with a diameter of 3.3 mm

## 8.4 Characterization of the cells

Characterization of assembled cells was carried out by measuring current and voltage on performing cells. The cells were irradiated with light of different intensity, this was achieved by filtering of the solar simulator light. For the filtering, metal plated, flat response filters with transmission  $T$  in the range from  $T=11\%$  to  $T=79\%$  were used. The filters, manufactured by GRIOT MELLEES, have a uniform absorbance in the visible light spectra.

The I-V measurement was done by using the potentiostat equipment to vary the potential between open circuit voltage and 0 V while simultaneously measuring the current through the cell, the set-up for this is schematically depicted in Figure 23 on page 56.

In Figure 35 a typical plot of current and power vs voltage for a solar cell is shown with some of the most used performing cell parameters marked.

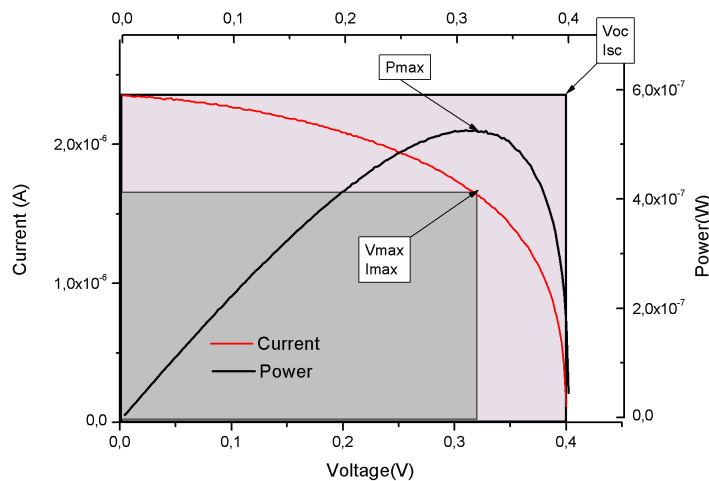


**Figure 35:** Typical graph showing the graphic result of an I-V measurement with current and power versus voltage. Characteristic values used for calculating the efficiency and fill factor are marked in the graph

It was observed that the cells degraded quite rapidly after they were assembled. Decreased cell performance were noticed already after one day, because of this observation, the characterizing measurements were always performed within 30 min after the cell assemblage.

All data for this work were extracted and calculated from the I-V measurements, using a MATLAB program.

## 8.5 Gold nanoparticle experiments

The experimental work of the gold nano particle study was divided into two main series of experiments, series 1 and series 2. Table 14 and Table 15 show which cells that belong to the two series. In these tables every cell is assigned with a unique index number, these numbers are just used to identify and keep track of the different samples and have no connection to the composition of the cells.

The first series was made to study what dye should be used to produce cells with highest sensitivity to variations in Au RSA. Here the sensitivity was considered as increase in efficiency due to variations in added amount of 10 nm GNPs in the cell. The second series was made to study correlations between cell performance, GNP size and GNP concentration (Au RSA), using the chosen dye from series 1. In series 2, GNPs of size 5, 10 and 40 nm were used. To achieve comparable result from the both series, all preparation of materials followed the same protocols and the electrolyte was taken from the same batch for all cells in these series. Same type of electrode substrates, spacers, equipment for preparation and cell assembling tools were used for all cells.

All characterizations of the cells were carried out with I-V measurements, performed at four different light intensities. From these measurements data as; efficiency,  $V_{sc}$ ,  $I_{sc}$  and fill factor were obtained. From the preliminary study of the capacitive effect in solar cells described in Appendix C, it was observed that at a rate of 50 mV/s these effects were not affecting the result considerably, therefore all the I-V measurements in series one and two were carried out at this rate.

### Calculating amounts of gold colloid

In this section it is described how the amount of gold colloid in relation to  $\text{TiO}_2$  was calculated, this was done considering the results from trying out the best slurry composition as described in section 8.3.4. It is also described which combinations of materials were used in the two main series of experiments with DSSCs containing GNPs. To clarify the outline of the work and the division between the two series, a flow chart of the work is shown in Figure 36 on the following page.

The gold colloids used in this work consisted of GNPs dispersed in purified water, this means that adding GNPs also will add water to the slurry composition. In table 4 on page 59, concentration data of the gold colloids are shown as declared from the manufacturer, BBI solutions. It was decided that the 10 nm GNPs were to be used first, therefore the calculation of the gold colloid amounts were based on the data of the 10 nm GNPs. The final slurry composition sets the relative amounts of  $\text{TiO}_2$  and water as 200/1200 in mass ratio. The density of the gold colloids can be set to  $1 \text{ g/cm}^3$  when the amounts of gold colloid for the  $\text{TiO}_2$  slurries are calculated.

As reference between cells with different amount of gold added, it was decided to use the gold relative surface area (Au RSA), which means the total surface area of the GNPs in relation to mass of  $\text{TiO}_2$  in the anode. Therefore the cells are always compared as to what Au RSA they have, the Au RSA can be thought of as concentration of gold in the photoactive layers of the cells. The Au RSA is given in units  $\text{cm}^2/\text{g}_{\text{TiO}_2}$  and means the total gold nano particle surface area per gram of  $\text{TiO}_2$ .

Using density =  $1 \text{ g/ml}$  for the 10 nm gold colloid and assuming that the gold colloids can be regarded as water when mixing of the slurry is considered, sets the maximum amount of 10 nm gold colloid to 1200 mg in the standard composition. A simple calculation shows that using an amount of 1200 mg 10 nm gold colloid will produce an Au particle area of  $21.48 \text{ cm}^2$ , see Table 4 on page 59. This means an Au RSA of  $107.4 \text{ cm}^2/\text{g}_{\text{TiO}_2}$  in a slurry containing 200 mg  $\text{TiO}_2$ . To get the more convenient number 100 for the full amount of Au RSA the amount of 10 nm gold colloid was altered to 1120 mg colloid per 200 mg  $\text{TiO}_2$  instead. For the following calculations of gold colloid amounts, the Au RSA was always used as reference between samples with different GNP size, and the total amount of gold colloid plus water is limited to 1120 mg in samples containing 200 mg  $\text{TiO}_2$ .

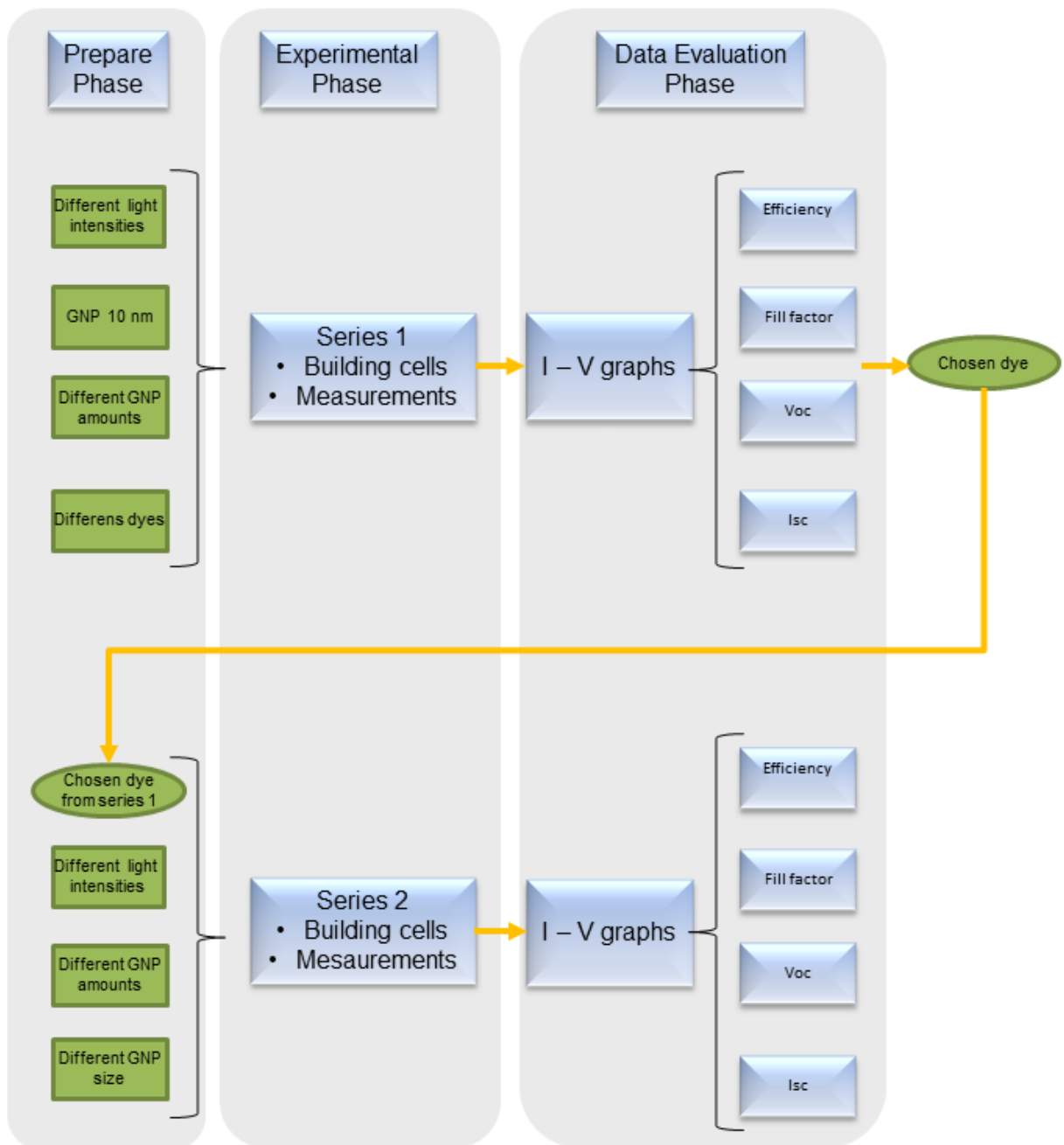


**Figure 36:** Outline of the main experiments. The figure shows the division between the two series and what in and out data that were used in the two cases.

The results from the characterizations are presented with graphs in Section 9.

### 8.5.1 Series 1 experiments

For this series of experiments, 10 nm GNPs were used in all cells and varied parameters were type of dye and Au RSA. Table 14 shows the 16 different combinations of cell parameters used in this series. The cells are identified by their index in column 1. Characterizing measurements were carried out with four different light intensities; 100, 79, 55 and 11 % of full solar simulator light intensity.

**Table 14:** The combination of dyes and Au RSA used for the cells in series 1.

Cell index	GNP size [nm]	Dye	Au RSA [ $\text{cm}^2/\text{g}_{\text{TiO}_2}$ ]
1	10	455-PF6	0
2			25
3			50
4			100
5	10	620-1H3TBA	0
6			25
7			50
8			100
9	10	SQ2	0
10			25
11			50
12			100
13	10	no dye	0
14			25
15			50
16			100

### 8.5.2 Series 2 experiments

Based on the results of series 1 the Ruthenizer 455-PF6 dye was chosen to be used for all the cells in series 2. The parameters to be varied for the cells in series 2 were; GNP size and Au RSA. Table 15 shows all the combinations of these parameters used for the cells in series 2. The cells are identified by their index in column 1. The characterizing measurements were done with four different light intensities in the same way as for series 1.

**Table 15:** The combination of dyes and Au RSA used for the cells in series 2.

Cell index	GNP size [nm]	Dye	Au RSA [ $\text{cm}^2/\text{g}_{\text{TiO}_2}$ ]
17	5	455-PF6	0
18			12
19			25
20			38
21			50
22			75
23			100
24			125
25	10	455-PF6	0
26			12
27			25
28			38
29			50
30			75
31			100
32	40	455-PF6	0
33			6
34			12
35			18
36			24

**Part IV**  
**RESULTS**



## 9 Results and discussion

In this section the results from; absorption measurements, TiO<sub>2</sub> slurry study, impedance measurements of the electrolyte and the characterizing of the solar cells are presented. In both figures and texts, the following abbreviations are used to save space.

- 455 = Ruthenizer 455-PF6 dye.
- SQ2 = Sensidizer SQ2 dye.
- 620 = Ruthenizer 620-1H3TBA dye.
- Tx = Filter transmittance, where x is transmittance in percent. I.e. T100 means 100% transmisssion of light which is the same as the unfiltered light source and T11 means 11% of the light is transmitted.
- gx = amount of gold where x is the value of the Au RSA in units cm<sup>2</sup>/g<sub>TiO<sub>2</sub></sub>.

### 9.1 Absorption measurements

All absorption measurements of dyes and gold colloids were carried out on a Perkin Elmer Lambda 900 UV/VIS/NIR spectrometer. Absorbance were measured in the wavelength range 300 - 900 nm. As sample holders, quartz cuvettes with path length of 1 mm were used for the gold colloid samples and 10 mm for the dye solution samples. The gold colloid samples were measured undiluted while the dye samples were diluted to 0.015 mM. The settings for the spectrometer were the same in all measurements for both dyes and gold colloids, these are presented in Table 16.

**Table 16:** Instrument setting for the absorption measurements.

Instrument	Perkin Elmer Lambda UV/VIS/NIR 900
Wavelength range	300 - 900 [nm]
Step size	1 [nm]
Slit size	5 [nm]
Integration time	0.08 [s]
Scan speed	500 [nm/min]

### 9.1.1 Absorption spectra of dyes

The graphs from the absorption measurements of the dyes; 455-PF6, 620-1H3TBA and SQ2 are presented in Figure 37.

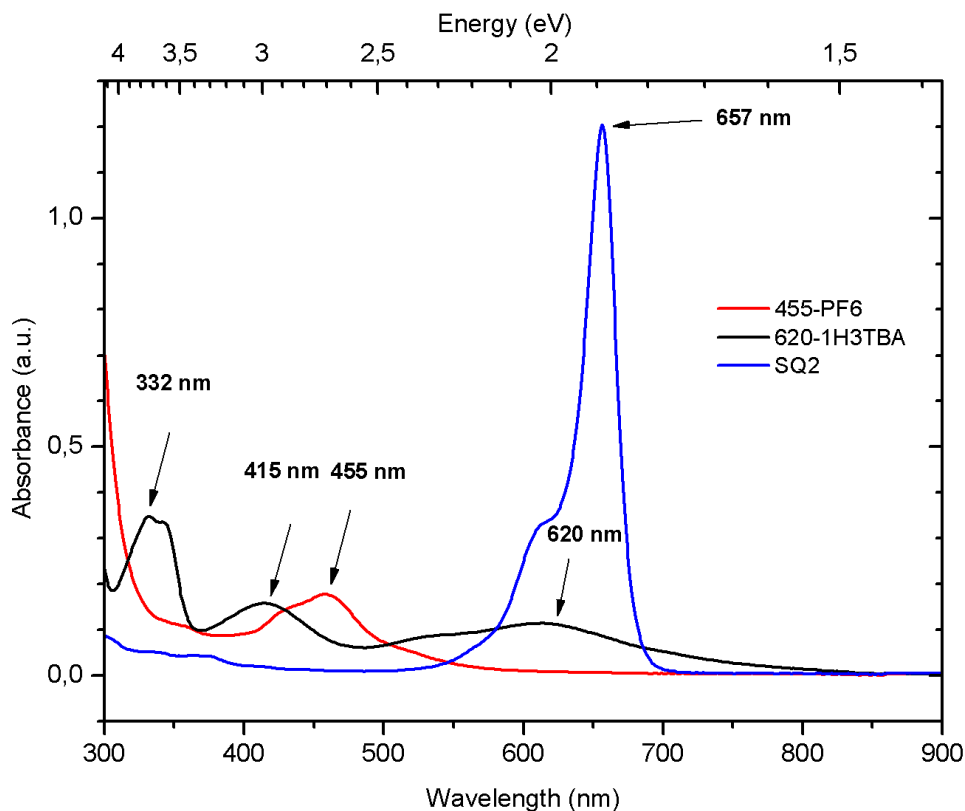


**Figure 37:** Absorption spectra of dyes; 455-PF6, 620-1H3TBA and SQ2. Concentration: 0.015 nM in ethanol. Ethanol was used for reference to compensate for background signals. 10 mm quartz cuvettes were used as sample holders.

The graphs in Figure 37 show that the three dyes have quite different absorption spectra. The SQ2 dye has one high and narrow peak at 657 nm while the 455 and 620 have more spread out absorption spectra. In the region below 500 nm the 455 and 620 dyes absorb more than the SQ2 dye. The measured spectrum of the SQ2 is in good agreement with results found in [55].

### 9.1.2 Absorption spectra of gold colloids

Metal nanoparticles can absorb light when the frequency of the irradiated light match the plasmonic resonance frequency of the nanoparticles. The plasmonic resonance frequency is dependent of the nanoparticle size and shape, see Section 6. In this work gold nano particles of size: 2, 5, 10 and 40 nm diameter were initially chosen. Water based colloids containing these GNPs were characterized with absorption measurements. The resulting spectra are shown in Figure 38.

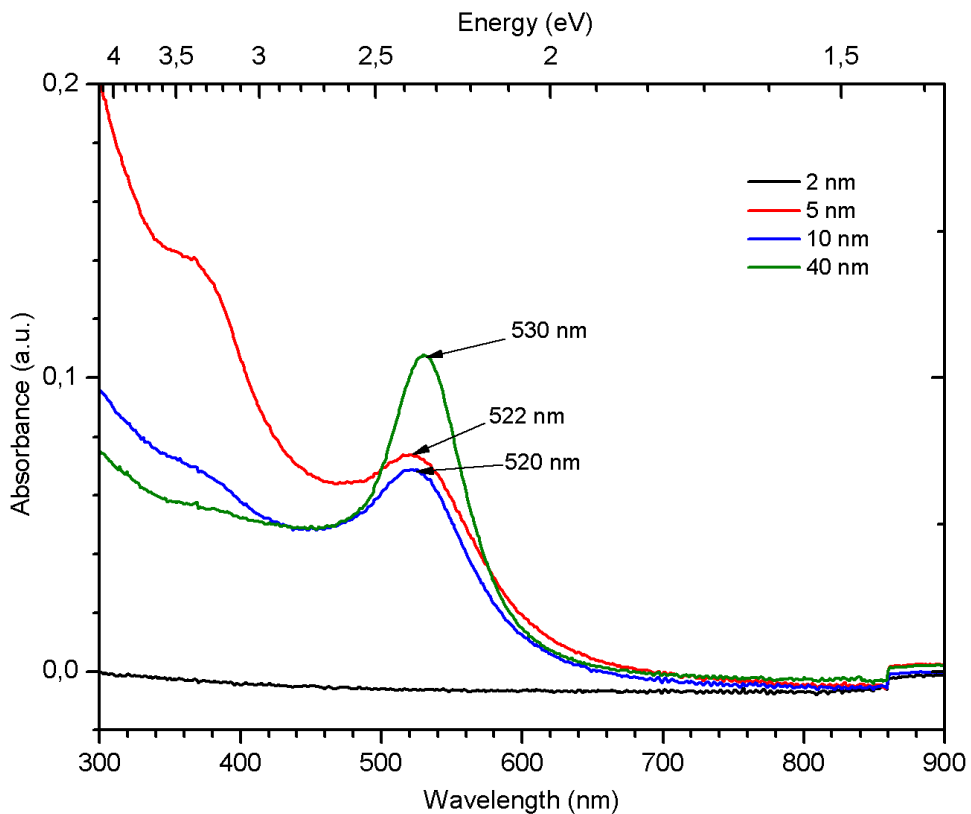


**Figure 38:** Absorptionspectra of the gold colloids containing GNPs of size 2, 5, 10 and 40 nm. Deionized water was used for reference to compensate for background signals. As sample holders, 1 mm quartz cuvettes were used.

Colloids containing GNPs of size 5, 10 and 40 nm have their absorption peaks quite close to each other, centred around 525 nm. The 40 nm sample has the most distinct and also the highest peak. The 5 nm GNPs show the most broad absorption spectra and they absorb more than the others for wavelengths below 500 nm, i.e. they absorb more of the high energy wavelengths of the light. The 2 nm gold colloid did not show any absorption in the measured wavelength interval, therefore the 2 nm GNPs were excluded from the actual experiments with cells containing GNPs.

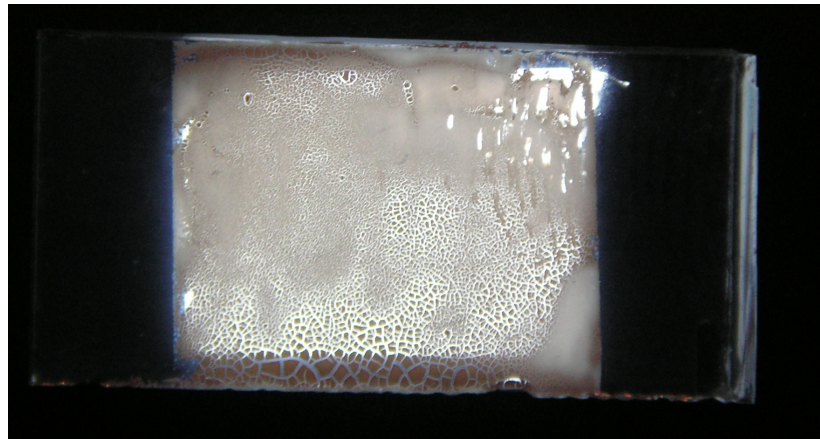
## 9.2 TiO<sub>2</sub> slurry composition

As mentioned earlier, the aim was to study effects on the cell performance of GNPs dispersed in the anode. To best clarify these effects, thin TiO<sub>2</sub> films (0.7 - 0.8 nμm) were used. Typical thickness of TiO<sub>2</sub> films used in DSSCs is about 10 μm but in this work even thinner films were desired [15, 56]. One way to evaluate the effects on the optical absorption of added GNPs is to study the absorption spectra of the resulting TiO<sub>2</sub> films. To have this option the TiO<sub>2</sub> films need to be thin enough to be somewhat transparent to UV/VIS/NIR light. The absorption spectra of the final TiO<sub>2</sub> films were not measured in this work.

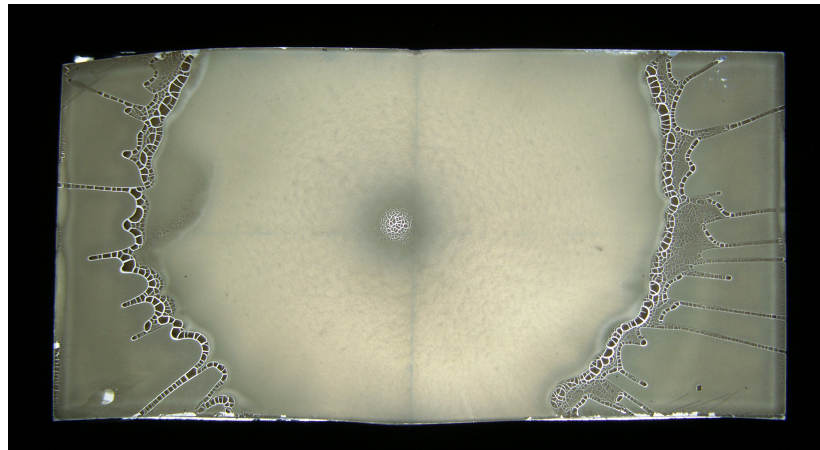
Different compositions of TiO<sub>2</sub> slurry and applying methods as declared in Table 11 on page 67 were tested to achieve thin and homogeneous TiO<sub>2</sub> films. The result of these tests is listed in 1 - 5 below:

1. The doctor blade method did not work well for any of the tested samples, either the resulting films were inhomogeneous or they were too thick and opaque to be used in absorption measurements.
2. For all slurries containing ethanol, i.e samples 1 - 4, there were problems with the fast evaporation of the solvent, this caused cracks in the film in most of the tried cases. For these samples the resulting films were also inhomogeneous. In sample 3 and 4 three times more Triton were added to facilitate the spreading of the slurry but the produced films were still not homogeneous.
3. In sample 5 - 7, isopropanol was used as solvent, these compositions produced films without cracks but the issue with inhomogeneous films remained. Sample 6 and 7 were too dilute, basically no material stayed on the substrate during the spin coating and the doctor blade method did not work well either.
4. In sample 8 - 12 deionized water was used as solvent instead and for these compositions the spin coating produced more homogeneous films. Sample 8 and 9 produced a bit too opaque films considering possibilities of absorption measurements and samples 11 and 12 were too dilute to produce good films. Sample 10 was regarded as the best option among these for producing the desired, thin and homogeneous TiO<sub>2</sub> films.

Figure 39 on the facing page shows two examples of poor TiO<sub>2</sub> films made in this study. The two main issues, inhomogeneous film and formation of cracks are clearly seen in both examples. The samples are not annealed so the observed cracks were formed after the spin coating process, during the evaporation of the solvents.



(a)



(b)

**Figure 39:** Photographs showing examples of poor results of applied TiO<sub>2</sub>. These films were made from slurries containing ethanol. The samples are not annealed. (a) sample 2 applied with the doctor blade method using a glass rod. (b) sample 3 applied with spin coating process of 1100 rpm for 5 s + 3930 rpm for 10 s + 5300 rpm for 10 s (spin coater program 98).

The best result for applying the slurry to the glass substrate was achieved using a water based composition with a mass ratio of water and TiO<sub>2</sub> of 1200/200 applied with spin coating program 95, see Table 11 on page 67. The thickness of these TiO<sub>2</sub> films was 0.7 - 0.8  $\mu\text{m}$ . Based on observations in this study, the composition of sample 10 was chosen as the standard slurry to be used as an starting point when the composition of slurries including GNPs should be decided.

In some cases there were remaining particles or lumps in the TiO<sub>2</sub> film after the spin coating, these particles were large enough to identify with visual inspection, see Figure 40 on the following page. By trying different combinations of grinding and sonicating of the slurries, it was found that these inhomogeneities could be eliminated by grinding TiO<sub>2</sub> slurry with a mortar for 30 min. and then sonicate it for 30 min. prior to the spin coating process.

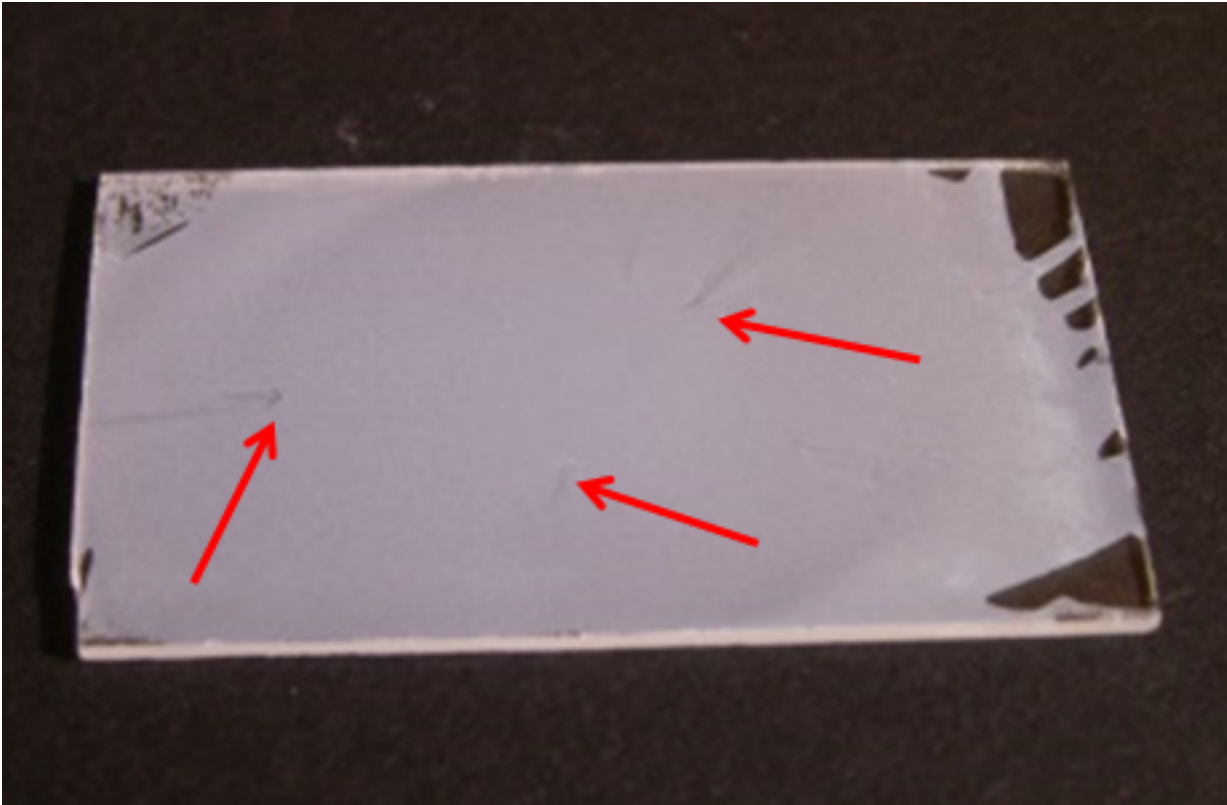


**Figure 40:** Photograph of an electrode, spin coated with a slurry composition according to Table 9 on page 65 with  $x=0.25$ . The slurry was sonicated for 30 min. but not worked on with the mortar. The spin coating was performed with program 95 and the electrode was annealed at 470 °C for 30 min. The photograph clearly shows residual large particles in the final TiO<sub>2</sub> film.

### 9.3 Impedance measurements of the electrolyte

The conductivity of the electrolyte is of great importance because it is a property that might limit the photocurrent in the cell [45]. The conductivity can be calculated from impedance measurements. The impedance of the Hex120 electrolyte, composed according to Table 8 on page 64, was measured with the HP 4192A LF impedance analyser in a frequency range from 5 Hz to 13 MHz and temperature range of 0 - 60 °C. The Nyquist plot of the measurements is shown in Figure 41.

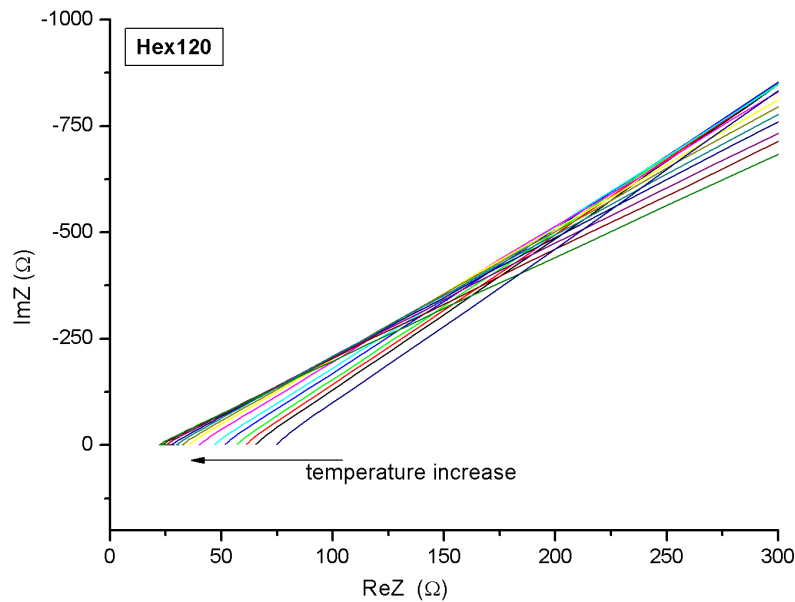


**Figure 41:** Nyquist plot of the impedance measurements for Hex120 electrolyte in the temperature range 0 - 60 °C with 5 °C separation between each measurement.

The conductivity is calculated from the measured results as [57]:

$$\sigma = \frac{l}{R \cdot A} \quad (30)$$

where  $l$  = length of sample (0.071 cm) and  $A$  = cross section area of the sample (0.8642 cm<sup>2</sup>). The resistance  $R$  is read from the graphs where the imaginary part of the impedance has its minimum, the plot shows decreasing resistance with increasing temperature for this electrolyte. The resistance and the calculated conductivity of the sample are presented in Table 17 and Figure 42 on the next page.

**Table 17:** Measured resistance and calculated conductivity in the temperature interval 0 - 60 °C for the Hex120 electrolyte.

Temperature [°C]	Resistance [ $\Omega$ ]	Conductivity [mS/cm]
0	74.78	1.10
5	61.15	1.34
10	51.64	1.59
15	47.06	1.74
20	50.97	1.61
25	43.89	1.87
30	40.04	2.05
35	35.50	2.31
40	32.07	2.56
45	28.75	2.89
50	26.67	3.08
55	24.28	3.38
60	22.89	3.59

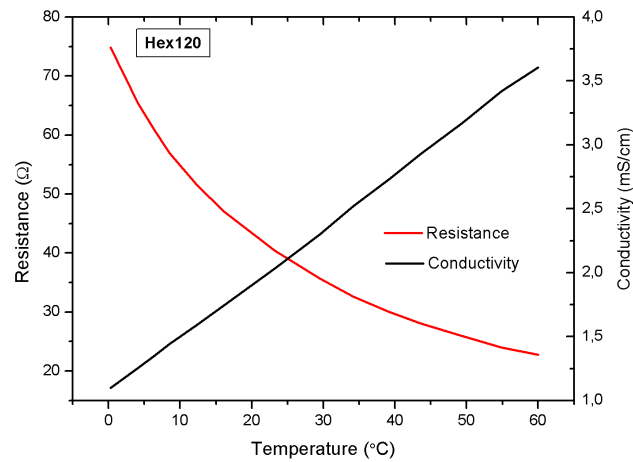


**Figure 42:** Resistance and conductivity in the temperature interval 0 - 60 °C for the hex120 electrolyte.

The conductivity increases with temperature. This behaviour can be expected since the ions in the electrolyte should be able to move more freely as the gel electrolyte becomes less rigid with increasing temperature. The calculated values for the conductivity in the temperature interval 0 - 60 °C are in the range of 1.1 to 3.59 mS/cm which is in accordance with earlier reported results [28]

## 9.4 Characterization of the cells

To observe and evaluate effects of adding GNPs into the photoactive layers of the cells, characterizations of performing cells were carried out. As described in the experimental section, all characterizations of the assembled cells were based on measuring the I-V characteristics with different intensities of irradiating light. Irradiation intensity was varied by using different filters. Data from the measurements were used for additional calculation of performing properties.

The results are presented with graphs showing how different performing properties of the cells were affected by or correlated with the varied parameters. The graphs present the properties as functions of Au RSA in the unit  $\text{cm}^2/\text{g}_{\text{TiO}_2}$ . To facilitate comparison to other units, a translation between Au RSA, Au wt % and number of GNPs is given in Table 18. The results from the characterizations of the cells are presented in an order that reflects the outline of the experiments as shown in Figure 36 on page 74.

**Table 18:** Translation between different units of GNP amounts. The table translates between; Au RSA [ $\text{cm}^2/\text{g}_{\text{TiO}_2}$ ], wt % and number of GNPs per gram of  $\text{TiO}_2$ . The wt % is here defined as mass of gold divided by mass of  $\text{TiO}_2$ , expressed in percent. The table is based on the combinations of Au RSA and GNP size that were used for the different cells.

GNP size [nm]	Quantity	Value									
5	Au RSA		12			25	38	50	75	100	125
	wt % $\cdot 10^{-3}$		1.9			4.0	6.1	8.1	12.1	16.1	20.1
	# GNPs $\cdot 10^{13}$		1.5			3.2	4.8	6.4	9.5	12.7	15.9
10	Au RSA		12			25	38	50	75	100	
	wt % $\cdot 10^{-3}$		3.9			8.1	12.2	16.1	24.1	32.2	
	# GNPs $\cdot 10^{12}$		3.8			8.0	12.1	15.9	23.9	31.8	
40	Au RSA	6	12	18	24						
	wt % $\cdot 10^{-3}$	7.7	15.5	23.2	30.9						
	# GNPs $\cdot 10^{11}$	1.2	2.4	3.6	4.8						

All cells from series 1 and 2 were characterized with varied intensities of irradiated light, this resulted in a large amount of I-V graphs and all of them are not presented here, instead a smaller collection of these is chosen to be shown. In the text and the captions of the figures, the cells are referred to with the index numbers as presented in the Table 14 on page 75 and Table 15 on page 76.

### 9.4.1 I-V graphs for cells in series 1

In series 1, cells containing 10 nm GNPs and cells with no GNPs were studied in combination with the different dyes; 455, 620 and SQ2, blank samples without dye sensitisation were also included. In Figures 43 and 44 on the next page, the characteristic I-V graphs of these experiments are presented. Efficiency, fill factor, open circuit voltage and short circuit current are presented in the captions to the figures.

#### Cells without GNPs

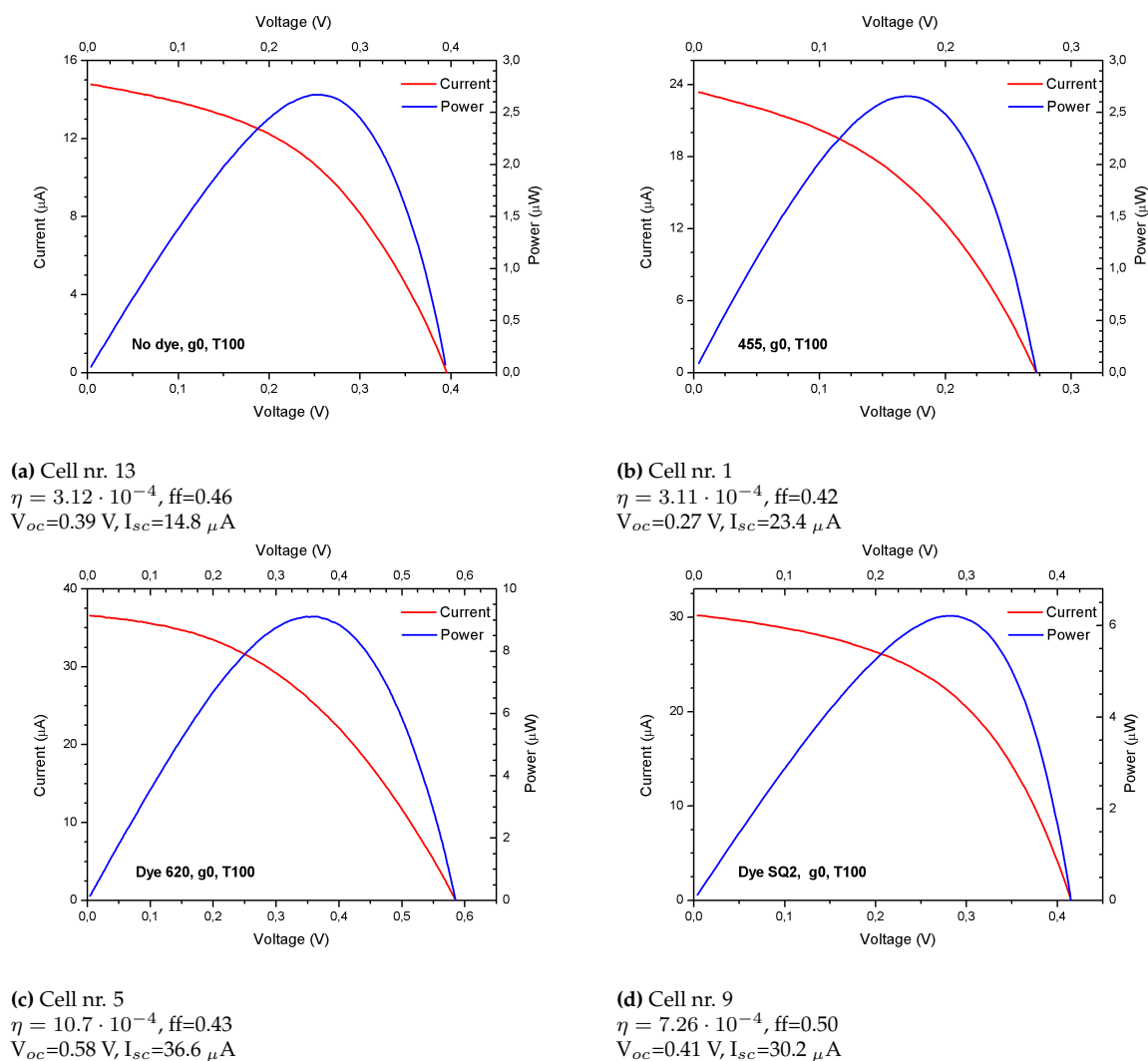


**Figure 43:** I-V graphs for solar cells with different dyes and without GNPs, irradiated with unfiltered light.

### Cells containing GNPs

To present I-V graphs for cells containing GNPs, cells with Au RSA of  $25 \text{ cm}^2/\text{g}_{\text{TiO}_2}$  were chosen because they showed the highest efficiencies in this series.

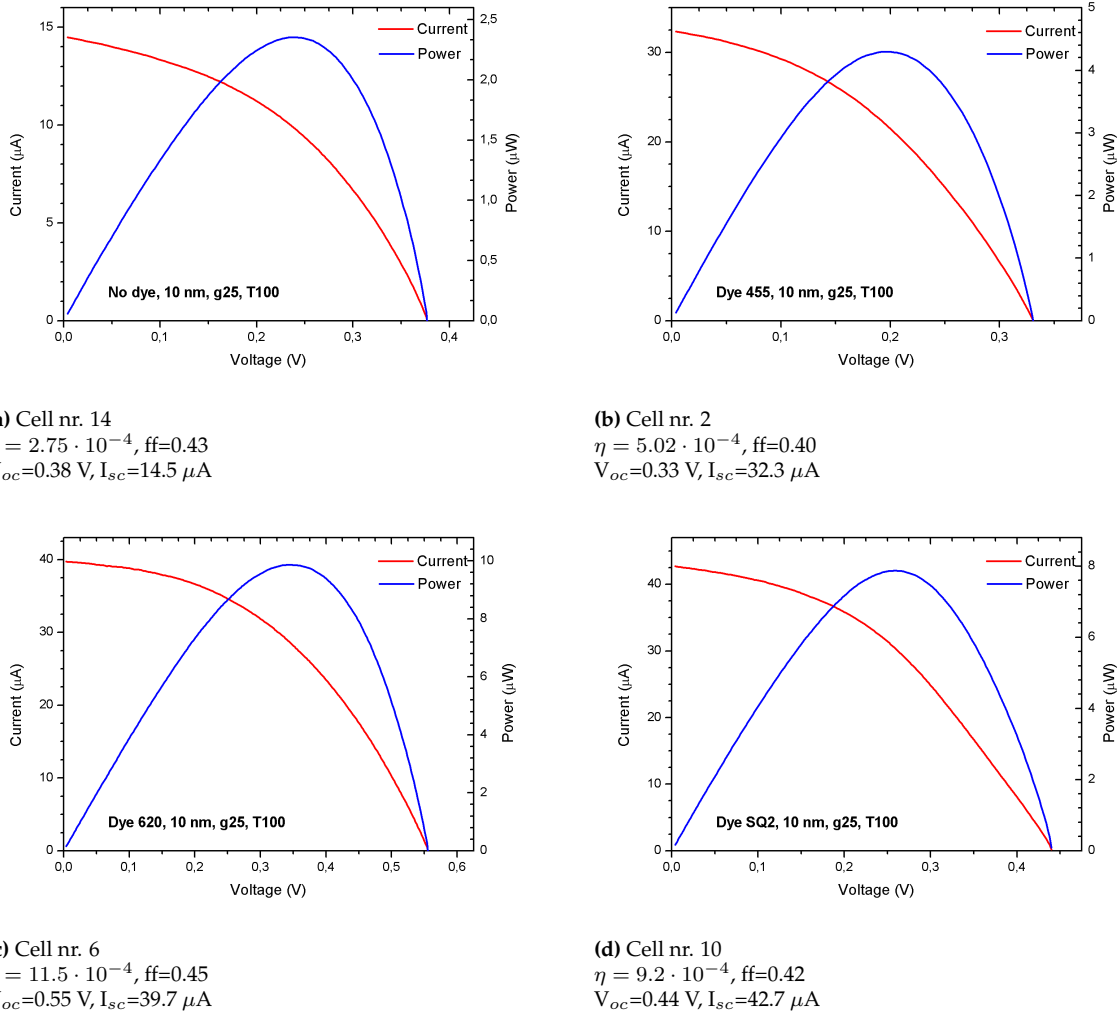


**Figure 44:** I-V graphs for solar cells with different dyes and GNP content of Au RSA =  $25 \text{ cm}^2/\text{g}_{\text{TiO}_2}$ , irradiated with unfiltered light ( $T=100$ ).

In Figure 43 on the facing page, I-V graphs from cells without GNPs are shown and in Figure 44 a-d graphs from cells containing 10 nm GNPs are shown. All these cells show quite low fill factors, between 0.42 and 0.50 for the cells without GNPs and between 0.40 and 0.45 for the cells containing GNPs. In fact, all cells in series 1 show low fill factors, the values varies between 0.39 and 0.55. If the DSSCs are considered as described by the solar cell equivalent model presented in Section 5, the low fill factor might be explained by low shunt resistance caused by electrolyte contacting the TCO

glass. Also the efficiencies for these cells are quite low, a reason for the low efficiencies can be low rate of photon to electron conversion due to the fact that the absorbing photoactive layers used in this work were quite thin ( $< 1\mu\text{m}$ ).

The thin and porous  $\text{TiO}_2$  films might be an explanation for short circuits between the conducting surface of the TCO glass and the electrolyte. Thin and porous  $\text{TiO}_2$  films might contain small channels through which electrolyte directly can contact the TCO glass. If this happens, it opens more possible routes for recombining electrons directly from the TCO glass to the dye or to transfer electrons to tri-iodide molecules in the electrolyte. These short circuit currents will lower the shunt resistance in the cell. In the article by Guliani et.al [45] it is also discussed that low shunt resistance may be caused by electron transfer from the  $\text{TiO}_2$  to the electrolyte in the interface of  $\text{TiO}_2$ , dye and electrolyte. In this work the  $\text{TiO}_2$  films containing GNPs and dye were directly contacting the TCO glass and therefore electron transfer between the TCO glass and the dye as well as the GNPs must exist also.

It might be possible though, to prevent these back currents by composing the semi-conducting part, the  $\text{TiO}_2$  layer, differently. Instead of using only one layer for attaching and electrically contacting the  $\text{TiO}_2$  film to the conducting glass as well as for absorbing the dye, as it was done here, several layers can be used instead. Doing so, the first layer can be made very thin and dense without organic components which basically is used to achieve porous layers. This thin layer will make a good contact with the TCO glass and at the same time effectively prevent the electrolyte from contacting the glass. However, thin and dense layers will not make a good absorber for the dyes. On top of this first layer, thicker porous layers can be added to get effective absorption of the dye, the result will be a cell with good absorption of dye, still able to isolate the electrolyte from the TCO glass.

#### 9.4.2 Efficiency of cells in series 1

To decide which dye from series 1 should be used to produce cells that react most positive to variations in Au RSA, normalized graphs of efficiency vs Au RSA were made. These graphs are presented in Figure 45 on the facing page. The normalization is made with respect to the value of efficiency of the sample without any GNPs (Au RSA 0 in the graphs).

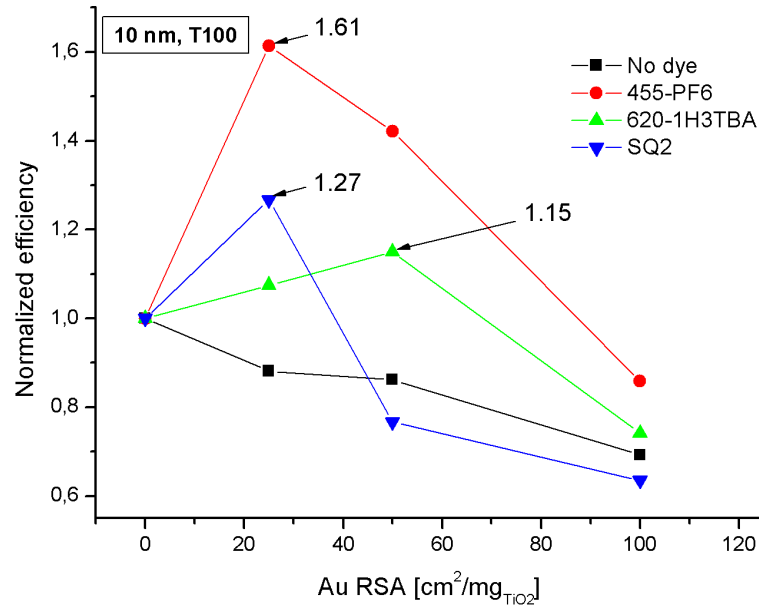


**Figure 45:** Normalized graphs of efficiency vs Au RSA for cells with different dyes, these graphs show results for cells irradiated with unfiltered light,  $T=100$ .

From the normalized graphs in Figure 45, it is clear that cells sensitized with 455-PF6 dye are the most positively reacting ones to addition of GNPs up to an Au RSA of  $25 \text{ cm}^2/\text{g}_{\text{TiO}_2}$ . For the cells without sensitizing dye the efficiency was decreased when GNPs were added. The graphs for the sensitized cells show a peak performance in efficiency, indicating that above a certain value of Au RSA further addition of GNPs will be contra productive and the efficiency will decrease. This is valid for all dye sensitized cells. The efficiency peaks occurred at different amount of Au RSA depending on which sensitizing dye was used. The maximum relative increase of efficiency for the different cells is also presented in Table 19.

**Table 19:** Max relative increase of efficiency for dye sensitized cells containing GNPs of size 10 nm.

Sensitizing dye	Rel. increase of $\eta$ [%]	Au RSA <sub>max.incr.</sub> [ $\text{cm}^2/\text{g}_{\text{TiO}_2}$ ]
455-PF6	61	25
620-1H3TBA	15	50
SQ2	27	25
No dye	neg.	-

### 9.4.3 Current at maximum power of cells in series 1

Normalized graphs of  $I_{P_{max}}$  as function of Au RSA were also made to see if the variations in efficiency and current at maximum power follow the same pattern as the Au RSA is varied. The normalization is made with respect to the value of the sample without any GNPs (Au RSA 0 in the graphs).

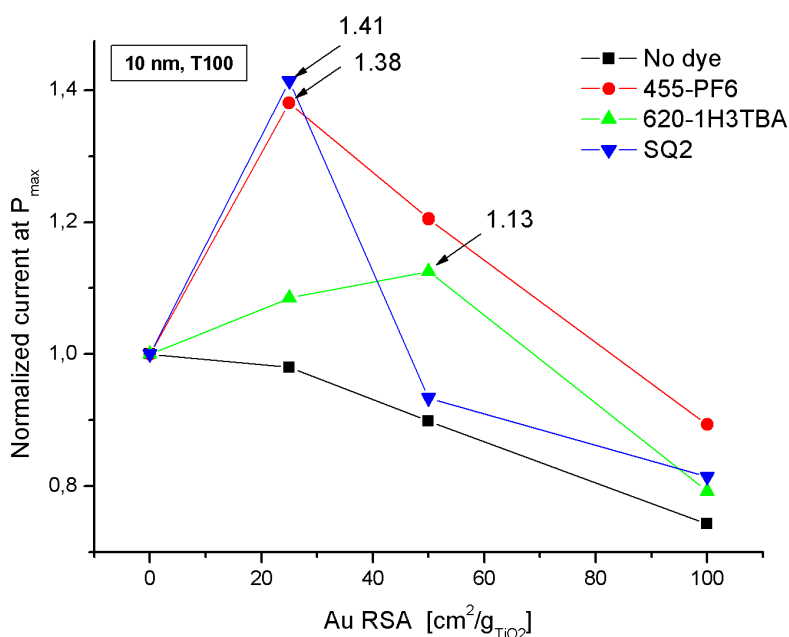


**Figure 46:** Normalized graphs of  $I_{P_{max}}$  vs Au RSA for cells with different dyes and unfiltered light,  $T=100$ .

The graphs in Figure 46 show that cells with 455-PF6 and SQ2 dye have approximately the same relative increase of  $I_{P_{max}}$  and also that this occurs at the same Au RSA,  $25 \text{ cm}^2/\text{mg}_{\text{TiO}_2}$ . As shown in Figure 45 on the preceding page and Figure 46, the relative increase in efficiency is higher for cells with sensitized with 455-PF6 dye than for those sensitized with SQ2 dye while the relative increase of  $I_{P_{max}}$  is approximately the same. For cells sensitized with 620-1H3TBA the relative increase of efficiency and  $I_{P_{max}}$  show similar dependence on variations in Au RSA. Max. relative increase of  $I_{P_{max}}$  for the different cells is also presented in Table 20 on the facing page below:

**Table 20:** Max relative increase of current at maximum power,  $I_{P_{max}}$  for dye sensitized cells containing GNPs of size 10 nm.

Sensitizing dye	Rel. increase of $I_{P_{max}}$ [%]	Au RSA <sub>max.incr.</sub> [ $\text{cm}^2/\text{g}_{\text{TiO}_2}$ ]
455-PF6	38	25
620-1H3TBA	13	50
SQ2	41	25
No dye	neg.	-

#### 9.4.4 I-V graphs for cells in series 2

Based on the results in series 1 it was decided that cells in series 2 should be sensitized with the 455-PF6 dye. In series 2, this dye was tested in combinations with GNPs of sizes 5, 10 and 40 nm. In order to get more detailed measurements, the collection of samples was also extended to contain more values of Au RSA. First a collection of I-V graphs from series 2 is presented. For each GNP size, the cell with the Au RSA that produced the highest efficiency under unfiltered irradiation was chosen for this collection. The I-V graphs for these cells are shown in Figure 47 on the next page.

## I-V graphs of cells with highest efficiency from series 2

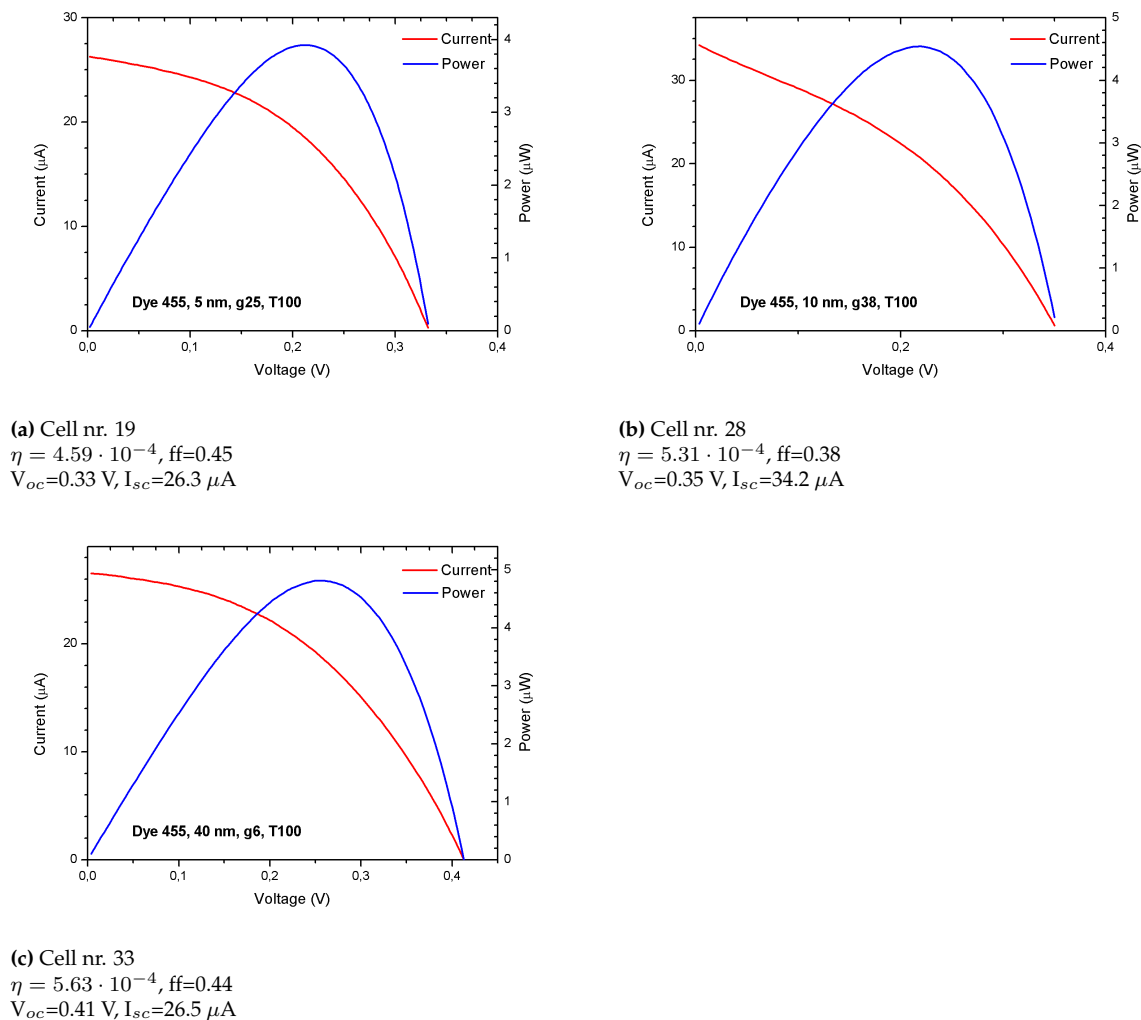


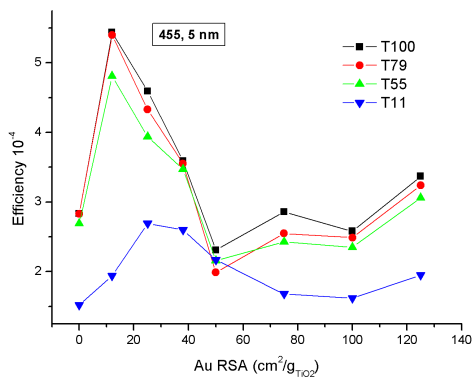
**Figure 47:** I-V graphs for solar cells containing 455-PF6 dye and GNPs of size; 5, 10 and 40 nm. Irradiation with unfiltered light.

The graphs in Figure 47 a-c and the calculated values show that these cells have quite low fill factors and efficiencies, this was the case for the cells in series 1 as well. The rather poor cell performance was observed not just for these chosen cells, it was also observed as a general result for all cells in series 2. The reasons for the poor cell performance of the cells here is believed to be the same as discussed for the cells in series 1.

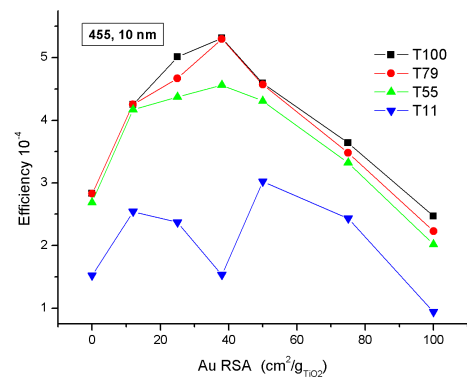
### 9.4.5 Efficiency of cells in series 2

In the following, efficiencies for cells from series 2 are presented with graphs of efficiency as function of Au RSA. The plots are divided into two groups; one group showing efficiency for different light intensities, one plot for each GNP size; the other group showing the efficiencies for the different GNP sizes, one plot for each light intensity. This system of grouping plots is also used for the presentations of fill factor, open circuit voltage, short circuit current, current at maximum power and voltage at maximum power that follows.

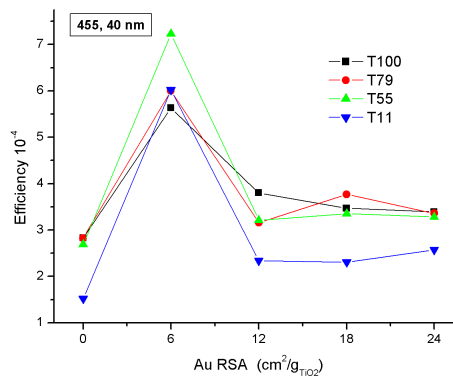
#### Efficiency at different light intensities



(a) Efficiency for cells containing 5 nm GNPs and dye 455 at different light intensities.



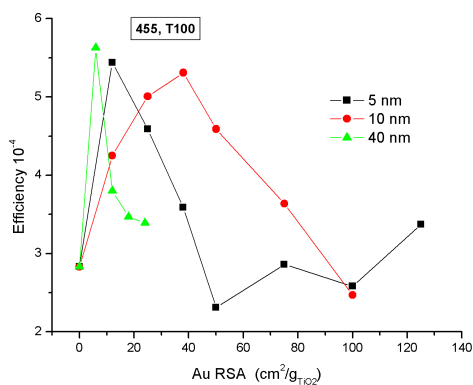
(b) Efficiency for cells containing 10 nm GNPs and dye 455 at different light intensities.



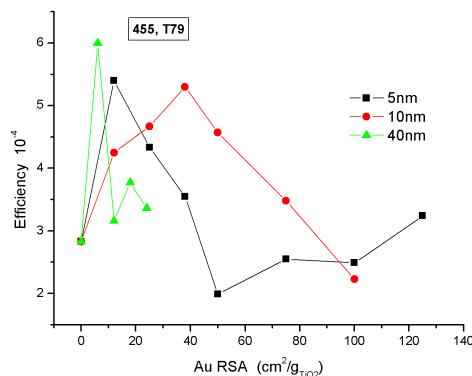
(c) Efficiency for cells containing 40 nm GNPs and dye 455 at different light intensities.

**Figure 48:** Efficiency as function of Au RSA for cells sensitized with 455-PF6, irradiated with different light intensities.

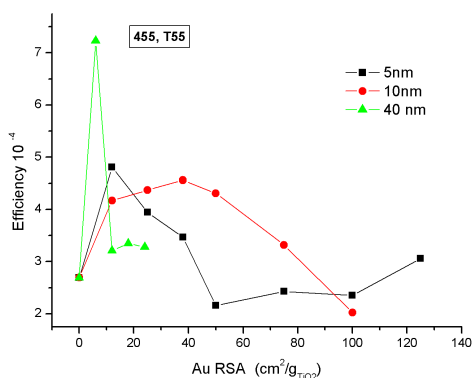
## Efficiency at different GNP size



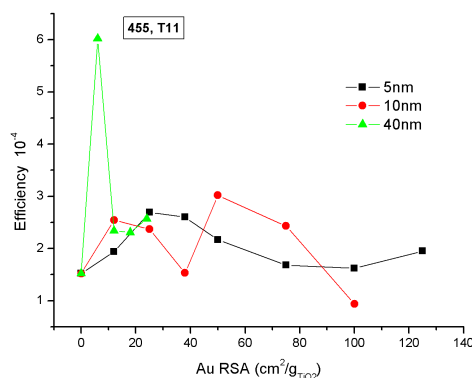
(a) Efficiency for different cells with GNP size 5, 10 or 40 nm with T100 and dye 455.



(b) Efficiency for different cells with GNP size 5, 10 or 40 nm with T79 and dye 455.



(c) Efficiency for different cells with GNP size 5, 10 or 40 nm with T55 and dye 455.



(d) Efficiency for different cells with GNP size 5, 10 or 40 nm with T11 and dye 455.

Figure 49: Efficiency as function of Au RSA for cells with dye 455-PF6 and different GNP size.

Figure 48 on the previous page and Figure 49 clearly show that efficiency has a peak behaviour when studied as function of Au RSA, this is valid for all the different light intensities used here. The graphs in Figure 48 on the previous page also show that the efficiencies reach the peak value at different Au RSA. The 5 nm cells have peaks at 12 and 25, 10 nm cells at 38 and 40 nm cells at 6  $\text{cm}^2/\text{g}_{\text{TiO}_2}$  Au RSA. The efficiency for the 10 nm cell with 38  $\text{cm}^2/\text{g}_{\text{TiO}_2}$  Au RSA, irradiated under T11 filtering seems to deviate from the general pattern, this might be due to some measurement error. The 40 nm cells reach the highest efficiency, this occurs for the T55 irradiation. Considering efficiency, the cells with 40 nm GNPs are less affected than the others by variations in light intensity. The maximum difference between max and min efficiency due to variations in light intensity is shown in Table 21 on the facing page.

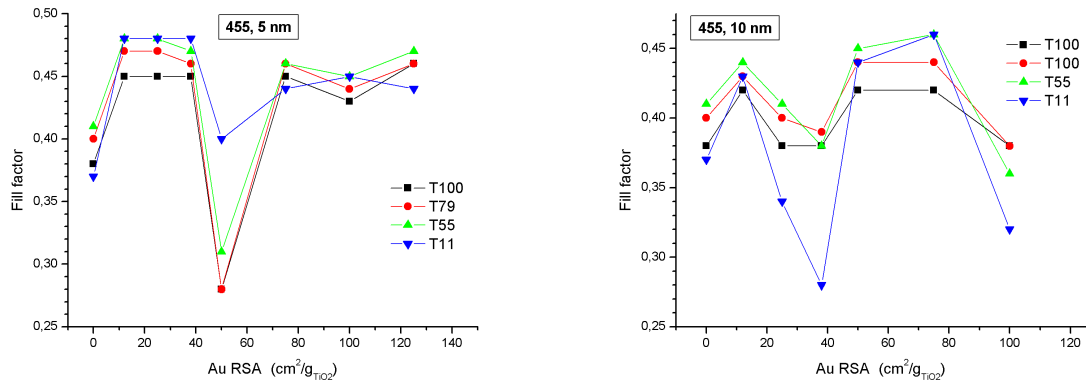
**Table 21:** Table showing max decrease in efficiency due to variations in light intensity.

<b>GNP size [nm]</b>	<b>Rel. decrease of efficiency [%]</b>
5	64
10	55
40	22

The cells with 40 nm GNPs were the least sensitive ones to variations in light intensity and also, with efficiency peaks occurring at the same Au RSA for different light intensities.

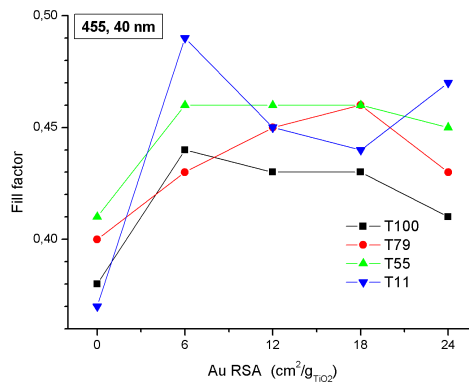
9.4.6 Fill factor of cells in series 2

Fill factor at different light intensity



(a) Fill factor for cells containing 5 nm GNPs and dye 455 at different light intensities.

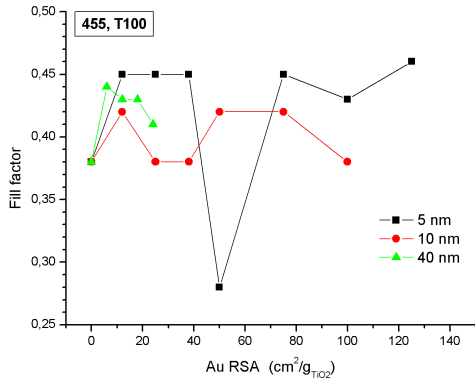
(b) Fill factor for cells containing 10 nm GNPs and dye 455 at different light intensities.



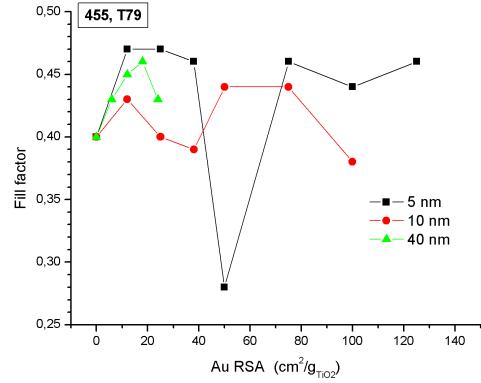
(c) Fill factor for cells containing 40 nm GNPs and dye 455 at different light intensities.

Figure 50: Fill factor as function of Au RSA for different light intensities and dye 455-PF6.

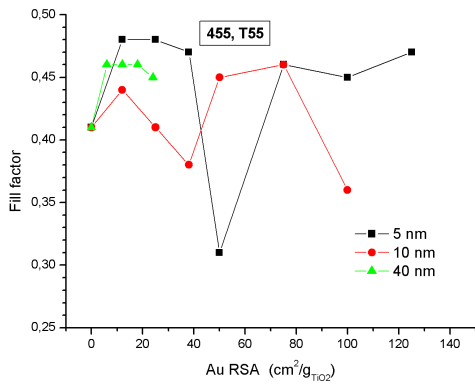
## Fill factor with different GNP size



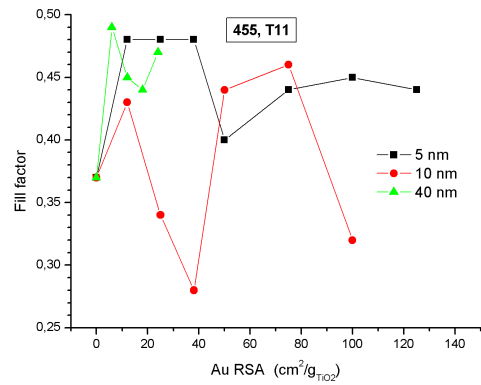
(a) Fill factor for different cells with GNP size 5, 10, or 40 nm with T100 and dye 455.



(b) Fill factor for different cells with GNP size 5, 10, or 40 nm with T79 and dye 455.



(c) Fill factor for different cells with GNP size 5, 10, or 40 nm with T55 and dye.



(d) Fill factor for different cells with GNP size 5, 10, or 40 nm with T11 and dye 455.

Figure 51: Fill factor as function of Au RSA for different GNP size and dye 455-PF6.

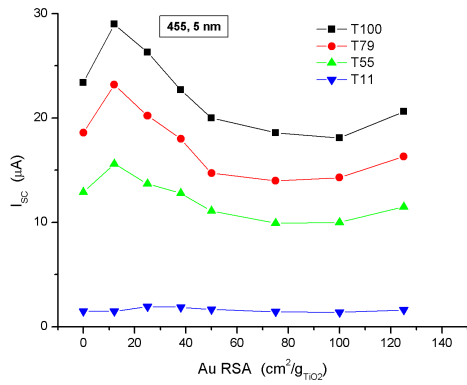
The fill factor for the 5 and 10 nm GNPs show a local minima at 50 and 38  $\text{cm}^2/\text{g}_{\text{TiO}_2}$  Au RSA respectively. The 40 nm cells show a maximum at 6  $\text{cm}^2/\text{g}_{\text{TiO}_2}$  Au RSA. In general the values of the fill factor were quite low.

### 9.4.7 Short circuit current of cells in series 2

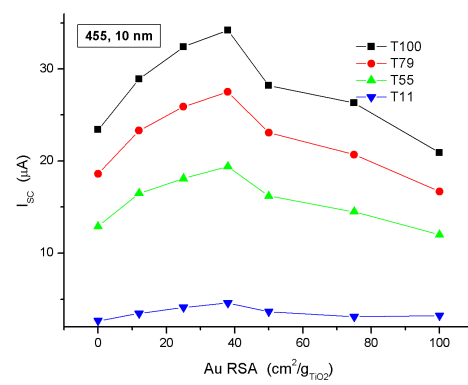
In the preceding section, the efficiency and fill factor were studied in different graphs. With the aim to study the effects of added GNPs on cell performance, it can be a bit misleading to study the efficiency alone, being a product of voltage and current. The produced current itself is also of great interest as it reflects the efficiency of the photon to electron conversion more directly than the overall cell efficiency. A significant increase in produced photocurrent can be obscured by low voltage if efficiency alone is studied. In the following the short circuit current,  $I_{SC}$  which is a measure of how much current the cell can produce, is presented as function of Au RSA, the plots are grouped as described before.

Studying the power efficiency, the attention is on the the generation of usable electrons, that is electrons that actually reach the outer circuit of the cell where it contributes to the efficiency and can be used for electrical work. It is a known fact that some of the photoexcited electrons are recombined somewhere between the excitation and the entering of the outer circuit. There are a several possible routes for recombinations between these events and the main parts of the recombinations will be to oxidized dye molecules or to the electrolyte, see Figure 11 on page 28. These recombinations will most probably affect the produced usable cell current and voltage, which in turn affects the efficiency. Recombinations are not measured or even estimated in this work but it should be kept in mind that these processes are always present to some extent. The currents presented in the following are the actual measured currents in an outer circuit.

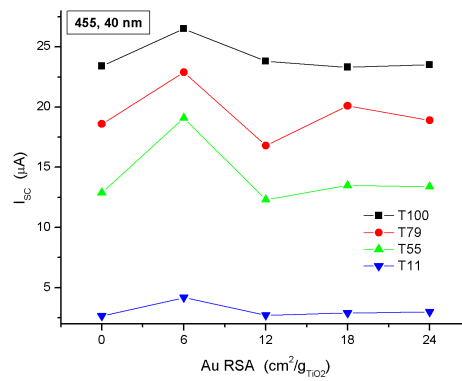
## Short circuit current at different light intensity



(a) Short circuit current  $I_{SC}$  for cells containing 5 nm GNPs and dye 455 at different light intensities.



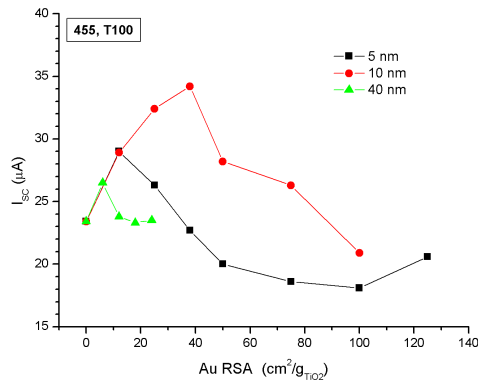
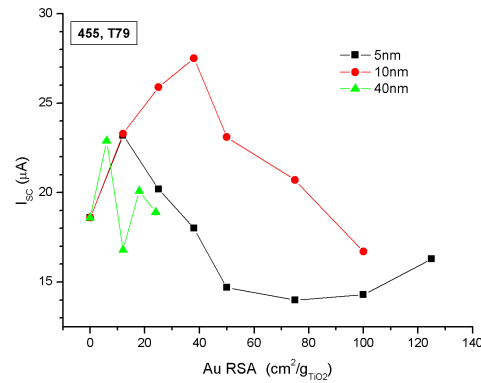
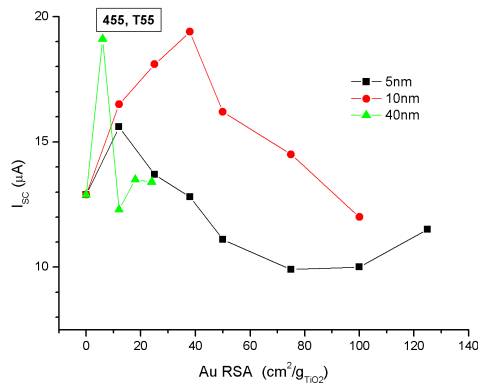
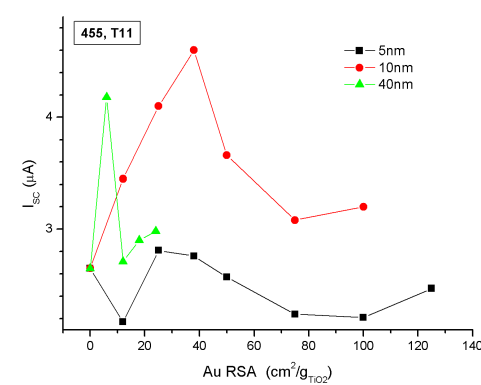
(b) Short circuit current  $I_{SC}$  for cells containing 10 nm GNPs and dye 455 at different light intensities.



(c) Short circuit current  $I_{SC}$  for cells containing 40 nm GNPs and dye 455 at different light intensities.

Figure 52: Short circuit current  $I_{SC}$  as function of Au RSA for different light intensities and dye 455-PF6.

## Short circuit current for different GNP size

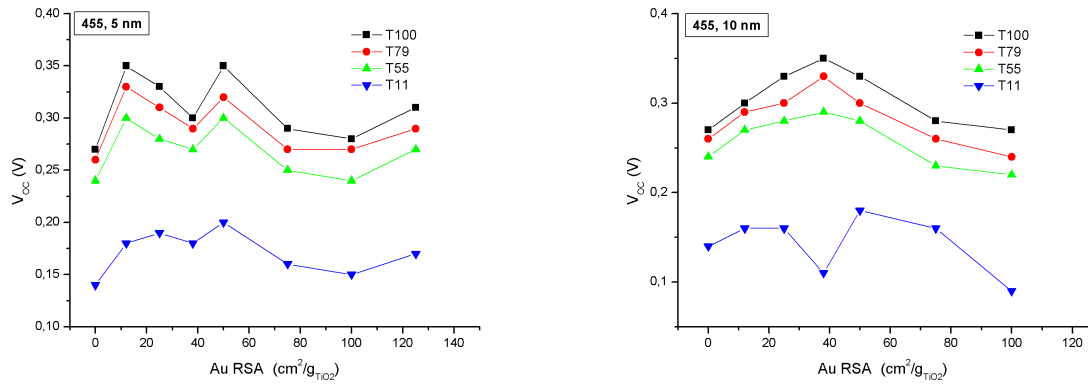
(a) Short circuit current  $I_{SC}$  for different cells with GNP size 5, 10 or 40 nm with T100 and dye 455.(b) Short circuit current  $I_{SC}$  for different cells with GNP size 5, 10, or 40 nm with T79 and dye 455.(c) Short circuit current  $I_{SC}$  for different cells with GNP size 5, 10, or 40 nm with T55 and dye 455.(d) Short circuit current  $I_{SC}$  for different cells with GNP size 5, 10, or 40 nm with T11 and dye 455.**Figure 53:** Short circuit current  $I_{SC}$  as function of Au RSA for different GNP size and dye 455-PF6.

There is a peak behaviour for the short circuit current  $I_{SC}$  as function of Au RSA, the peak occurs at different Au RSA for the the different GNP sizes; for 5 nm at 12 , for 10 nm at 38 and for 40 nm at 6 cm<sup>2</sup>/g<sub>TiO<sub>2</sub></sub> Au RSA. Comparing the graphs of short circuit current and efficiency as function of Au RSA, it is seen that the 5 nm cells peak in  $I_{SC}$  at less Au RSA than the efficiency (12 instead of 25 cm<sup>2</sup>/g<sub>TiO<sub>2</sub></sub>) while the 10 nm and 40 nm cells peak at the same values of Au RSA. When comparing the graphs in Figure 48 on page 95 and Figure 52 on the previous page, it is also clear that the  $I_{SC}$  is more reactive to variations in light intensity than efficiency.

The highest value of  $I_{SC}$  is achieved by using 10 nm GNP. It is also observed that the  $I_{SC}$  is always increasing with increasing light intensity, this was not the case with the efficiency. This shows that the overall efficiency is not solely limited by poor absorption and photon to electron conversion but also how the cell voltage follows the variations in current.

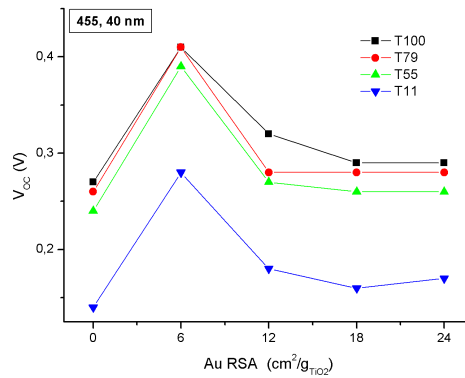
9.4.8 Open circuit voltage of cells in series 2

Open circuit voltage at different light intensity



(a) Open circuit voltage  $V_{OC}$  for cells containing 5 nm GNPs and dye 455 at different light intensities.

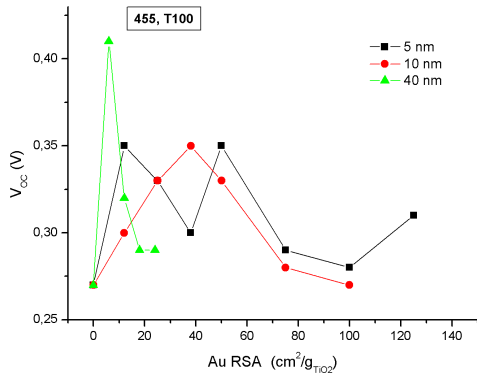
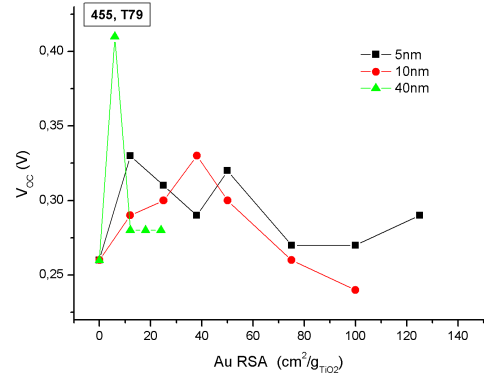
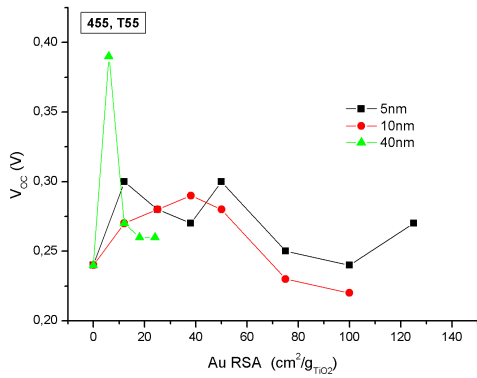
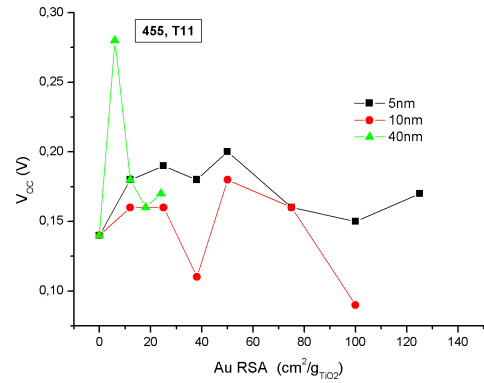
(b) Open circuit voltage  $V_{OC}$  for cells containing 10 nm GNPs and dye 455 at different light intensities.



(c) Open circuit voltage  $V_{OC}$  for cells containing 40 nm GNPs and dye 455 at different light intensities.

Figure 54: Open circuit voltage  $V_{OC}$  as function of Au RSA for different light intensities and dye 455-PF6.

## Open circuit voltage with different GNP size

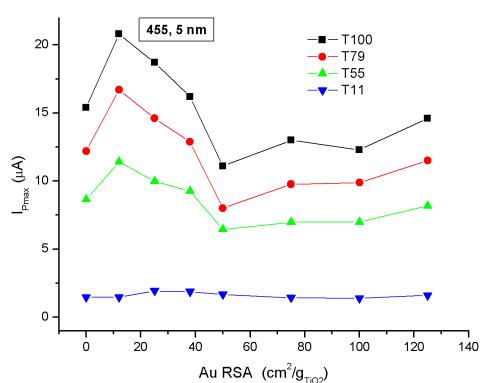
(a) Open circuit voltage  $V_{OC}$  for different cells with GNP size 5, 10, or 40 nm with T100 and dye 455.(b) Open circuit voltage  $V_{OC}$  for different cells with GNP size 5, 10, or 40 nm with T79 and dye 455.(c) Open circuit voltage  $V_{OC}$  for different cells with GNP size 5, 10, or 40 nm with T55 and dye 455.(d) Open circuit voltage  $V_{OC}$  for different cells with GNP size 5, 10, or 40 nm with T11 and dye 455.**Figure 55:** Open circuit voltage  $V_{OC}$  as function of Au RSA for different GNP size and dye 455-PF6.

The open circuit voltage shows peak behaviour as function of Au RSA and the 40 nm cells show the most pronounced peak. The 5 nm cells show a dip at  $38 \text{ cm}^2/\text{g}_{\text{TiO}_2}$  Au RSA at all four intensities of light. The dip might be caused by poor function of this particular cell (cell nr. 20, 5 nm GNPs and  $38 \text{ cm}^2/\text{g}_{\text{TiO}_2}$  Au RSA). The highest value of  $V_{OC}$  is reached with the 40 nm GNPs, this value is 0.41 v and it occurs at  $6 \text{ cm}^2/\text{g}_{\text{TiO}_2}$  Au RSA. For the 5 and 40 nm cells the shape of the graphs are similar when compared between the different light intensities.

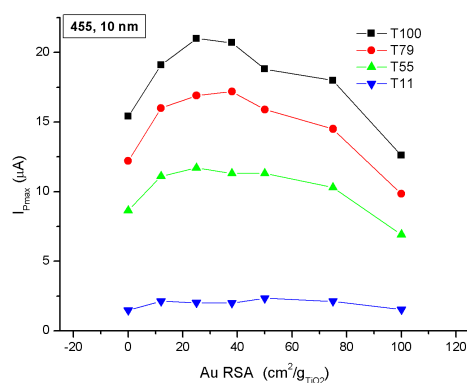
### 9.4.9 Current at maximum power of cells in series 2

The current at maximum power as function of Au RSA and light intensity might bring information about how the actual produced current is varying at the point where efficiency is evaluated. Figures 56 and 57 on the next page show graphs of  $I_{P_{max}}$  vs Au RSA for different GNP size and light intensities at the point of maximum power.

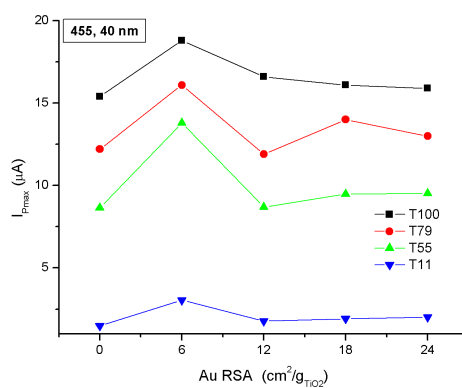
#### $I_{P_{max}}$ at different light intensity



(a) Current at maximum power  $I_{P_{max}}$  for the 5 nm GNPs and dye 455-PF6 at different light intensities

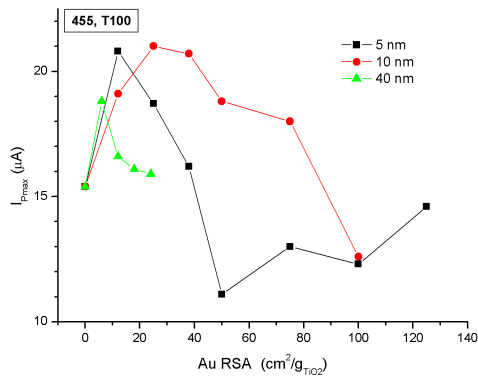
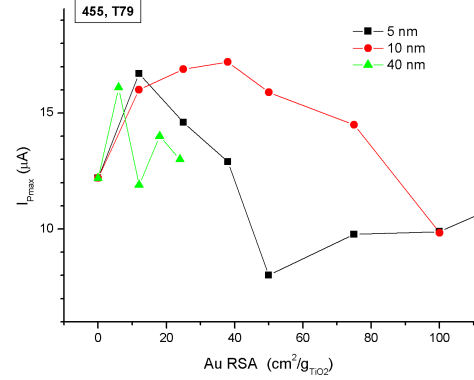
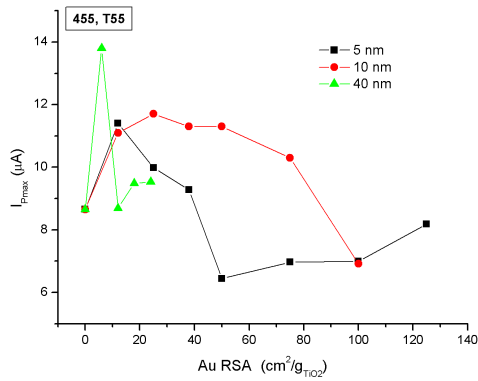
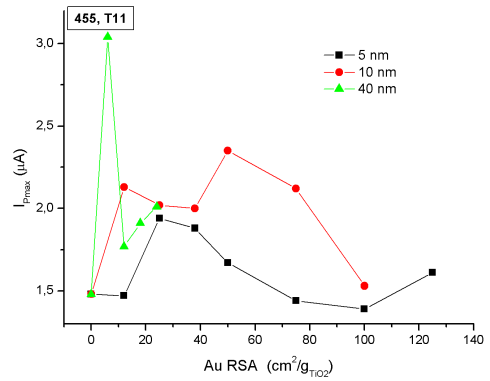


(b) Current at maximum power  $I_{P_{max}}$  for the 10 nm GNPs and dye 455-PF6 at different light intensities



(c) Current at maximum power  $I_{P_{max}}$  for the 40 nm GNPs and dye 455-PF6 at different light intensities

Figure 56: Current at maxpower,  $I_{P_{max}}$  as function of Au RSA for different light intensities and dye 455-PF6.

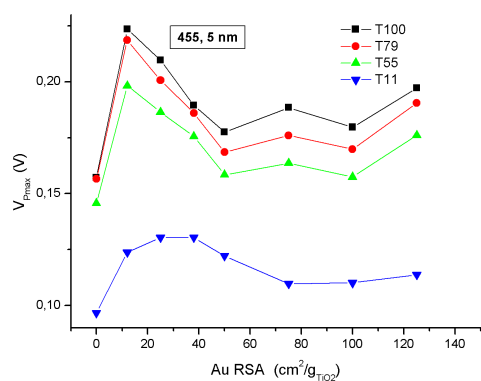
$I_{P_{max}}$  with different GNP size(a) Maxcurrent  $I_{P_{max}}$  for different cells with GNP size 5, 10, or 40 nm with T100 and dye 455.(b) Maxcurrent  $I_{P_{max}}$  for different cells with GNP size 5, 10, or 40 nm with T79 and dye 455.(c) Maxcurrent  $I_{P_{max}}$  for different cells with GNP size 5, 10, or 40 nm with T55 and dye 455.(d) Maxcurrent  $I_{P_{max}}$  for different cells with GNP size 5, 10, or 40 nm with T11 and dye 455.**Figure 57:** Current at maxpower  $I_{P_{max}}$  as function of Au RSA for different GNP size and dye 455-PF6.

$I_{P_{max}}$  as function of Au RSA has a peak behaviour for all three GNP sizes, the peak occurs at different Au RSA for the different GNPs. The peaks occurs at;  $12 \text{ cm}^2/\text{g}_{\text{TiO}_2}$  Au RSA for the 5 nm,  $25\text{-}38 \text{ cm}^2/\text{g}_{\text{TiO}_2}$  for the 10 nm and  $6 \text{ cm}^2/\text{g}_{\text{TiO}_2}$  for the 40 nm GNPs. Both 5 nm and 40 nm GNPs have more distinct peaks than the 10 nm GNPs. The current at maximum power is increasing for increased light intensity, this was also the case for the short circuit current.

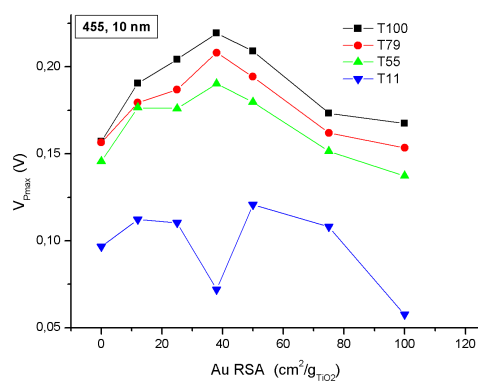
### 9.4.10 Voltage at maximum power of cells in series 2

The variation of the cell voltage at the working point where the power reaches maximum as function of Au RSA for different GNP sizes and light intensity is presented in Figures 58 and 59 on the next page.

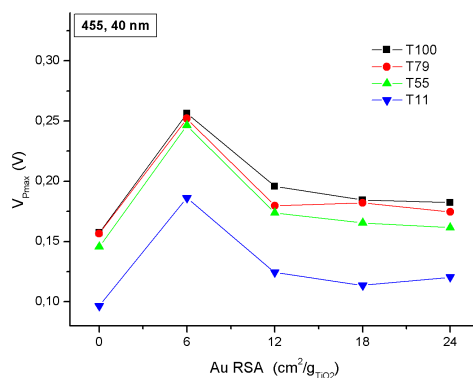
#### $V_{P_{max}}$ at different light intensity



(a) Voltage at maximum power  $V_{P_{max}}$  for the 5 nm GNPs and dye 455

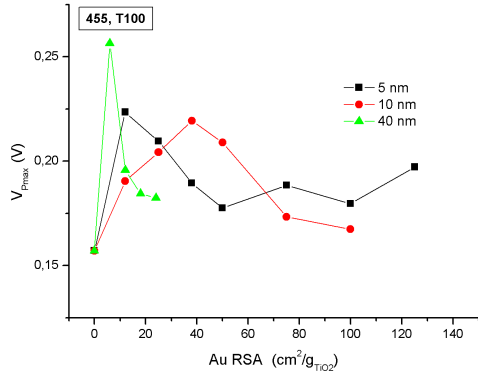
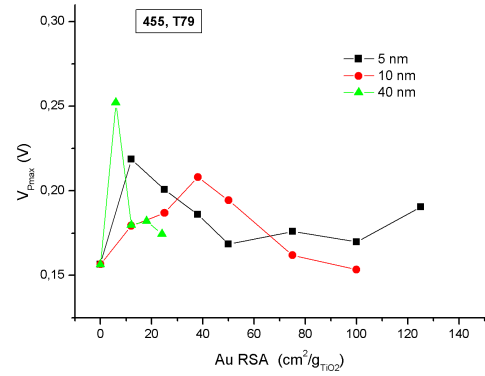
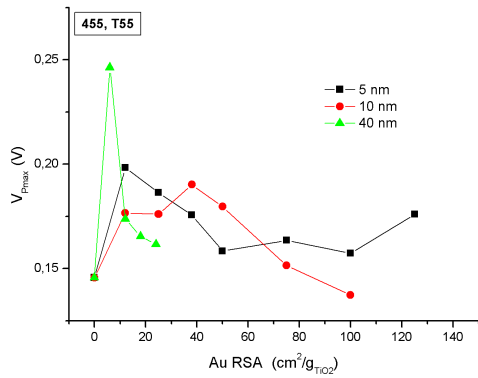
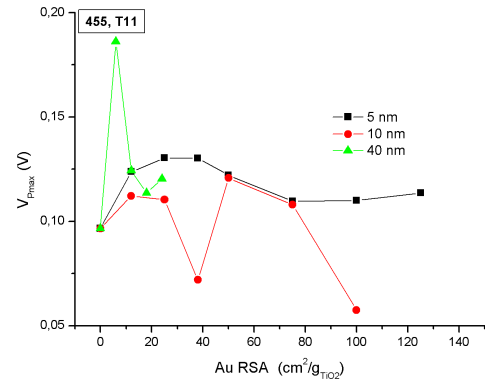


(b) Voltage at maximum power  $V_{P_{max}}$  for the 10 nm GNPs and dye 455



(c) Voltage at maximum power  $V_{P_{max}}$  for the 40 nm GNPs and dye 455.

**Figure 58:** Voltage at maximum power,  $V_{P_{max}}$  as function of Au RSA for different light intensities and dye 455-PF6.

$V_{Pmax}$  with different GNP size(a) Voltage at maximum power,  $V_{Pmax}$  for different cells with GNP size 5, 10 or 40 nm with T100 and dye 455(b) Voltage at maximum power,  $V_{Pmax}$  for different cells with GNP size 5, 10 or 40 nm with T79 and dye 455(c) Voltage at maximum power,  $V_{Pmax}$  for different cells with GNP size 5, 10 or 40 nm with T55 and dye 455(d) Voltage at maximum power,  $V_{Pmax}$  for different cells with GNP size 5, 10 or 40 nm with T11 and dye 455-PF6**Figure 59:** Voltage at maxpower,  $V_{Pmax}$  as function of Au RSA for different GNP size and dye 455.

The voltage at maximum power,  $V_{Pmax}$ , has a peak behaviour for all three GNP sizes, the peaks occurs at different Au RSA for each of them; they occur at 25, 38 and 6  $\text{cm}^2/\text{g}_{TiO_2}$  Au RSA for the 5 nm, 10 nm and 40 nm cells respectively. The 10 nm has a significant local minimum at 38 Au RSA for the T11 light, this might be a measurement error.  $V_{Pmax}$  follows the same pattern for the different light intensities. In general,  $V_{Pmax}$  is increasing with increased light intensity. The pattern of  $V_{Pmax}$  as a function of Au RSA is similar to that of  $I_{Pmax}$ .

When comparing the graphs in Figure 48 on page 95 to Figure 59 on the previous page showing the properties;  $\eta$ ,  $FF$ ,  $I_{SC}$ ,  $V_{OC}$ ,  $I_{Pmax}$  and  $V_{Pmax}$  as function of Au RSA, some pattern emerges. A peak behaviour shows for most of these properties, where positive effects are achieved up to a certain level of Au RSA. For amounts above this level the positive effect declines and in some cases the effects of adding GNPs are even negative at high enough levels. It was also shown that adding GNPs to cells without sensitizing dyes was contra productive and decreased the cell efficiency for all amounts of GNPs that were used in this work.

For the 5 and 10 nm cells the peak values appear at different amount of GNPs but for the 40 nm cells the peak values occur at the same amount of gold,  $6 \text{ cm}^2/\text{g}_{TiO_2}$  for all the properties mentioned above. As mentioned in Section 2, GNPs of size 5 to 20 nm might not contribute to scattering of the light [21]. This might implicate that the properties;  $\eta$ ,  $I_{SC}$ ,  $V_{OC}$ ,  $FF$ ,  $I_{Pmax}$  and  $V_{Pmax}$  for cells containing 40 nm GNPs is affected more by the scattering effects from the GNPs than effects of enhanced near fields. It was also shown that the best response for cells with 40 nm GNPs was achieved with Au RSA of  $6 \text{ cm}^2/\text{g}_{TiO_2}$ . One reason for the peak to occur at this same amount of GNP might be that effects of reflections and screening of light will lower the photon flux significantly in the photoactive layers for gold amounts higher than  $6 \text{ cm}^2/\text{g}_{TiO_2}$  when 40 nm GNPs are used.

Looking at these result it seems that the 40 nm GNPs produces cells with the most positive response to added amount of gold if cell efficiency is considered. However, it should be kept in mind that these graphs show efficiency versus Au RSA which is not the same as relative amounts measured in number of particles or mass of gold. To see which GNP size increased the efficiency most per number of particles or mass of gold, some translation calculations needs to be done. Translation between the quantities total surface area, number of GNPs and mass of gold is shown in Table 18 on page 87.

An example of comparison; the efficiency graphs in Figure 49 on page 96 show that efficiency peaks at 25, 38 and  $6 \text{ cm}^2/\text{g}_{TiO_2}$  Au RSA for the 5 nm, 10 nm and 40 nm cells respectively. If these values are used and translated according to Table 18 on page 87 the result is; using 5 nm, 10 nm and 40 nm GNPs would require 16.1, 48.9 and 30.9 mass units of gold respectively. This means that if mass of gold is to be considered, the most efficient concept for reaching the efficiency peak would be to use GNPs of size 5 nm at  $25 \text{ cm}^2/\text{g}_{TiO_2}$  Au RSA, the second most efficient would be 40 nm GNPs at  $6 \text{ cm}^2/\text{g}_{TiO_2}$  and the least efficient is 10 nm GNPs at  $38 \text{ cm}^2/\text{g}_{TiO_2}$ .

## 10 Conclusions and outlook

### Conclusions

As a first study, experiments using different sensitizing dyes; Ruthenizer 455-PF6, Ruthenizer 620-H3TBA and Sensidizer SQ2 in combination with 10 nm GNPs in different amounts were performed. Cells were built and characterized with I-V graphs at different light intensities. These experiments showed that, when cell efficiency is considered, cells sensitized with Ruthenizer 455-PF6 dye were most positively sensitive to addition of GNPs in the photoactive layer.

In a second series of experiments, the Ruthenizer 455-PF6 dye was further tested in combinations with 5 , 10 and 40 nm GNPs in different amounts. Cells were built and characterized the same way as for series 1.

It was observed that the dependence on cell efficiency of variations in Au concentration show a peak behaviour for all three sizes of GNPs. This peak occurs at different Au concentration for the different sized GNPs. The cells containing 40 nm GNPs have the most pronounced efficiency peak. This peak is reached at  $6 \text{ cm}^2/g_{\text{TiO}_2}$  Au RSA, independent of light intensity. Cells containing 5 nm and 10 nm GNPs reach their peak values at higher Au RSAs, 25 and  $38 \text{ cm}^2/g_{\text{TiO}_2}$  respectively.

From a separate study of nitric acid effects on the GNP colloids of size 5, 10 and 40 nm, it was shown that nitric acid affects the optical properties of the gold colloids significantly. Both the absorbance and the surface plasmon absorption maximum,  $\lambda_{max}$  were affected by the acid. The smallest GNPs (5 nm) were less affected than the 10 nm and the 40 nm GNPs. This shows that, due to the nitric acid in the  $\text{TiO}_2$  slurry, the actual size and shape of the GNPs in the final annealed  $\text{TiO}_2$  layers, might differ compared to what was originally in the added GNP colloid.

The surface plasmon absorption maximum was affected differently for colloids of different sized GNPs. However, a red shift in the absorption-spectra was observed for all three sizes of GNPs when nitric acid was added to the colloids.

From I-V characterizations of cells containing different amount of nitric acid, efficiency was observed to decrease with decreasing amount of nitric acid used in the  $\text{TiO}_2$  slurry. This clearly shows that efficiency can not be improved just by decreasing the amount of nitric acid.

### **Future work**

Interesting future work connecting to this work would be finding methods to measure and identify the final size and shape of the GNPs in the annealed TiO<sub>2</sub> films. This would provide very useful information when results from experiments similar to this are evaluated and discussed in terms of GNP size.

Another interesting approach would be to explore possibilities of replacing nitric acid by some other substance that does not affect the GNP size and shape. Exploring other approaches as for ex; not placing the GNPs directly into the acidic TiO<sub>2</sub> slurry might also solve the problem of GNPs degrading in acidic environments.

Furthermore, it is of greatest interest to look for new dyes that might work even more efficiently in combination with metal nano particles in the concept of DSSCs.

Considering the results from this work it looks promising that cell efficiencies can be improved by using nanoplasmonic effects, because poor efficiency is an issue that has to be properly addressed if the dye sensitized solar cells should be able to compete on the future market of solar energy converters.

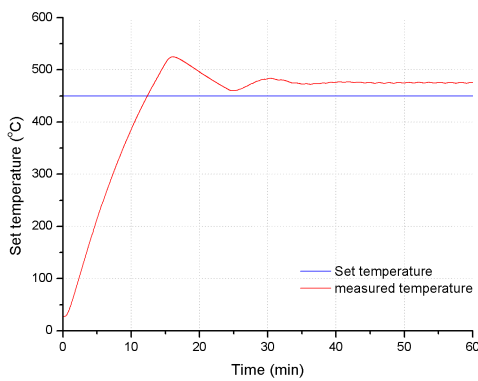
## A Furnace test

The furnace used for annealing of the anode electrodes was controlled with respect to the dynamics of the temperature response and the residual error in the final temperature. The furnace used for this is a chamber furnace, type GEM PD from Carbolite equipped with a temperature control unit from Eurotherm. The control unit has two controls to be set by the user, one for final temperature and one for regulation parameters which control the dynamic response of the furnace. In this work two settings of the regulation parameters were used, fast regulation and slow regulation which correspond to the highest and lowest rate of temperature increase respectively. Four different measurements were carried out, all with the same final temperature setting of 450 °C. Two methods for temperature setting were used, setting to 450 °C directly or raising the setting in steps following a program. The different measurements were set up as shown in Table 22.

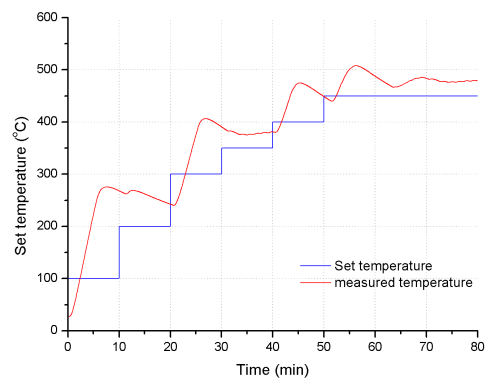
**Table 22:** The different measurement set-ups.

Regulation	Method
Fast	Temperature directly set to 450
Fast	Temperature set according to program
Slow	Temperature directly set to 450
Slow	Temperature set according to program

Graphs showing the results of the measurements is found in Figures 60 and 61, the red graph shows the temperature setting program.

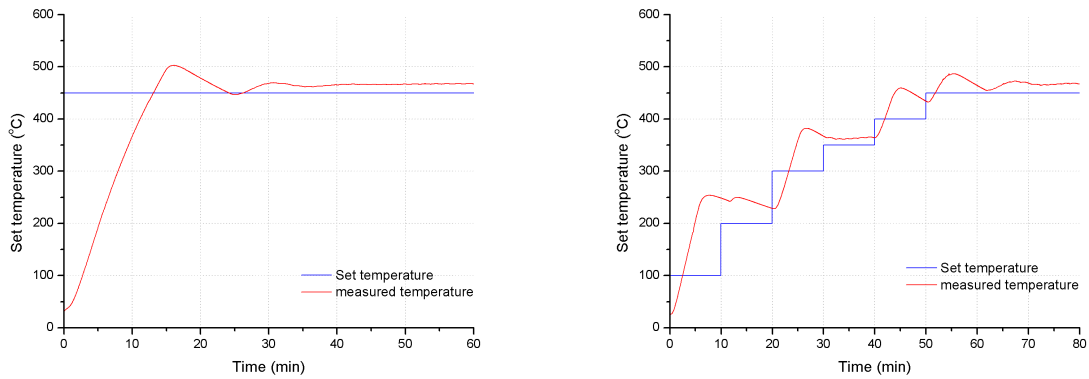


(a) Temperature with fast regulation and temperature directly set to 450 °C.



(b) Temperature with fast regulation and temperature set to 450 °C following a program.

**Figure 60:** The two measurements carried out with fast regulation of the temperature. (a) Without using temperature setting program. (b) Using temperature setting program.



(a) Temperature response with with slow regulation and temperature directly set to 450 °C.

(b) Temperature response with slow regulation and temperature set to 450 °C following a program

**Figure 61:** The two measurements carried out with slow regulation of the temperature. (a) Without using temperature setting program. (b) Using temperature setting program.

The results show that the actual temperature of the furnace overshoot the set value, not only for the temporary maximum value but also for the final value, resulting in residual errors <sup>1</sup>. Both the transient errors and the residual ones are larger when the fast regulation setting is used. If the temperature is set to 450 °C directly, the final value is reached within 40 minutes with fast regulation and within 50 minutes with slow regulation. Some values from this measurements showing absolute and relative errors are collected in Table 23.

**Table 23:** Result from furnace measurements. Relative overshoot of the temperature is calculated as difference between maximum measured ( $T_m$ ) and set temperature ( $T_s$ ), divided by set temperature. Relative error is the difference between final temperature ( $T_f$ ) and set temperature, divided by set temperature.

Measurement type	Max temp. [°C]	Rel. overshoot [%]	Final temp. [°C]	Residual error [°C]	Relative error [%]
Fast regulation	525	17	475	25	5
Fast regulation - pgm.	508	13	479	29	6
Slow regulation	503	12	467	17	4
Slow regulation - pgm.	487	8	468	18	4

For the annealing of TiO<sub>2</sub> films in this work, the furnace was always used with the slow setting, following the setting program and final temperature set to 450 °C. This means that the actual annealing temperature of the TiO<sub>2</sub> films was about 470 °C.

<sup>1</sup> residual error = difference between set value and final value of temperature

## B Solar simulator test

To produce light irradiation with spectral distribution similar to sunlight, a solar simulator, model LS0106 from LOT Oriel was used. The power of the simulated light from this device was specified to 1 sun which corresponds to a power of  $1000 \text{ W/m}^2$  in radiometric units. The light source within this simulator is a 150 W xenon lamp. This lamp in combination with a built in AM 1.5 filter produces a spectral distribution of light that resembles natural AM 1.5 sunlight.

With the set-up used in this work, the solar simulator produced a 35 mm diameter light beam in the working plane at a distance of 80 mm from the condenser lens. The solar cells that were to be irradiated were much smaller than this. The typical irradiated area of solar cells used in this work is approximately 7 by 7 mm. A mask with known aperture was used to have control of the irradiated power, this made the utilized area in the light beam even smaller. The smaller size of the irradiated cell area compared to the light beam cross section area makes it possible to place the cell in different positions, still having the irradiated area completely within the light beam cross section area.

Therefore, before the actual measurements were performed on solar cells with this set-up, the homogeneity of the light beam in the working plane as well as stability in time was studied with respect to optical power. This was performed using a photo detector to measure the power in different known positions in the working plane of the light beam. Positions and measured data were saved for evaluation. The photo detector used for this was a sun calibrated reference detector, model 3275-01 from Sciencetech Inc. with a known calibration for light with spectra similar to sunlight. The responsivity was declared as 1.81 mA/sun from the manufacturer.

In addition, two photo diodes were also used; a FDS100 from Thor-Labs and a BPW 21 from OSRAM. Measurements with these two diodes were made just for comparison of the more sophisticated instrument from Sciencetech. The measurements with the 3275-01 detector were made in 17 different position while the photo diodes were used in 5 of these positions. Figure 62a on page 117 shows how the positions were chosen.

The study of the homogeneity clearly showed that the produced power of the light varied significantly in different positions in working plane of the beam. For the stability in time, it was found that the power in fixed positions varied during the first 30 minutes after start and after that it was stable in time.

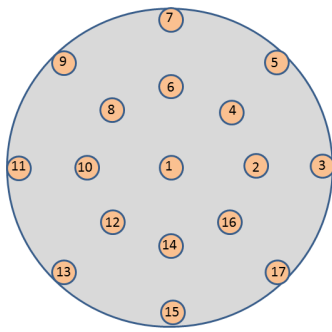
The measured variations of power in different positions in the light beam is shown in Table 24 on the following page and a graphic presentation of the result is shown in Figure 62b on page 117. A comparison between the calculated values in units of one sun shows quite large differences between the three detectors. In a separate study where the two photo diodes were irradiated with different light intensities by using metal plated flat response filters, it was shown that their responsivities were linear to

the optical power of the light. Considering this, it can be concluded that the variations in the light beam intensity from the solar simulator were not just variations in photon flux but also a spectral variation. In this work, only a relative comparison of effects of different cells were studied and therefore the true value of the power was not needed. On the other hand, for comparison, it was crucial to irradiate the cells with the same spectral distribution and optical power in all measurements.

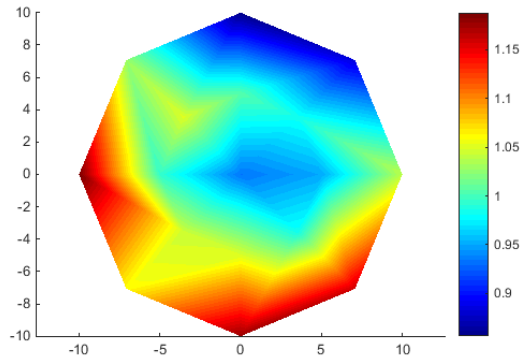
Due to this and the fact of variations in irradiated power at different positions in the light beam, it was decided that a fix position within the light beam, in the working plane, should be used through out all the measurements. The center of the light beam in the working plane was chosen to be the fixed position. The center of the light beam was marked in the working plane of the solar simulator support and the solar simulator was fixed to the support, this way a reliable marking of the chosen position was made. In addition an arrangement with a mask was made to ensure that the samples were placed correctly in every measurement.

**Table 24:** Measured values of power in different positions in the light beam. For the BPW21 and FDS100 photo diodes, only 5 positions were used. The table shows the measured current produced by the detectors in mA and the corresponding optical power in the unit sun (1 sun = 1000 W/m<sup>2</sup>).

Detector	3275-01		FDS100		BPW21	
Position	Current (mA)	Power (sun)	Current (mA)	Power (sun)	Current (mA)	Power (sun)
1	1.69	0.93	0.78	0.93	4.00	0.93
2	1.72	0.95				
3	1.88	1.04	0.90	1.08	4.12	1.31
4	1.78	0.94				
5	1.60	0.88				
6	1.82	1.00				
7	1.55	0.85	0.82	0.99	3.76	1.20
8	1.86	1.03				
9	1.90	1.05				
10	1.94	1.07				
11	2.15	1.19	1.15	1.38	5.25	1.67
12	1.89	1.04				
13	1.92	1.06				
14	1.90	1.05				
15	2.13	1.18	1.08	1.30	4.82	1.53
16	1.78	0.98				
17	2.10	1.16				



(a)



(b)

**Figure 62:** (a) The measuring positions within the light beam of the solarsimulator. (b) The optical power distribution in the light beam cross section area in the working plane of the simulator. The colorbar is graded in the optical power unit sun.



## C Capacitive properties of DSSC

When the IV graphs are measured for a solar cell, a voltage ramp is applied to the solar cell via the potentiostat. The applied voltage is varied between the open circuit voltage and zero while the current is measured, this way the current is varied between zero and the short circuit current. The voltage variation used for this is a linear ramp where the voltage is changed in a step like manner between the initial and final values. An example showing how this voltage variation can be made is presented in Figure 63.

DSSCs are composed of layers of different materials with specific electronic properties. When dynamic voltage signals were imposed on such a system, some capacitive effects were expected to be observed for the measured current. As for capacitive circuits in general, the magnitude of these effects were expected to be dependent of the voltage rate of the actual experiment.

The DSSCs clearly showed capacitive behaviour when I-V measurements were carried out at high enough voltage rates in the potential sweep. As mentioned in the introduction section, a DSSC can be modelled with a circuit containing capacitances as shown in Figure 17 on page 40 [45], so both theoretical modelling and experimental result present the DSSCs as devices with capacitive properties.

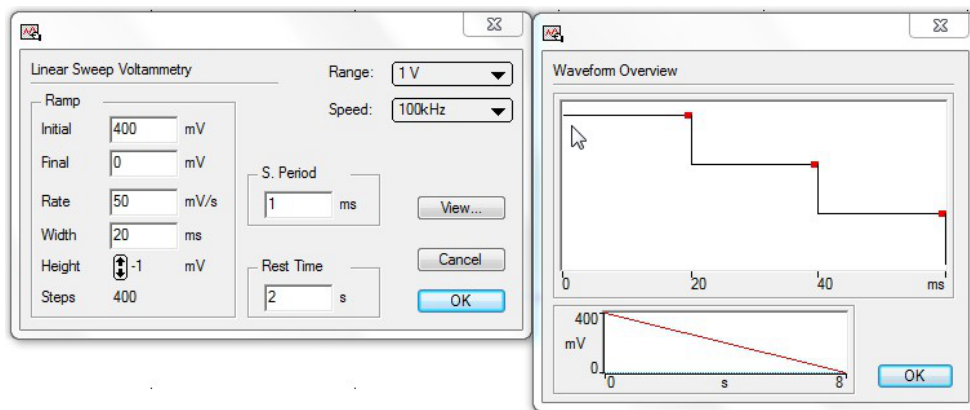


**Figure 63:** The two windows where the parameter settings are made in the measurements with the potentiostat. Here the settings for linear voltammetry is shown to the left, and the step like potential sweep with the sampling period (red marks) for the chosen parameters, to the right.

To study the capacitive behaviour, I-V measurements were carried out using linear sweep voltammetry at different rates of applied voltage. Cells with no GNPs and cells with  $50 \text{ cm}^2/\text{g}_{\text{TiO}_2}$  Au RSA were used. Also the different techniques, doctor blade method and spin coating were included in this experiment to model different thickness

C CAPACITIVE PROPERTIES OF DSSC

of layers. The voltage rates were chosen between 1 and 100 000 mV/s for the spin coated cells and between 50 and 5000 mV/s for the doctor bladed one. All measurements were carried out with low pass filtering of 10 Hz to avoid disturbance from mains hum (50 Hz). All cell types and instrument settings used for the measurements are declared in Table 25, the setting windows for the linear sweep voltammetry are shown in Figure 63 on the previous page. The TiO<sub>2</sub> slurries were composed according to the standard composition as shown in Table 9 on page 65.

**Table 25:** Data of the I-V measurements. Step w. and step h. refers to the width and height of the voltage steps used in the potential sweeps. Sample p. means the actual measuring time and the rightmost column, S.p./S.w shows the ratio of the measuring time to the step width in percent.

Cell type	Doctor blade/ Spin coating	Au RSA (cm <sup>2</sup> /g <sub>TiO<sub>2</sub></sub> )	Rate (mV/s)	Initial (mV)	Step w. (ms)	Step h. (mV)	Sample p. (ms)	S.p./S.w. (%)
no dye	spin coating	0	1	448	1000		0.1	0.01
			10	410	100		0.1	0.1
			100	410	10	-1	0.1	1
			1000	280	1		0.1	10
			10 000	420	0.1		0.01	10
			100 000	420	0.01		0.01	100
no dye	spin coating	50	1	424	1000		1	0.1
			10	430	100		1	1
			100	426	10	-1	1	10
			1000	426	1		1	100
			10 000	426	0.1		0.1	100
			100 000	426	0.01		0.01	100
620	spin coating	0	1	620	1000		0.1	0.01
			10	620	100		0.1	0.1
			100	620	10	-1	0.1	1
			1000	620	1		0.1	10
			10 000	620	0.1		0.01	10
			100 000	620	0.01		0.01	100
620	spin coating	50	1	544	1000		1	0.1
			10	544	100		1	1
			100	544	10	-1	1	10
			1000	544	1		0.1	10
			10 000	544	0.1		0.01	10
			100 000	544	0.01		0.01	100
no dye	doctor blade	0	100	424	10	-1	0.1	1
			300	420	5	-1	0.1	2
			500	420	3	-1	0.1	3
			800	422	1.25	-1	0.01	0.8
			1000	422	1	-1	0.01	1
			1200	420	1.25	-1.5	0.01	0.8
			2000	420	0.75	-1.5	0.01	1
			3000	420	0.5	-1.5	0.01	2
			5000	420	0.3	-1.5	0-0.1	3

The I-V graphs of the cells built with spin coated  $\text{TiO}_2$  films are presented in Figures 64 to 67 and the I-V graphs of the cell built with doctorbladed  $\text{TiO}_2$  film are presented in Figure 68 on page 123.

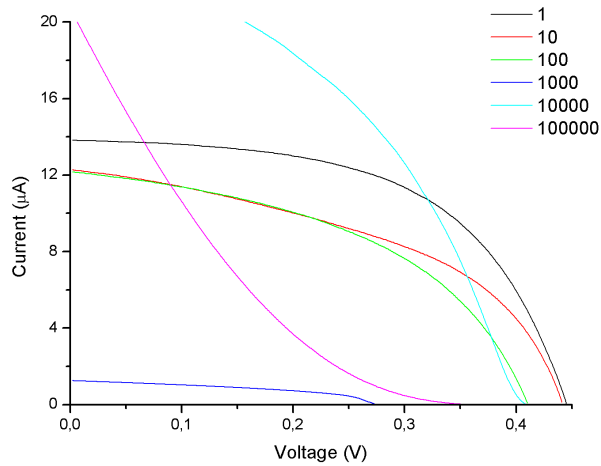


**Figure 64:** I-V graph of cell without dye and GNPs,  $\text{TiO}_2$  slurry applied with spin coating program 95, different voltage rates between 1 and 100000 mV/s.

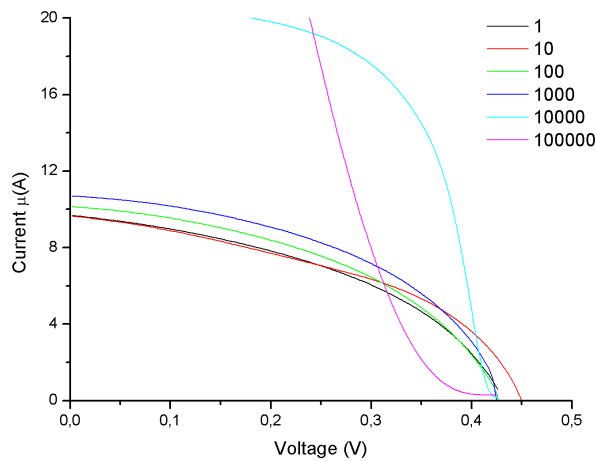


**Figure 65:** I-V graph of cell without dye and  $50 \text{ cm}^2/\text{g}_{\text{TiO}_2}$  Au RSA,  $\text{TiO}_2$  slurry applied with spin coating program 95. Voltage rates between 1 and 100000 mV/s were used.

From the graphs in Figure 64 and 65, it is seen that the capacitive effects are significantly affecting the result for rates above 1000 mV/s. In Figure 64 the graph for 1000 mV/s is different from the others, this might be because some error in this specific measurement.

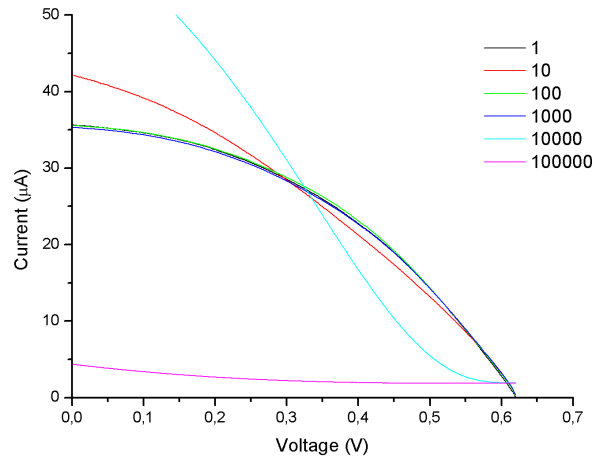


**Figure 66:** I-V graph of cell with dye 620-1H3TBA and no GNPs, TiO<sub>2</sub> slurry applied with spin coating program 95. Voltage rates between 1 and 100000 mV/s were used.

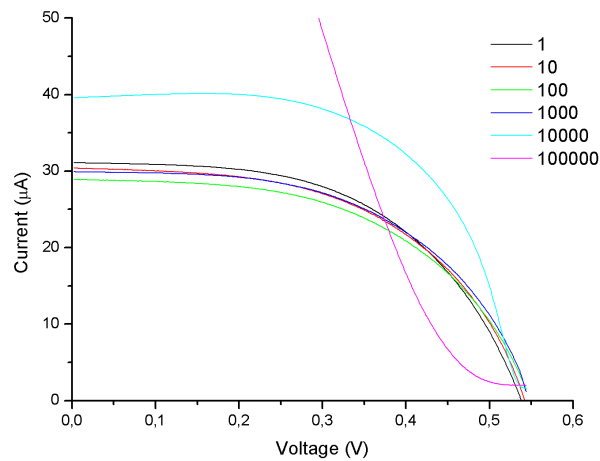


**Figure 67:** I-V graph of cell with dye 620-1H3TBA and 50 cm<sup>2</sup>/gTiO<sub>2</sub> Au RSA, TiO<sub>2</sub> slurry applied with spin coating program 95. Voltage rates between 1 and 100000 mV/s were used.

In Figure 66 and 67 it is seen that the capacitive effects are significantly affecting the measurements, in Figure 66 the graph representing 10 mV/s is a bit different, this might be caused by measurement error. Comparing all four cells prepared with spin coated electrodes it seems that the capacitive effects are strongly affecting the I-V measurements at voltage rates above 1000 mV/s. The measurements above 1000 mV/s in general have a larger ratio of sampling period to step width as can be seen in Table 25 on page 120. There are limitations how to choose these parameters and the used ones were the best available for the actual measurements. It is hard to tell how a different equipment offering other settings would have corrected better for the capacitive effects.

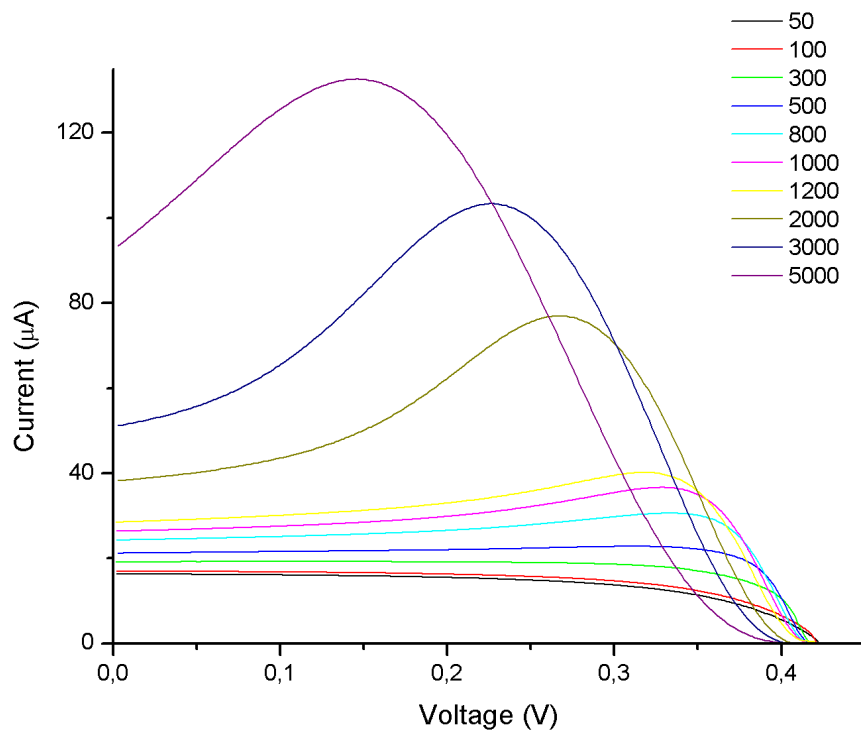


**Figure 68:** I-V graph of cell without dye and GNPs, TiO<sub>2</sub> slurry applied with the doctor blade method. Voltage rates between 50 and 5000 mV/s were used.

Figure 68 shows the I-V graphs for the cell prepared with the doctor blade method. The voltage rates here are chosen closer above the value, for which the capacitive effects starts to affect than for the spin coated ones, the reasons for this are limitations in the parameter settings for the potentiostat.

The I-V graphs for the doctor bladed cell clearly shows that the capacitive effects starts to affect the measurements at 300 mV/s. This is lower than what was found for

the spin coated cells. Apart from the method of applying the slurries, the cells that produced the I-V graphs in Figure 64 on page 121 to Figure 67 on page 122 were all prepared in the same way so the explanation for different capacitive behaviour might be found be within the TiO<sub>2</sub> layer. From the experiments carried out to find the optimal slurry composition it was clear that the doctor bladed slurries were thicker than the spin coated so there might be a correlation between the capacitive effect and the thickness of the TiO<sub>2</sub> layer.

## D Nitric acid effects on GNPs

During preparations of  $\text{TiO}_2$  slurries containing 5 nm GNPs it was observed that the optical properties of the GNPs were affected when nitric acid was added to the solutions containing the GNPs. The reaction was observed by visual inspection shortly after the nitric acid was added. The solution of triton, carbowax, deionized water and gold colloids changed color from a bright pink shade to a more dark shade and then finally to a more clear and colorless solution. The more gold the solution contained the more pronounced the effect was. For the sample with  $125 \text{ cm}^2/\text{g}_{\text{TiO}_2}$  Au RSA, the solution became more or less colorless. In some of the samples, dark particles, large enough to be seen with the bare eye, was observed after about 1 hour. The different change of color for samples containing different amounts of GNPs is shown in Figure 69 which shows a photograph of a series of different samples 2 hours after adding the nitric acid to the solutions.



**Figure 69:** Photograph showing solutions of nitric acid, triton X-100, carbowax, deionized water and different amount of gold colloids containing 5 nm GNPs

To study the effects of nitric acid in the slurry on the absorption spectra of the gold colloids and on the performance of the solar cells, two series of experiments were carried out.

1. Comparing absorption spectra of gold colloids with different amounts of  $\text{HNO}_3$  added. A series of 6 samples of gold colloid and nitric acid were prepared in compositions as presented in Table 26 on the next page. The absorption spectra of the samples were measured in the wavelength interval 300 - 900 nm (4.13 - 1.38 eV).

2. Comparing performance of cells containing different amounts of HNO<sub>3</sub>. A series of 6 solar cells containing GNPs of 5 nm respectively 10 nm with 25 cm<sup>2</sup>/g<sub>TiO<sub>2</sub></sub> Au RSA and different amounts of HNO<sub>3</sub> were prepared and characterized with I-V measurements.

## D.1 Absorption measurements

The absorption measurements were carried out with the same experimental setting as for the other absorption measurements in this work, these are presented in Table 16 on page 79. A series of 6 samples were mixed and subsequently measured twice with the spectrometer. The measurements were also carried out at fixed points in time, first measurements 10 min after mixing and the second ones after 60 min. To be able to do this in a controlled and comparable way, a time schedule containing all operations was followed, the schedule is shown in Table 27

**Table 26:** The compositions of the samples containing gold colloids and nitric acid prepared for absorption measurements.

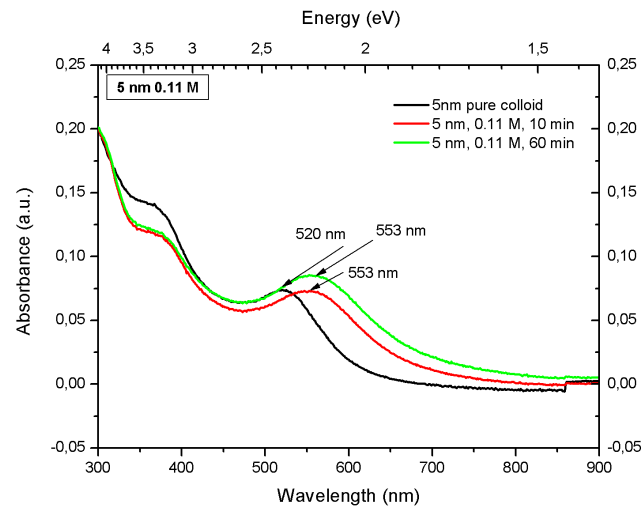
Sample	A1	A2	B1	B2	C1	C2
Gold nanoparticle size (nm)	5	5	10	10	40	40
HNO <sub>3</sub> concentration (M)	0.11	0.01	0.11	0.01	0.11	0.01

**Table 27:** The compositions of the samples containing gold colloids and nitric acid prepared for absorption measurements. The notation A1-xx in the table means sample A1 measured xx minutes after mixing the gold colloid and the nitric acid.

Time (min)	Mixing operation	Measuring operation
0	mixing A1	
5	mixing A2	
10		measure A1-10
15		measure A2-10
20	mixing B1	
25	mixing B2	
30		measure B1-10
35		measure B2-10
40	mixing C1	
45	mixing C2	
50		measure C1-10
55		measure C2-10
60		measure A1-60
65		measure A2-60
70		
75		
80		measure B1-60
85		measure B2-60
90		
95		
100		measure C1-60
105		measure C2-60

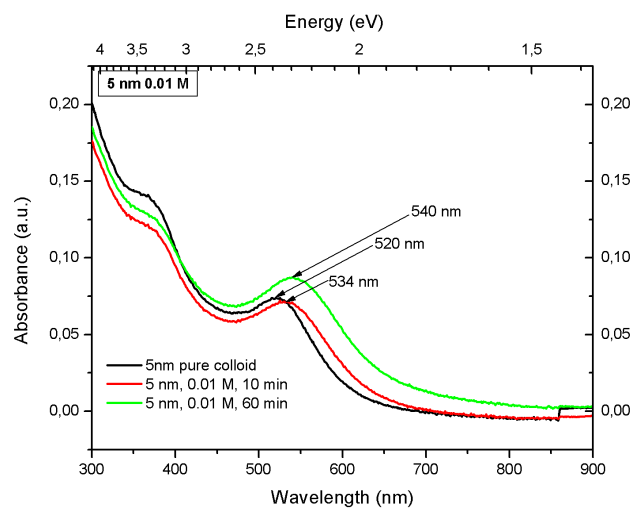
The results from the absorption measurements are presented with graphs in Figure 70 on page 128 to Figure 75 on page 130. There is one figure for each combination of GNP

size and HNO<sub>3</sub> concentration. In each figure there are three graphs, one for the pure gold colloid, one for this colloid mixed with HNO<sub>3</sub> 10 min after mixing and one for this colloid measured after 60 min.



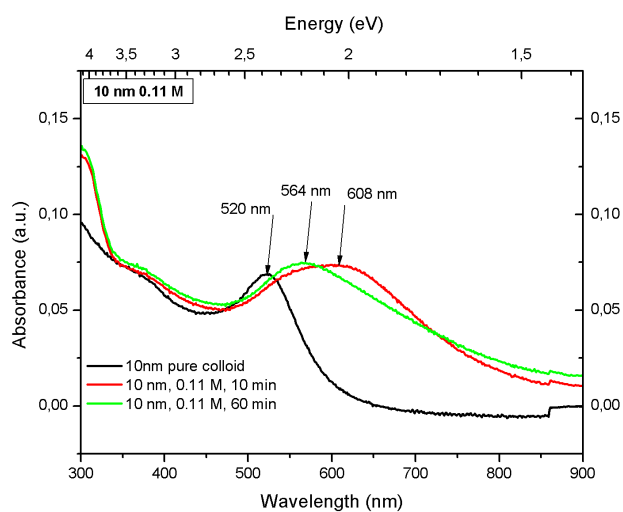
**Figure 70:** Absorption spectra of gold colloid, GNP size 5 nm,  $\text{HNO}_3$  concentration 0.11 M, sample A1.

Figure 70 shows a slight red shift for the absorption peaks for sample A1. After 1 h, the absorbance is increased by  $\sim 13\%$ .



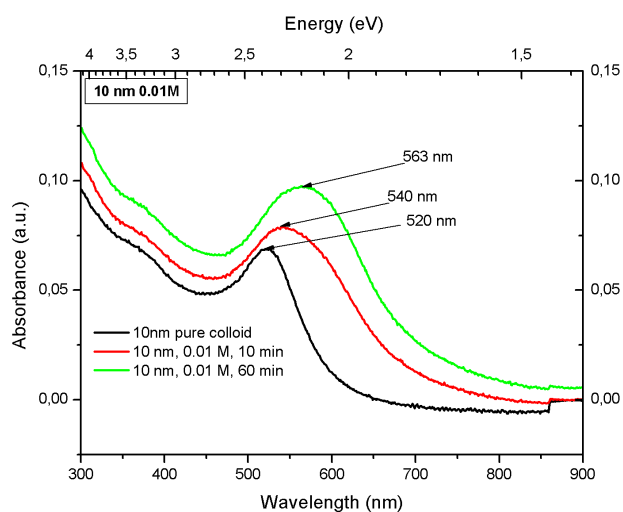
**Figure 71:** Absorption spectra of gold colloid, GNP size 5 nm,  $\text{HNO}_3$  concentration 0.01 M, sample A2.

Figure 71 shows that the red shift for sample A2 is less than for sample A1. The absorbance is increased  $\sim 22\%$  after 1 h.



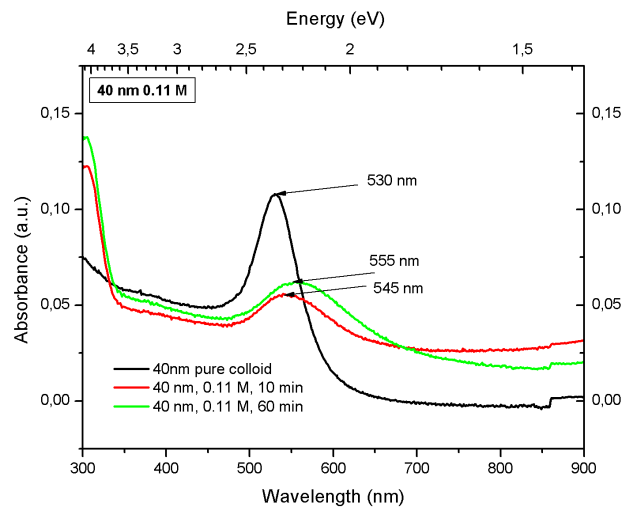
**Figure 72:** Absorption spectra of gold colloid, GNP size 10 nm,  $\text{HNO}_3$  concentration 0.11 M, sample B1.

From Figure 72 it is shown that the red shift of sample B1 is 88 nm after 10 min and after 1 h it is 44 nm. The absorbance is increased  $\sim 7\%$  after 1 h.



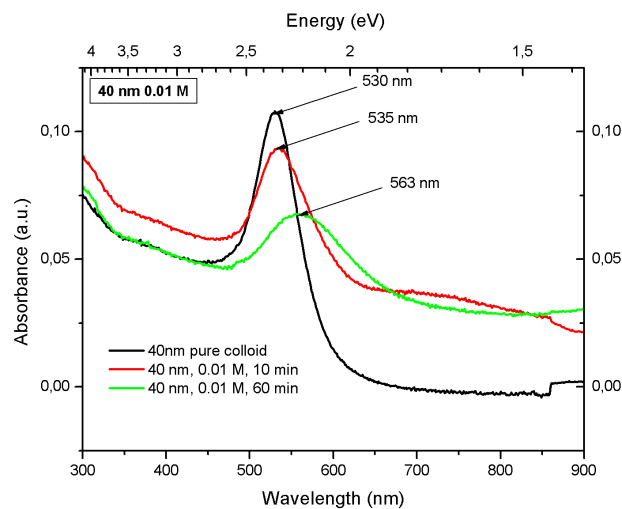
**Figure 73:** Absorption spectra of gold colloid, GNP size 10 nm,  $\text{HNO}_3$  concentration 0.01 M, sample B2.

Figure 73 shows a redshift of 20 nm after 10 min and 43 nm after 1 h for sample B2. The absorbance is increased by about 14 % after 10 min and about 40 % after 1 hour.



**Figure 74:** Absorptionspectra of gold colloid, GNP size 40 nm,  $\text{HNO}_3$  concentration 0.11 M, sample C1.

Figure 74 shows a red shift of 15 nm after 10 min and 25 nm after 1 h for sample C1. The absorbance is lowered by about 49 % after 10 min and by 42 % after 1 h.



**Figure 75:** Absorptionspectra of gold colloid of particle size 40 nm,  $\text{HNO}_3$  concentration 0.01 M, C2.

Figure 75 shows a redshift of 5 nm after 10 min and 33 nm after 1 h for sample C2. The absorbance is lowered by about 13 % after 10 min and by 38 % after 1 h.

Looking at Figure 38 on page 81 for comparison of the absorption spectra of the pure gold colloid, it is seen that the GNP size affects the absorbance significantly but that the peak absorbance frequencies are not altered that much by these size variations. This suggests that absorbance is more size dependent than resonant frequency for the colloids containing GNPs. Here the GNPs are assumed to have their spherical shape as they were delivered from the manufacturer.

During the experiment, interesting visual observations were also made. It was observed that the change in color started directly after mixing the gold colloids and the acids, and then developed gradually. After about 1 hour no further change in color was visually observed. After some two hours small black particles were observed at the bottom of the samples containing nitric acid, see Figure 76

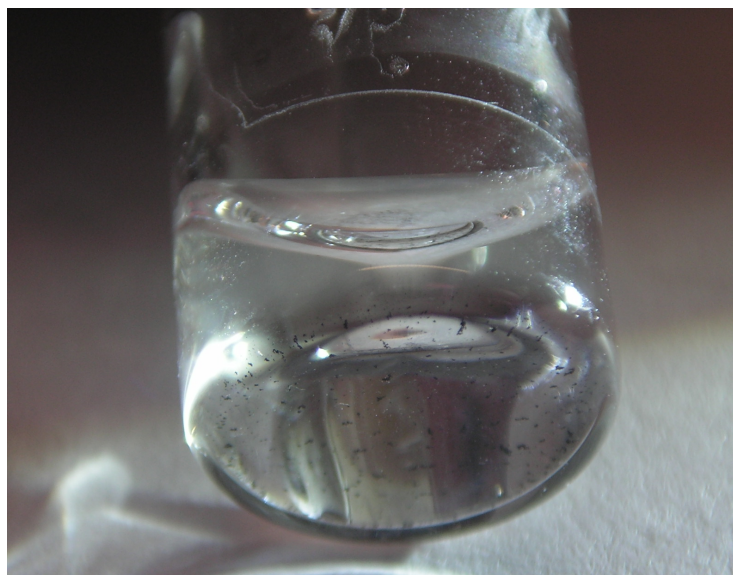


**Figure 76:** Photograph showing sample C1 (40 nm GNP in  $\text{HNO}_3$  0.11 M) 2 hours after mixing. Black particles were observed at the bottom of the vial, at this stage the solution was clear and colorless.

Comparing the results shown in Figure 70 on page 128 to Figure 75 on the preceding page it seems like the optical properties of the smallest GNPs (5 nm) is less affected by the acidic environment than those of the 10 nm and the 40 nm GNPs. The 10 nm GNPs in  $\text{HNO}_3$  0.01 M exhibits significantly increased absorbance ( $\sim 40\%$ ) 1 h after the acid was added, this might suggest that the particles have conglomerated into larger particles.

For the 40 nm GNPs the absorbance decreased significantly after the addition of acid. This might indicate that some of the 40 nm GNPs might have conglomerated into particles large enough to form sediment and end up at the bottom of the vial. The explanation of less absorbance would in this case be due to less particles participating in the spectroscopic measurement.

As it was mentioned in Section 6, describing the LPSRs, the shape of the nanoparticles have a significant effect on the optical properties on metal nanoparticles. The surface plasmon absorption maximum ( $\lambda_{max}$ ) depends on the aspect ratio<sup>1</sup>  $r$  of the particle as [48]:

$$\lambda_{max} = 420 + r \cdot 95 \text{ [nm]} \quad (31)$$

Again, looking at the presented graphs, this suggests that the GNPs have changed their shape and that this change is most pronounced for the 10 nm GNPs. If equation (31) is used, the 5 nm GNPs would have an aspect ratio of 1.4, the 10 nm GNPs 1.5 and the 40 nm GNPs 1.4 if the values from samples containing HNO<sub>3</sub> 0.11 M, measured 1 h after mixing is considered.

It should also be noted that the 10 nm GNPs had a very large red shift for the HNO<sub>3</sub> 0.11 M sample 10 min after mixing, the aspect ratio for this specific sample was 1.98 after 1 hour the aspect ratio had decreased to 1.5. By visual inspection small particles was observed at the bottom of some of the samples, this suggest that some of the particles might not have participated in the absorption measurements performed after the mixing.

To Summarize: the added nitric acid affect the optical properties of the GNP colloids, both size and shape may have been altered after the acid was mixed into the colloid. Both acid concentration and elapsed time since the mixing are affecting the optical properties.

---

<sup>1</sup> aspect ratio = length of particle divided by width of particle

## D.2 Comparing cell performance

The I-V characterization were carried out with the same equipment and same procedures as for the other cells in the work, for these cells however, only unfiltered light (T100) was used in the measurements. This was a comparative experiment, carried out to see the effects of varying the amount of nitric acid in the TiO<sub>2</sub> slurry on the cell performance, therefore the measured current of cells with the same GNP size but different amounts of nitric acid are shown in the same figure. Six different cells were made with different combinations of GNP size and amount of nitric acid as declared in Table 28. In this table, 100 % of nitric acid refers to the amount used in the standard composition of TiO<sub>2</sub> slurry as declared in Table 9 on page 65. The resulting I-V graphs are shown in Figures 77 and 78 on the next page.

**Table 28:** The combinations of nitric acid and GNP size for the solar cells used in the study of the effects of nitric acid on the cell performance. The amount of HNO<sub>3</sub> is given as percent of the amount in the standard composition, see Table 9 on page 65. The cells are numbered ac1 - ac6 for reference.

Cell nr.	ac1	ac2	ac3	ac4	ac5	ac6
GNP size (nm)	5	5	5	10	10	10
Amount of HNO <sub>3</sub> 1M (%)	0	30	100	0	30	100

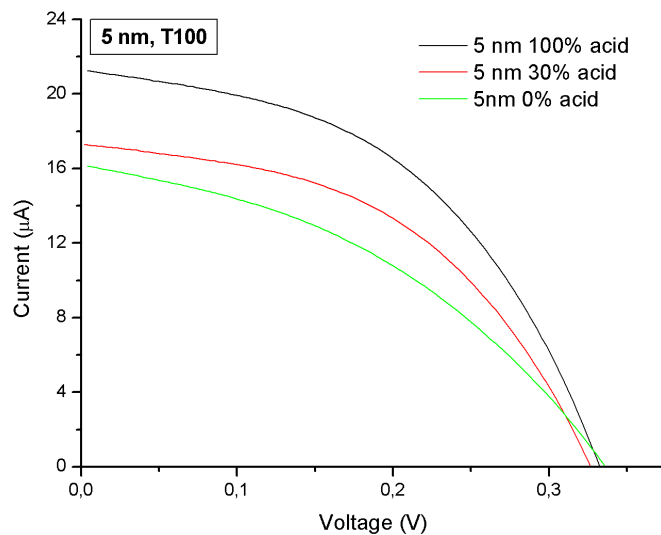


**Figure 77:** IV-graphs for cells ac1, ac2 and ac3, containing 5 nm GNPs and different amounts of HNO<sub>3</sub> in the TiO<sub>2</sub> slurry.

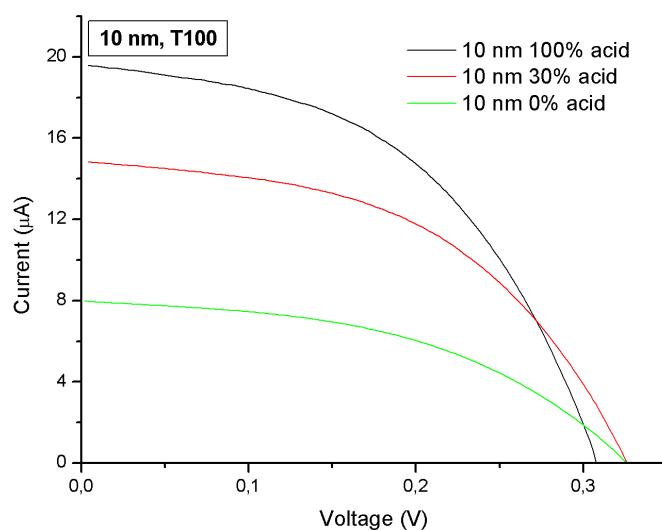


**Figure 78:** IV-graphs for cells ac4, ac5 and ac6, containing 10 nm GNPs and different amounts of  $\text{HNO}_3$  in the  $\text{TiO}_2$  slurry.

From figures 77 and 78 it is clear that the highest photocurrent is achieved for cells containing 100% of the amount from the standard composition. The open circuit voltage is not significantly affected by the variation in amount of  $\text{HNO}_3$  but the short circuit current was decreased with 20 resp. 25% for cells with 5nm particles and with 24 resp 60% for the cells with 10 nm particles when the amount of nitric acid was lowered from 100 to 30 and 0% respectively.

To summarize the observations from this study of effects of nitric acid on GNP optical properties. By visual inspection, the  $\text{TiO}_2$  solutions of GNPs, triton, carbowax, deionized water and nitric acid of different concentrations were observed to change in color compared to solutions without nitric acid. By photo spectroscopy, it was clearly shown that the optical properties of the gold colloids were affected by adding nitric acid to the solutions. As that the optical properties were changed, it is reasonable to conclude that the size and shape of the GNPs in the final solutions may have been changed.

The full scale experiment of building cells and subsequently characterize them, showed that reducing the amount of nitric acid in the  $\text{TiO}_2$  slurry lowered the photocurrent and thereby also the efficiency of the cells. Even though the GNPs may be affected by the nitric acid, the best cell performance was achieved by keeping the standard composition of the slurry as shown in Table 9 on page 65.

This separate study points out the fact that it might be ambiguous what size and shape the GNPs actually have in the assembled cells. This should be kept in mind in discussions and conclusions based on results from experiments where GNP size and shape are referred to as parameters.

## References

- [1] US Department of commerce. U.s. and world population clock, 2015. Accessed at <http://www.census.gov/popclock/> on Feb 26, 2015 (2015).
- [2] Index Mundi. Country comparison, population growth rate, 2014. Accessed at <http://www.indexmundi.com/g/r.aspx?v=241> on Feb 26, 2015 (2014).
- [3] U.S. Energy Information Administration (EIA). International energy outlook 2013 (ieo2013), June 2013. Accessed at <http://www.eia.gov/forecasts/ieo/pdf/0484on> Oct 6, 2014 (2013).
- [4] Energimyndigheten. Snabbare ökning av fornybar energi, June 2011. Accessed at <http://www.energimyndigheten.se/Press/Nyheter/Nyhetsarkiv-2011/Snabbare-okning-av-fornybar-energi> on Oct 2, 2014 (2011).
- [5] Energiuskottet at the Royal Swedish Academy of Science. Sveriges energisituation i ett europeiskt och globalt perspektiv. Accessed at [http://www.kva.se/globalassets/vetenskap\\_samhallet/energi/utskottet/2014/rapport\\_sverigesenergisituation\\_140108.pdf](http://www.kva.se/globalassets/vetenskap_samhallet/energi/utskottet/2014/rapport_sverigesenergisituation_140108.pdf) on Nov 20, 2014 (2013).
- [6] A. Luque and Steven Hegedus. *Handbook of photovoltaic science and engineering*. Wiley, Chichester, 2003.
- [7] Egbert Boeker and Rienk v. Grondelle. *Environmental physics*. Wiley, Chichester, 1999.
- [8] nrel. Best research cell efficiencies, 2015. Accessed at <http://energyinformative.org/nrel-efficiency-record-two-junction-solar-cell> on Oct 16, 2014 (2014).
- [9] Martin A. Green, Keith Emery, Yoshihiro Hishikawa, Wilhelm Warta, and Ewan D. Dunlop. Solar cell efficiency tables (version 45). *Progress in Photovoltaics: Research and Applications*, 23(1):1–9, 2015.
- [10] Michael Grätzel. Dye-sensitized solar cells. *Journal of Photochemistry and Photobiology, C: Photochemistry Reviews*, 4(2):145–153, 2003.
- [11] Md K. Nazeeruddin, Etienne Baranoff, and Michael Grätzel. Dye-sensitized solar cells: A brief overview. *Solar Energy*, 85(6):1172–1178, 2011.
- [12] Siu-Pang Ng, XiaoQing Lu, Ning Ding, Chi-Man Lawrence Wu, and Chun-Sing Lee. Plasmonic enhanced dye-sensitized solar cells with self-assembly gold tio<sub>2</sub>-core shell nanoislands. *Solar Energy*, 99(0):115 – 125, 2014.
- [13] Tokuhisa Kawawaki, Yukina Takahashi, and Tetsu Tatsuma. Enhancement of dye-sensitized photocurrents by gold nanoparticles: Effects of plasmon coupling. *The Journal of Physical Chemistry C*, 117(11):5901–5907, 2013.
- [14] Yan Li, Hong Wang, Quanyou Feng, Gang Zhou, and Zhong-Sheng Wang. Gold nanoparticles inlaid tio<sub>2</sub> photoanodes: a superior candidate for high-efficiency dye-sensitized solar cells. *Energy & Environmental Science*, 6(7):2156–2165, 2013.
- [15] Changwoo Nahm, Hongsik Choi, Jongmin Kim, Dae Ryong Jung, Chohui Kim, Joonhee Moon, Byungjoo Lee, and Byungwoo Park. The effects of 100 nm diameter au nanoparticles on dye sensitized solar cells. *Applied Physics Letters*, 99(25), 2011.
- [16] Bobby Sebo, Niu Huang, Yumin Liu, Qidong Tai, Liangliang Liang, Hao Hu, Sheng Xu, and Xing-Zhong Zhao. Dye-sensitized solar cells enhanced by optical absorption, mediated by tio<sub>2</sub> nanofibers and plasmonics ag nanoparticles. *Electrochimica Acta*, 112(0):458 – 464, 2013.
- [17] K. R. Catchpole and A. Polman. Design principles for particle plasmon enhanced solar cells. *Applied Physics Letters*, 93(19):–, 2008.
- [18] K. R. Catchpole and A. Polman. Plasmonic solar cells. *Opt. Express*, 16(26):21793–21800, Dec 2008.
- [19] Stafford W Sheehan, Heeso Noh, Gary W Brudvig, Hui Cao, and Charles A Schmuttenmaer. Plasmonic enhancement of dye-sensitized solar cells using core-shell-shell nanostructures. *The Journal of Physical Chemistry C*, 117(2):927–934, 2013.
- [20] Harry A Atwater and Albert Polman. Plasmonics for improved photovoltaic devices. *Nature materials*, 9(3):205–213, 2010.
- [21] S. Pillai and M.A. Green. Plasmonics for photovoltaic applications. *Solar Energy Materials and Solar Cells*, 94(9):1481 – 1486, 2010. PVSEC 18.

- [22] Anders Hagfeldt, Gerrit Boschloo, Licheng Sun, Lars Kloo, Henrik Pettersson, Organisk kemi, KTH, Skolan for kemivetenskap (CHE), Fysikalisk kemi (stangd 20110630), Kemi, and Oorganisk kemi (stangd 20110630). Dye-sensitized solar cells. *Chemical reviews*, 110(11):6595, 2010.
- [23] H. Kitching, A. J. Kenyon, and I. P. Parkin. The interaction of gold and silver nanoparticles with a range of anionic and cationic dyes. *Physical chemistry chemical physics : PCCP*, 16(13):6050–6059, 2014.
- [24] Matteo Biancardo, Keld West, and Frederik C. Krebs. Quasi-solid-state dye-sensitized solar cells: Pt and pedot:pss counter electrodes applied to gel electrolyte assemblies. *Journal of Photochemistry & Photobiology, A: Chemistry*, 187(2):395–401, 2007.
- [25] Matteo Biancardo, Keld West, and Frederik C. Krebs. Optimizations of large area quasi-solid-state dye-sensitized solar cells. *Solar Energy Materials and Solar Cells*, 90(16):2575–2588, 2006.
- [26] Mudiyansele Wijendra Jayalath Bandara, Pierisge Sadeesha Leonard Fernando, Hewage Dhanushka, Naleen Sampath Fernando, Malavi Achchi Kankanamge Lakshman Dissanayake, Lekam Ralalage Anura, Kalinga Bandara, and Bengt-Erik Mellander. Conductivity and thermal properties of pan based polymer electrolytes for possible application in photo electrochemical solar cells. *Journal of Electrical Engineering*, 1:34–39, 2013.
- [27] M.A.K.L. Dissanayake, C.A. Thotawatthage, G.K.R. Senadeera, T.M.W.J. Bandara, W.J.M.J.S.R. Jayasundera, and B.-E. Mellander. Efficiency enhancement by mixed cation effect in dye sensitized solar cells with PAN based gel polymer electrolyte. *Journal of Photochemistry and Photobiology A: Chemistry*, 246(0):29 – 35, 2012.
- [28] TMWJ Bandara, T Svensson, MAKL Dissanayake, Maurizio Furlani, WJMJSR Jayasundara, PSL Fernando, Ingvar Albinsson, and Bengt-Erik Mellander. Conductivity behaviour in novel quasi-solid-state electrolyte based on polyacrylonitrile and tetrahexylammonium iodide intended for dye sensitized solar cells. *Journal of the National Science Foundation of Sri Lanka*, 41(3):175–184, 2013.
- [29] T. M. W. J. Bandara, T. Svensson, M. A. K. L. Dissanayake, M. Furlani, W. J. M. J. S. R. Jayasundara, and Bengt-Erik Mellander. Tetrahexylammonium iodide containing solid and gel polymer electrolytes for dye sensitized solar cells. 2012.
- [30] National Renewable Energy Laboratory. Reference solar spectra irradiance. Accessed at <http://redc.nrel.gov/solar/spectra/am1.5/> on Dec 29, 2014.
- [31] T. Markvart and L. Castaner. *Solar Cells: Materials, Manufacture and Operation*. Elsevier Science, 2004.
- [32] Anders. Hagfeldt and Michael. Grätzel. Light-induced redox reactions in nanocrystalline systems. *Chemical Reviews*, 95(1):49–68, 1995.
- [33] K. Kalyanasundaram and M. Grätzel. Applications of functionalized transition metal complexes in photonic and optoelectronic devices. *Coordination Chemistry Reviews*, 177(1):347 – 414, 1998.
- [34] Solar cell central. Solar efficiencies, 2011. Accessed at <http://solarcellcentral.com/limits-page.html> on nov 16, 2014 (2011).
- [35] William Shockley and Hans J. Queisser. Detailed balance limit of efficiency of p-n junction solar cells. *Journal of Applied Physics*, 18(3):510–519, 1961.
- [36] Frank Dimroth. New world record for solar cell efficiency at 46 Accessed at <http://www.ise.fraunhofer.de/en/press-and-media/press-releases/press-releases-2014/> on Dec 20, 2014 (2014).
- [37] Jenny Nelson. *The physics of solar cells*. Imperial College Press, London, 2003.
- [38] Howard R. Stuart and Dennis G. Hall. Island size effects in nanoparticle-enhanced photodetectors. *Applied Physics Letters*, 75(26):3815–3817, 1998.
- [39] Keisuke Nakayama, Katsuaki Tanabe, and Harry A. Atwater. Plasmonic nanoparticle enhanced light absorption in gas solar cells. *Applied Physics Letters*, 75(12):121904–121904–3, 2008.
- [40] Anders Hagfeldt, Ute B. Cappel, Gerrit Boschloo, Licheng Sun, Lars Kloo, Henrik Pettersson, and Elizabeth A. Gibson. *Chapter IE-1 - Dye-Sensitized Photoelectrochemical Cells*, pages 479–542. Academic Press, Boston, 2012.
- [41] Meena Dhankhar, Om Pal Singh, and V. N. Singh. Physical principles of losses in thin film solar cells and efficiency enhancement methods. *Renewable and Sustainable Energy Reviews*, 40:214–223, 2014.
- [42] Tom Markvart Luis Castaner. *Solar Cells, Materials, Manufacture and Operation*. Elsevier Science, Oxford, 2005.

- [43] D.S. Ginley and D. Cahen. *Fundamentals of Materials for Energy and Environmental Sustainability*. Cambridge University Press, 2011.
- [44] Ken-ichi Ishibashi, Yasuo Kimura, and Michio Niwano. An extensively valid and stable method for derivation of all parameters of a solar cell from a single current-voltage characteristic. *Journal of Applied Physics*, 104(9):094507–094507–6, 2008.
- [45] Renu Guliani. Exact analytical analysis of dye-sensitized solar cell: Improved method and comparative study. *The Open Renewable Energy Journal*, 5(1):49–60, 2012.
- [46] L. Bay and K. West. An equivalent circuit approach to the modelling of the dynamics of dye sensitized solar cells. *Solar Energy Materials and Solar Cells*, 87(1):613–628, 2005.
- [47] Juan Bisquert, Jorge Garcia-Canadas, Ivan Mora-Sero, and Emilio Palomares. Comparative analysis of photovoltaic principles governing dye-sensitized solar cells and p-n junctions. volume SPIE-5215, pages 49–59, 2003.
- [48] Valerio Voliani and ebrary (e-book collection). *Update on gold nanoparticles*. Smithers Rapra Publishing, Shrewsbury, 2013.
- [49] Stefan A. Maier, SpringerLink (e-book collection), and SpringerLink (Online service). *Plasmonics: fundamentals and applications*. Springer, New York, 2007.
- [50] Michael I. Mishchenko, Larry D. Travis, and Andrew A. Lacis. *Scattering, absorption, and emission of light by small particles*. Cambridge University Press, Cambridge, 2002.
- [51] Michael P Marder. *Condensed matter physics*. Wiley, Oxford, 2010.
- [52] Craig F. Bohren and Donald R. Huffman. *Absorption and scattering of light by small particles*. Wiley, New York, 1998.
- [53] Joachim Sukmanowski, Reinhard Carius, Thomas Müller, Bart Pieters, Joachim Kirchhoff, Peiqing Luo, Francois-Xavier Royer, Wilfried Reetz, Etienne Moulin, and Helmut Stiebig. Photoresponse enhancement in the near infrared wavelength range of ultrathin amorphous silicon photosensitive devices by integration of silver nanoparticles. *Applied Physics Letters*, 95(3):033505–033505–3, 2009.
- [54] P. Apell and Carl Hägglund. Plasmonic near-field absorbers for ultrathin solar cells. *Journal of Physical Chemistry Letters*, 3(10):1275, 2012.
- [55] Yongqian Xu, Matthew J. Panzner, Xiaopeng Li, Wiley J. Youngs, and Yi Pang. Host-guest assembly of squaraine dye in cucurbit[8]uril: its implication in fluorescent probe for mercury ions. *Chemical communications (Cambridge, England)*, 46(23):4073, 2010.
- [56] Carl Hägglund, Michael Zäch, and Bengt Kasemo. Enhanced charge carrier generation in dye sensitized solar cells by nanoparticle plasmons. *Applied Physics Letters*, 75(1):013113–013113–3, 2008.
- [57] JiuJun Zhang. *Electrochemical Impedance Spectroscopy in PEM Fuel Cells*. Springer London, Dordrecht, 2009.